DOTTORATO DI RICERCA IN SCIENZE DELLA TERRA

Università degli Studi di Firenze

PING LU

Remote Sensing: applications for landslide hazard assessment and risk management

settore scientifico disciplinare: GEO-05

Tutore: Prof. Nicola Casagli

Co-Tutore: Dr. Filippo Catani

Dr. Veronica Tofani

Coordinatore: Prof. Federico Sani

XXIII CICLO

Firenze, 31 Dicembre 2010

I would like to dedicate this thesis to my loving wife and parents ...

Acknowledgements

I would like to thank Prof. Nicola Casagli, my supervisor in University of Firenze, for his constructive suggestions and constant support during this research, inspiring me the proper way of thinking research questions and corresponding solutions. I am also thankful to Dr. Filippo Catani and Dr. Veronica Tofani, the co-supervisors in University of Firenze, for their patient guidance throughout different stages of this study.

I am grateful to the European Commission FP6 project of Mountain Risks and its partners for the training and the transfer of knowledge. In particular, Dr. Jean-Philippe Malet and Prof. Olivier Maquaire, the directors of the project, show their full passions in managing this wonderful project.

Dr. Norman Kerle in University of Twente shared his knowledge of remote sensing with me and provided many useful references as well as friendly encouragement. Andre Stumpf in University of Twente expressed his interest in my work and provided many suggestions for the improvement of this work.

I had the pleasure of meeting the nice colleagues in University of Firenze. They are wonderful people and their contribution makes

this research work possible. I really established the deep friendship with my lovely colleagues.

Finally, I owe a special debt of thanks to my wife and parents for their consistent support, advice and respect to letting me make my own decisions, in many detailed aspects.

Abstract

Landslide, as a major type of geological hazard, represents one of the natural hazards most frequently occurred worldwide. Landsliding phenomena not only poses great threats to human lives, but also produces huge direct and indirect socio-economic losses to societies in all mountainous areas around the world. The global concern of landslide hazard and risk have raised the need for effective landslide hazard analysis and quantitative risk assessment.

Remote sensing offers a valuable tool for landslide studies at different stages, such as detection, mapping, monitoring, hazard zonation and prediction. In past years, remote sensing techniques have been substantially developed for landslide researches, mainly focusing on the applications of aerial-photos, optical sensors, SAR interferometry (InSAR) and laser scanning. In this study, two newly-developed remote sensing techniques are to be introduced, particularly aiming at rapid detection and mapping of landslide hazards with semi-automatic approaches.

The first approach employs the technique of Object-Oriented Analysis (OOA). It represents a semi-automatic approach based on systemized analysis using very high resolution (VHR) optical images. The purpose is to efficiently map rapid-moving landslides and debris flows

with minimum manual participation. The usefulness of this methodology is demonstrated on the Messina landslide event in southern Italy that occurred on 1 October 2009. The algorithm is first developed in a training area of Altolia, and subsequently tested without modifications in an independent area of Itala. The principal novelty of this work is (1) a fully automatic problem-specified multi-scale optimization for image segmentation, and (2) a multi-temporal analysis at object level with several systemized spectral and textural measurements.

The second approach is on the basis of recently developed long-term InSAR technique of Persistent Scatterer Interferometry (PSI), which generates stable radar benchmarks using a multi-interferogram analysis of SAR images and enables a detection of mass movement with millimeter precision. A statistical analysis of PSI Hotspot and Cluster Analysis (PSI-HCA) is further developed based on the Getis-Ord G_i^* statistic and kernel density estimation. It has been performed on PSI point targets in hilly and mountainous areas within the Arno river basin in central Italy. The purpose is to use PS processed from 4 years (2003-2006) of RADARSAT images for identifying areas preferentially affected by extremely slow-moving landslides. This spatial statistic approach of PSI-HCA is considered as an effective way to extract useful information from PS at the regional scale, thus providing an innovative approach for a rapid detection of extremely slow-moving landslides over large areas.

Although both two methods are initially developed for the same purpose of a rapid identification of landslide hazard, it is not easily to compare the results of these two approaches. A possible solution is to compare their outcomes at the risk level. For this reason, the output of PSI-HCA is further included in a quantitative landslide hazard and risk assessment, which also provides a fundamental basis for potential risk management in the future. The risk assessment is carried out in the Arno river basin, with the exposure of estimated losses in euro. The result indicates that approximately 3.22 billion euro losses are predicted for the upcoming 30 years within the whole basin.

In sum, the present study shows a great potential for newly-developed remote sensing techniques in improving procedures not only for identifying and locating landslide hazards, but also for a subsequent quantitative landslide hazard and risk assessment.

Contents

List of Figures

List of Tables

Chapter 1

Introduction

1.1 Landslide hazard: an overview

1.1.1 Landslide: definition and typology

Landslide, as a major type of geological hazard, represents one of the natural hazards most frequently occurred worldwide. The term 'landslide', as simply denoted by Cruden [1991], refers to 'the movement of a mass of rock, debris or earth down a slope'.

A complete classification of landslide is not easy to be determined. Some well-accepted classification algorithms can be found in recent published literatures. For example, a well-known classification of landslides was proposed by Varnes [1978] and subsequently improved by Cruden and Varnes [1996], primarily focusing on the combination of movement and material types. Besides, another widely recognized classification was proposed by Hutchinson [1988], referring to morphological and geotechnical parameters of landslides in relation to geology and

hydrogeology. Moreover, Leroueil et al. [1996] have suggested a characterization of slope movements with further involvement of those geotechnical parameters, including controlling parameters, predisposition factors, triggering/aggravating factors, revealing factors and corresponding consequences. Additionally, Hungr et al. [2001] have modified the landslide classification based on a new separation of landslide materials, with a more detailed consideration of material type, water content, pore pressure, recurrent path and velocity.

1.1.2 Landslide hazard in Italy

Despite the diversity of landslide definition and classification, it is widely agreed that landsliding phenomena not only poses great threats to human lives, but also produces huge direct and indirect socio-economic losses to societies in all mountainous areas around the world. In particular, with a large coverage (ca. 75%) of hilly and mountainous areas, Italy is among those countries most susceptible to landslide hazard.

According to the estimations from the Italian National Research Council [Guzzetti, 2000], Italy has suffered the highest fatalities of landslides in Europe and in the last century at least 5939 people (in average 59.4 deaths/year) have been reported dead or missing by reason of landslide occurrences, including a catastrophic event of Vajont occurred on 9 October 1963, bringing a victim number of 1917 people. Moreover, each year in Italy ca. 1-2 billion euro direct economic losses were estimated from the damages of landslides, accounting for an average of 0.15% the gross domestic product (GDP) of Italy [Canuti et al., 2004]. With a further consideration of those indirect losses, this number could even rise

to ca. 0.3-0.4% of the total GDP of Italy [Canuti et al., 2004; Schuster, 1996].

1.1.3 Global concern of landslide hazard

With the development of landslide studies, the recent focus of landslide disasters has been extended to a global concern.

According to the report from International Disaster Database [OFDA/CRED, 2006], landslide is among the natural hazards most frequently occurred in the whole world, with a potentially 4 million people affected worldwide in 2006. The advent of this report was also accompanied with some landslide studies at the global scale. For example, based on the global database, a worldwide analysis of landslide hazard and risk, namely the 'global landslide hotspots' (figure 1.1), has been proposed and accomplished by Nadim et al. [2006]. Similarly, Hong et al. [2006, 2007] have presented the efforts for a mapping of global landslide inventory and a further assessment of global landslide hazard and risk (see risk map in figure 1.2).

Additionally, under the background of worldwide global warming and climate changing as reported by IPCC [2007], recent studies have also claimed landslide occurrences as geomorphological indicators of global climate changes. For instance, Soldati et al. [2004] have dated several landslides in the Italian Dolomites and correlated the recorded increase of landslide activities with climate changes since the Late Glacial. The study was further extended by Borgatti and Soldati [2010] and it was concluded that the alteration in landslide frequency can be interpolated as changes in the hydrological conditions of slopes, which is closely connected with climate influences. Moreover, Jakob and Lambert [2009] have re-

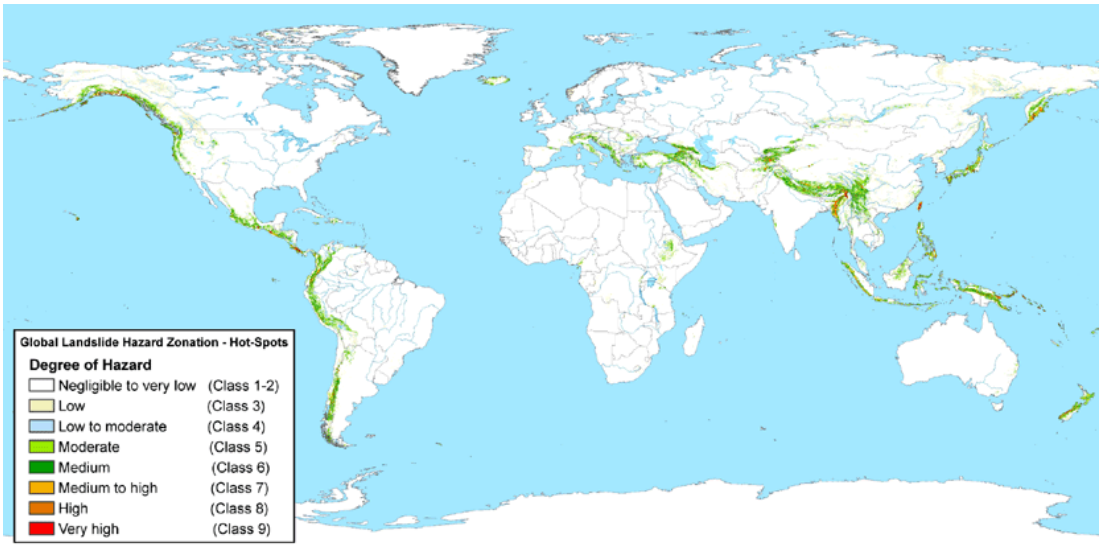

Figure 1.1: Global hotspot landslide hazard zonation for the world [Nadim et al., 2006]

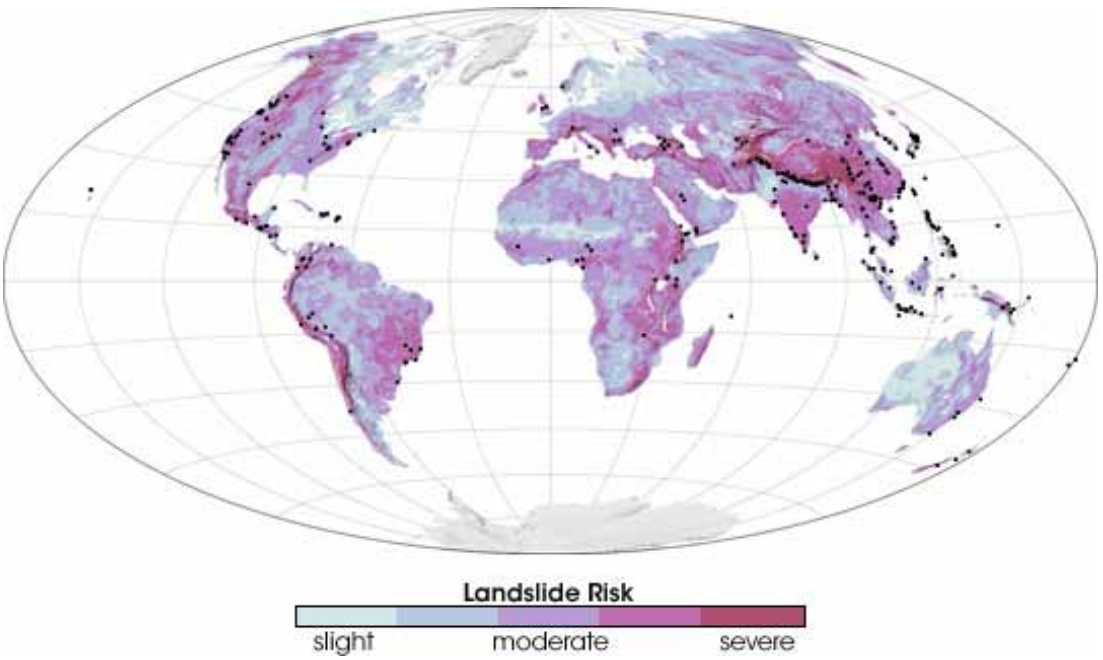

Figure 1.2: Global landslide risk map prepared by NASA [Hong et al., 2006, 2007; NASA, 2007]

ported that the influence of climate change is potentially reflected in an increase of landslide frequency, based on the simulation of climate models for precipitation regimes. These studies have fundamentally revealed an existence of potential landslide responses to climate changes.

Furthermore, according to Nadim et al. [2006], the other reasons bringing an increase of globally-reported landslide occurrences could be summarized as a consequence of uncontrolled human activities such as overexploited natural resources, intensive deforestation, plus poor land-use planning and undisciplined growing urbanization. This is in accordance to the report of Unite Nations [UN/ISDR, 2004], which emphasizes the important role of decent land-use planning and management in conducting natural hazard assessment and risk mapping.

1.2 Study scope and thesis outline

The global concern of landslide hazard and risk have raised the need of effective landslide hazard analysis and quantitative risk assessment. Also, in past decades, the urgent need to facilitate the understanding of landslides and the ability to handle related risks, has created important research and development activities for landslide studies [Nadim, 2002], which include the significant development of remote sensing techniques for landslide studies, as chiefly to be dealt with in the following content of this thesis.

1.2.1 Objectives of the research

The aim of this study is to integrate recent-developed remote sensing techniques in landslide studies with particular focuses on:

- An efficient mapping of rapid landslides and debris flows for creating an event-related landslide inventory based on (semi)-automatic remote sensing approach.
- A rapid detection of slow-moving landslides using (semi)-automatic remote sensing approaches at the regional scale.
- The use of remote sensing outputs for a quantitative landslide susceptibility, hazard and risk assessment.

1.2.2 Research questions

The following proposed research questions would assist to address the above-mentioned objectives:

- Which type of remote sensing data and technique is useful for a rapid mapping of landslide inventory?
- Which kind of remote sensing products can be used for a detection of (extremely) slow-moving landslides?
- Which information can be extracted from these remote sensing data and technique for an effective landslide detection and mapping?
- What are the useful and efficient approaches to extract these information?
- How can these approaches be improved in order to facilitate an potential automated approach for the purpose of rapid mapping and detection of landslides?

- How to evaluate the results of these approaches and how much accuracies can these approaches obtain?
- How can these remote sensing data and techniques further help to an assessment of the landslide susceptibility and hazard zoning, and a subsequent quantitative risk analysis?
- What are the novelties of this study compared to previous works of remote sensing for landslide studies?
- How can the whole study be improved for the future works?

1.2.3 Thesis structure and outline

This thesis is outlined as figure 1.1, including a total of seven chapters. The rest of the chapters are structured as follows:

- Chapter 2 renders a review of previously published principal remote sensing techniques for different stages of landslide studies. The review is organized by different remote sensing approaches, including the visual interpretation of aerial-photos, remote sensing within optical electromagnetic spectrum, satellite and ground-based SAR interferometry (InSAR), as well as airborne and terrestrial laser scanning.
- Chapter 3 firstly introduces the concept of a recent-developed technique: object-oriented analysis (OOA). The chapter further deals with the application of OOA in semi-automatic inventory mapping of rapid-moving landslides and debris flows, choosing a catastrophic event of Messina in Sicily, southern Italy as the case study.

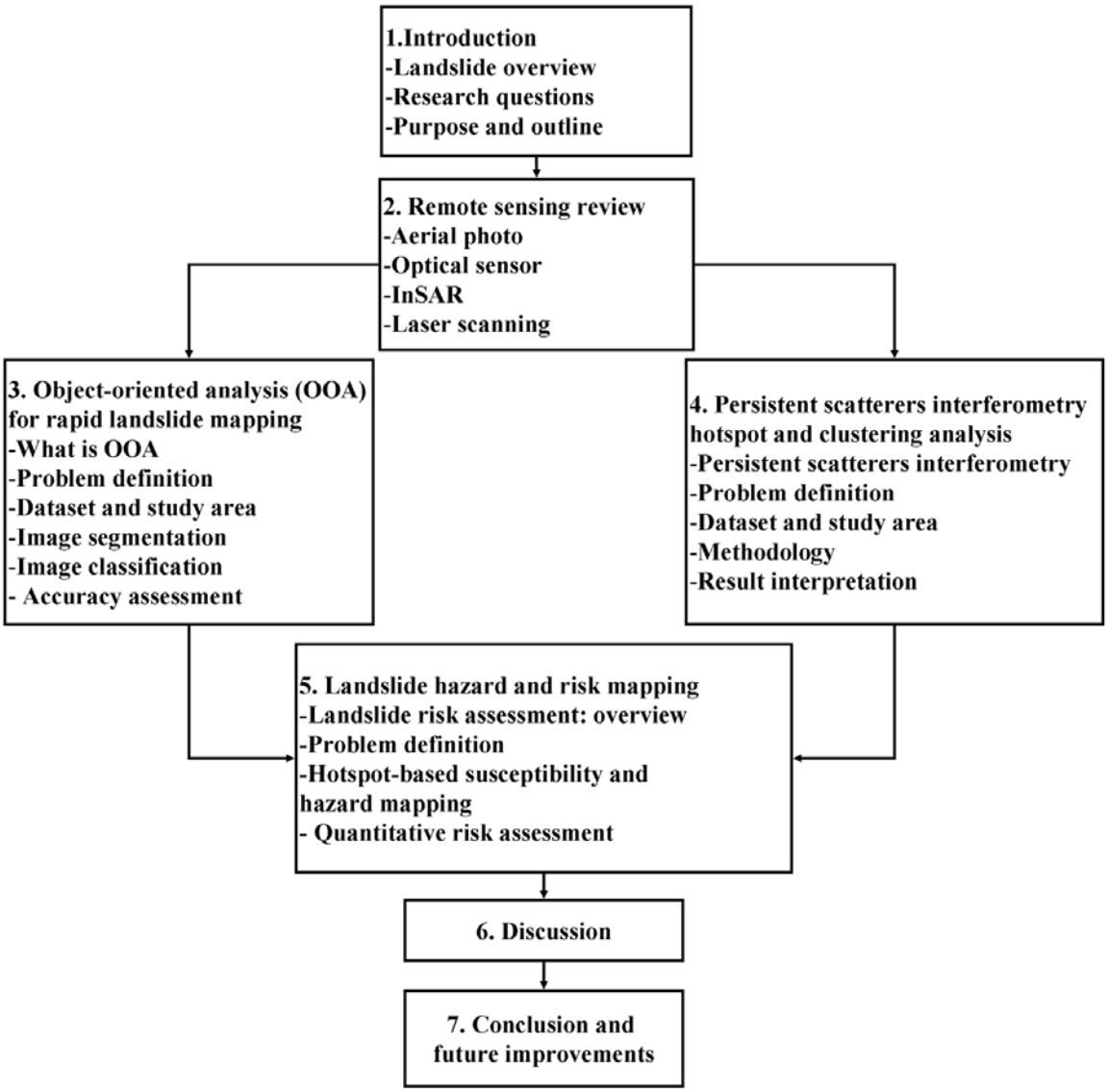

Figure 1.3: The structure and content of the thesis.

- Chapter 4 initially renders the novelty of a newly-developed InSAR technique: persistent scatterers interferometry (PSI). The chapter further introduces a new approach of PSI Hotspot and Cluster Analysis (PSI-HCA) for a rapid detection of slow-moving landslides. The usefulness of this approach is presented in the case study of the Arno river basin in central Italy.

- Chapter 5 first presents an short review regarding landslide hazard and risk assessment. The chapter then introduces an effort utilizing the previous derived outputs of PSI-HCA for further susceptibility and hazard zoning of landslides and a quantitative landslide risk assessment in the Arno river basin.

- Chapter 6 mainly deals with some discussions regarding those detailed problems and uncertainties existed in different stages of this study.

- Chapter 7 is the conclusion of the whole research work. Also some recommendations for further improvements are provided for possible future research activities.

Chapter 2

Remote sensing for landslide studies: a review

Remote sensing, which is simply defined as the approach of obtaining information without physical contact [Lillesand and Kiefer, 1987], is capable to survey distant areas where field works are difficult to be carried out. Remote sensing contributes a valuable tool for landslide studies at different stages, such as detection and mapping, monitoring, hazard zonation and prediction [Canuti et al., 2004; Mantovani et al., 1996; Metternicht et al., 2005]. In this chapter, the previous published contributions of remote sensing to those landslide studies are to be reviewed, arranged by the following useful remote sensing techniques: the visual interpretation of aerial-photos, remote sensing within optical electromagnetic spectrum, satellite/ground-based SAR interferometry (InSAR), and airborne/terrestrial laser scanning.

2.1 Visual interpretation of aerial-photos

A traditional but still useful remote sensing technique for landslide studies is the visual interpretation of aerial-photos which are usually provided with excellent spatial resolution. Visual interpretation of aerial-photos is particularly useful for the mapping and monitoring of landslide characteristics (distribution, classification) and related factors (land cover, lithology, slope, etc.), and until now it is still one of the most important sources for landslide inventory creations and modifications [Blesius and Weirich, 2010; Donati and Turrini, 2002; Metternicht et al., 2005].

The particular useful approach through aerial-photos is the 3D interpretation from stereo pairs [Mantovani et al., 1996; Soeters and Westen, 1996]. This stereoscopic approach, combined with additional field surveys, is especially useful for mapping and monitoring some landslides under forests and thus possibly not visible from single aerial-photo [Brardinoni et al., 2003]. Besides, the 3D interpretation from stereo pairs of aerial-photos enables a detailed recognition of landslide features and diagnostic morphology [Metternicht et al., 2005]. Also, the contribution of stereo pairs includes the digital elevation model (DEM), generated from photogrammetric technique, useful for the estimation of surface elevation, surface displacements and volume-related features [Blesius and Weirich, 2010; Coe et al., 1997; kaab, 2002].

Furthermore, as one of the most important uses, archived aerial-photos combined with a collection of landslide records from historical recourses, such as newspaper, enables a trace of landslide occurrences in older periods [Mantovani et al., 1996; Parise, 2001]. In particular, van Westen and Getahun [2003] have

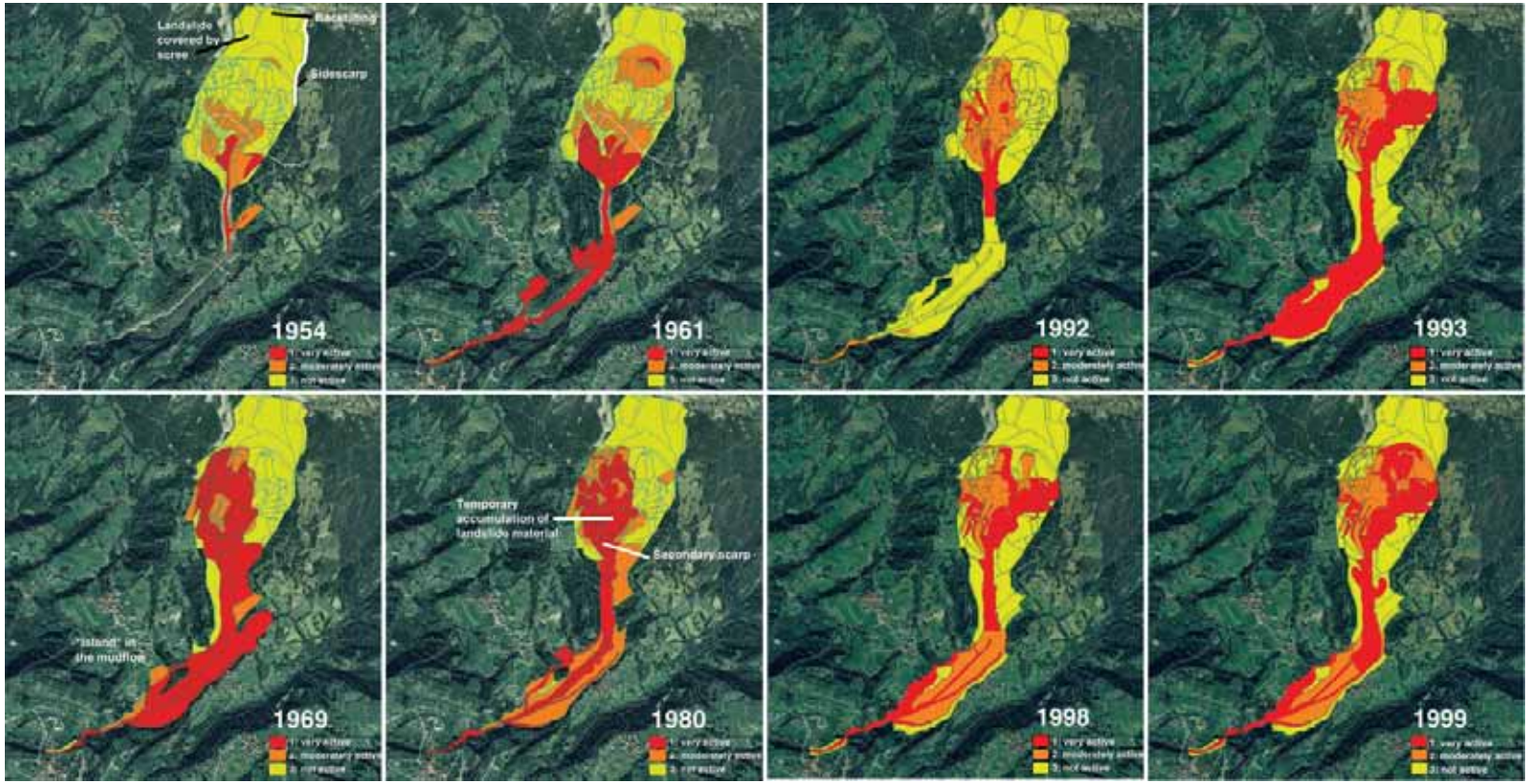

Figure 2.1: The example of analyzing the landslide evolution using temporal aerial-photos in Tessina [van Westen and Getahun, 2003]

demonstrated a typical qualitative analysis of the evolution of Tessina landslide in North-eastern Italy for more than 40 years, based on landslide maps interpreted from sequential multi-temporal aerial-photos (figure 2.1). This simple but effective method successfully observed the expanding reactivation activities of an old existing landslide.

However, the spectral information which can be extracted from the aerial photos is very limited, especially compared to those satellite imagery captured from multi-spectral sensors, which is to be described in the next section.

2.2 Optical satellite sensors

The satellite remote sensing within optical electromagnetic spectrum became popular with the launch of Landsat series of satellites, which also brought the application of optical satellite sensors in landslide studies. However, few studies have revealed the usefulness of Landsat MSS, TM and ETM+ data in landslide mapping and monitoring. The major difficulty is due to the low spatial resolution of this kind of conventional sensors (e.g. with the best resolution 30m for visible and near-infrared, Landsat-7), thus limiting their uses especially in a detailed landslide mapping [Gupta and Joshi, 1990; Sauchyn and Trench, 1978], especially in the early times their resolution is far lower compared to aerial-photos. This was also justified by Huang and Chen [1991] who reported a maximum accuracy of 16.6% for landslide mapping at Healy, Alaska using Landsat TM data. This limitation was also agreed by Mantovani et al. [1996], who have additionally mentioned that optical satellite remote sensing with low spatial resolution is not satisfactory for characterizing those particular landslide features.

With the improvement of spatial resolution for recently-developed optical sensors, some studies have shown the potential improvements of mid-resolution sensors in landslide studies, such as those imageries from SPOT [Lin et al., 2004; Nichol and Wong, 2005; Yamaguchi et al., 2003] and ASTER [Fourniadis et al., 2007; Liu et al., 2004], especially for landslide detection and mapping as well as hazard assessment purposes. In particular, Yamaguchi et al. [2003] enabled a detection of 20 to 30m displacement with reference to 20m spatial resolution of SPOT HRV data, with the inclusion of a sub-pixel image matching techniques. Also, another advantage brought by ASTER data is an inclusion of a nadir and backward pair of band 3 which enables a generation of DEM from photogrammetric techniques.

Recent launches and increasing availability of very high resolution (VHR) imageries enables a even more detailed characterization and differentiation of landslide processes for hazard analysis. For example, SPOT-5 imageries have been widely used owing to its high resolution with wide coverage and several studies have demonstrated their successful applications in landslide mapping (e.g. Borghuis et al. [2007]; Sato et al. [2007]). Similarly, image interpretations from higher imageries of IKONOS (e.g. Kim et al. [2010]; Nichol and Shaker [2006]) and Quickbird (e.g. Chadwick et al. [2005]; Owen et al. [2008]) allow a very detailed preparation of landslide inventory. With the most recent WorldView-1 and 2 imageries (spatial resolution: 1.8m for multi-spectral bands, 0.5m for panchromatic band) and equivalent GeoEye-1 images (spatial resolution: 1.65m for multi-spectral bands, 0.41m for panchromatic band, see an example imagery in figure 2.2), the accuracy for landslide mapping and hazard assessment can be furthermore improved, considering that more terrain features can be clearly

Figure 2.2: The panchromatic band of GeoEye-1, a new generation of VHR imagery with spatial resolution of 0.41m. The image is rendered for the view of a landslide in Pistoia, central Italy.

distinguished. In particular, Saba et al. [2010] have demonstrated a successful spatial and temporal landslide detection with an integration of all above mentioned VHR imageries. Besides, it is also mentioned by Kouli et al. [2010] that these VHR imageries could be additionally used for a detailed land-use correction for the subsequent hazard zonation. In addition, Casagli et al. [2009] have shown that how VHR imageries can be integrated in protecting archaeological site of Machu Picchu area in Peru, which is strongly under the threat of surrounding landslides.

2.3 Satellite and ground-based SAR interferometry

SAR interferometry (InSAR) is nowadays an important branch of remote sensing. It represents the technique that uses the phase content of radar signals for extracting information on deformations of the Earth's surface [Gens and Genderen, 1996]. Satellite InSAR is a typical example of repeat-pass interferometry which combines two or more SAR images of a same portion of terrain from slightly displaced passes of the SAR sensor at different times [Massonnet and Feigl, 1998]. It plays an important role in landslide mapping and monitoring applications, owing to its capability of detecting ground movements with millimeter precision [Corsini et al., 2006; P.Canuti et al., 2007; Rott and Nagle, 2006; Squarzoni et al., 2003]. The traditional InSAR processing approach for ground movement detection is mainly focused on the differential InSAR (DInSAR) technique [Massonnet and Feigl, 1998; Rosen et al., 2000]. It uses two corresponding interferograms

for differential measurements by comparing the possible range variations of two phases with the capability of detecting terrain motions with sub-centimetric accuracy. Several works have indicated the usefulness of DInSAR in landslide studies [Catani et al., 2005a; Fruneau et al., 1996; Rott et al., 1999; Singhroy et al., 1998; Strozzi et al., 2005; Ye et al., 2004].

With the development of different techniques of satellite InSAR, ground-based SAR interferometry (GB-InSAR) has also been built up for landslide studies. The principle of GB-InSAR is similar to satellite InSAR however with different spatial and temporal scale [Canuti et al., 2004]. Besides, the recently-developed GB-InSAR devices are designed advantageously for portability and easy installation. GB-InSAR shows its potential in landslide risk management. The conventional application is to monitor landslide from multi-temporal deformation maps retrieved from a sequence of interferograms, thus facilitating the understanding of the dynamics of unstable slopes. The usefulness of GB-InSAR in landslide monitoring is well documented in several studies using different devices, including continuous-Wave Step-Frequency (CW-SF) radar [Luzi et al., 2004, 2006; Pieraccini et al., 2003], the system LISA (Linear SAR) developed by the Joint Research Center of European Commission [Antonello et al., 2004; Canuti et al., 2004; Corsini et al., 2006; Leva et al., 2003; Tarchi et al., 2003a,b] and the equipment from IDS-Ingegneria dei Sistemi [Noferini et al., 2005, 2006, 2007, 2008]. In particular there are several novelties in these recent studies. For example, Noferini et al. [2005, 2006, 2008] have demonstrated the efforts to extract coherent pixels (in principle similar to persistent scatterers for satellite InSAR) from multi-temporal acquisitions in order to locate the landslide affected areas. Moreover, Herrera et al. [2009] have shown the potential of GB-InSAR

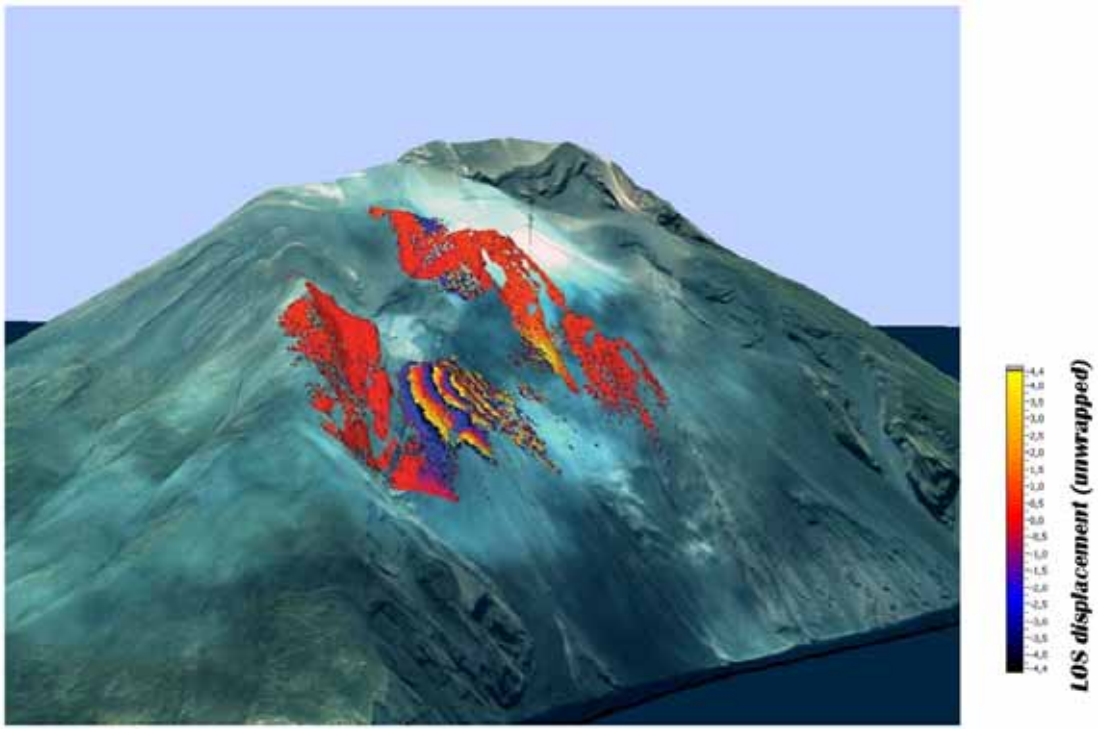

Figure 2.3: The Stromboli Volcano: the result of interferogram analysis with millimetric accuracy using LiSA GB-InSAR system [Casagli et al., 2008]

in landslide prediction: in particular the monitoring data from GB-InSAR can be correlated to rainfall data and the prediction can be made in a viscoelastic sliding-consolidation model. In addition, Luzi et al. [2009] have reported a potential use of GB-InSAR to get the depth of snow on a slope from the behavior of phase variation.

The GB-InSAR is also crucial for the establishment of an early warning system which aims at a maximum mitigation of the damages caused by sudden events. A successful application was demonstrated in the real-time monitoring of Stromboli Volcano in 2002 and 2003 [Casagli et al., 2008], by means of the LiSA system [Antonello et al., 2004; Canuti et al., 2004; Corsini et al., 2006;

Leva et al., 2003; Tarchi et al., 2003a,b]. After a large landslide occurrence on 30 December 2002, the system was installed on the northwestern flank of Stromboli and started real-time monitoring from 20 February 2003. The system enabled a sending of synthesized radar images with 2m resolution every 12 minutes from the instrument. Displacements were then calculated along the sensor's line-of-sight (LOS) from the generated consecutive interferograms and the deformation maps are produced with millimetric accuracy (figure 2.3). The collected data covered an area of 2 km^2 and were sent to the Italian Civil Protection in the near real-time. Actually, it is also possible to distinguish the interaction of different geomorphic processes within the monitoring periods which can be ideally extended to several years.

2.4 Airborne and terrestrial laser scanning

The active sensor of laser scanning, also known as Light Detection and Ranging (LiDAR), has been largely used for landslide studies in recent years, especially with the increasing improvements in vertical and horizontal accuracy, and its usefulness in high resolution topographic mapping.

The airborne laser scanning is suitable for the study over a large area with one-time flying data acquisition. A common use of airborne laser scanning is to generate a high resolution DTM from the highly-accurate raw point cloud data. Although potential information loss during the data interpolation, the accuracy of generated DTM can be bettered by technical improvements in collected points density, and in several sophisticated interpolation routines.

The derived high resolution LiDAR DTM and its derivatives (hillshade, slope,

curvature etc.) are widely used in characterizing terrain features and landforms, useful for landslide identification and mapping, thanks to its provided details and accuracies [Corsini et al., 2009; Haugerud et al., 2003; Schulz]. Also, topography information extracted from LiDAR DTM enables a characterization of landslide features which is not able to be detected by aerial-photos due to the forest canopy [Haugerud et al., 2003]. Some successful case studies have been reported in landslide identification and mapping applications of airborne laser scanning [Ardizzone et al., 2007; Baum et al., 2005; Eeckhaut et al., 2007; Schulz, 2007]. Besides, several studies have indicated the potential use of LiDAR DTM in landslide volume estimation [Chen et al., 2006; Corsini et al., 2009; Derron et al., 2005; Scheidl et al., 2008].

Some particular studies include the effort of McKean and Roering [2004], who attempted to identify landslides using surface roughness measurement, performing the Laplacian operation on a LiDAR DTM. Also, Glenn et al. [2006] have extracted surface roughness, semivariance and fractal dimension directly from raw point data for the purpose of keeping original quality and subsequently utilize these morphometry parameters in landslide characterization (e.g. activities, motion, material and topography). Besides, Booth et al. [2009] have developed an innovative approach to automatically map landslides using signal processing techniques of Fourier transform on LiDAR DTM. Moreover, Trevisani et al. [2009] have performed geostatistical techniques, employing variograms maps as spatial continuity indexes on LiDAR DTM, in order to characterize the surface morphology. Additionally, Corsini et al. [2009] have rendered a quantification of mass wasting from a sequential DTMs generated from multi-temporal scanning acquisitions.

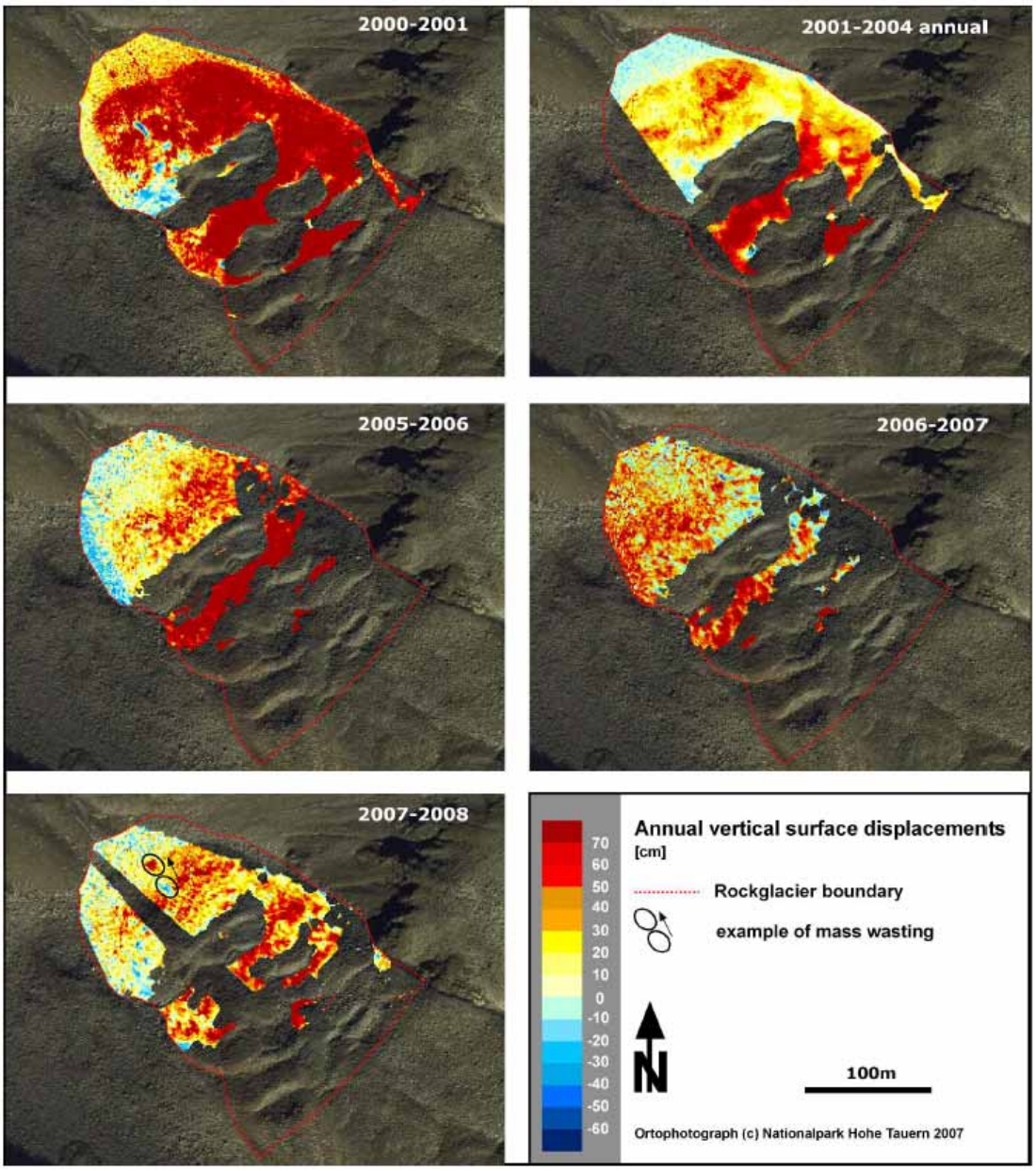

Figure 2.4: An example of monitoring annual surface displacement through temporal laser scanning at the cirque Hinteres Langtal, Austria as illustrated by Avian et al. [2009]

Apart from airborne LiDAR, the terrestrial laser scanning is also helpful to landslide studies, with the increasing portability and design of the scanning instrument. The prevalent approach is to estimate landslide displacement, observing morphological changes and understanding the failure mechanism from point data [Abellan et al., 2009; Oppikofer et al., 2009; Teza et al., 2007, 2008] and interpolated surface [Avian et al., 2009; Baldo et al., 2009; Prokop and Panholzer, 2009]. Another important note, since the terrestrial laser scanning is relatively easier to be regularly arranged and scanned, it can be used as an alternative approach for the monitoring of landslide morphologic and volumetric evolution [Avian et al., 2009; Jones, 2006; Oppikofer et al., 2009; Prokop and Panholzer, 2009; Rowlands et al., 2003; van Westen et al., 2008]. An example of Avian et al. [2009] for monitoring mass movement by temporal acquisitions is illustrated in Figure 2.4.

In particular, Teza et al. [2007] have introduced an automatic approach to measure landslide displacement using iterative shape matching from multi-temporal point clouds. After, combined with a strain field computation, Teza et al. [2008] enables a characterization of the kinematics of ground surface for mass movements, aiming at a detailed analysis of landslide behaviour. Furthermore, Prokop and Panholzer [2009] showed that terrestrial laser scanning is useful for monitoring slow-moving landslides with displacement rate changes < 50mm.

Besides, the terrestrial laser scanning is well used in monitoring rockfall hazards, which enables a detection of displacement with millimeter accuracy from sequential raw data. Also, using the software of Coltop3D [Jaboyedoff et al., 2007], it is able to extract detailed structural features with the point clouds acquired from the upper part of cliffs for rockslide characterization [Oppikofer et al.,

2009], similar to Sturzenegger and Stead [2009], who presented an effort to quantify discontinuity orientation and persistence on rock slopes. Additionally, Lato et al. [2009] utilized a mobile scanning system at a speed up to 100km/h to ensure a constant monitoring of rockfall movement from geomechanical structural feature identification and kinematic analysis.

2.5 Conclusion

This chapter renders an overview of the contributions of remote sensing to landslide researches from the past published works, particularly regarding those works of aerial-photos, optical satellite sensors, SAR interferometry and laser scanning. These remote sensing techniques show their usefulness in different stages of landslide studies, such as landslide mapping, detection, monitoring ,investigation and so on.

The visual interpretation of aerial-photos is conventional but still effective, owing to its capability of 3D interpretation and high spatial resolution. In terms of satellite remote sensing within optical electromagnetic, their utilities for landslide studies are strongly limited by traditional sensors with low spatial resolution. However, the new generation of VHR imageries show their potential in accurate landslide mapping and following hazard assessment. The InSAR techniques, including both satellite sensors and ground-based instruments, have strong ability in detecting and monitoring ground mass movements, especially those displacements within millimeter precision which can hardly be detected by aerial-photos and optical images. In addition, laser scanning from both airborne and terrestrial acquisitions have demonstrated the capability in capturing high resolution

topographic parameters, enabling a detailed feature characterization for landslide identification, mapping and monitoring.

The development of remote sensing techniques is always rapid. New techniques and data are often developed and become available in very short time. The continuous focus and discovery over newly-updated approaches is necessary for different researches using remote sensing techniques. This is also what the following chapters will mainly focus: the novelty brought by new technique of remote sensing in landslide applications.

Chapter 3

Object-Oriented Analysis (OOA) for mapping of rapid-moving landslides

A complete multi-temporal landslide inventory, ideally updated after each major event, is essential for quantitative landslide hazard assessment. However, traditional mapping methods, which rely on manual interpretation of aerial-photos and intensive field surveys, are time-consuming and accordingly not efficient for the generation of such event-based inventories. In this chapter, a semi-automatic approach based on object-oriented change detection for landslide mapping, and using very high resolution (VHR) optical images, is introduced. The approach was specifically developed for a mapping of rapid-moving (velocity $>$ 1.8m/hour, according the scale of [Cruden and Varnes, 1996]) shallow landslides and debris flows. The usefulness of this methodology is demonstrated on the Messina landslide event in southern Italy that occurred on 1 October 2009. The algorithm

was first developed in a training area of Altolia, and subsequently tested without modifications in an independent area of Itala. 198 newly-triggered landslides an debris flows were correctly detected, with user accuracies of 81.8% for the number of landslides, and 75.9% for the spatial extent of landslides. The principal novelty of this work is (1) a fully automatic problem-specified multi-scale optimization for image segmentation, and (2) a multi-temporal analysis at object level with several systemized spectral and textural measurements.

This chapter is organized in eight sections. The first section gives the background of object-oriented analysis (OOA), including a comparison of traditional pixel-based analysis and novel OOA approach. The second section is to define the research gap and propose the major research questions. It reviews the application of OOA in landslide studies and then defines the main purpose of this study. The third section proceeds with the case study area. The fourth section renders an overview over the flowchart and the datasets used. The fifth section introduces a new approach of image segmentation systemized with multi-scale optimization. The sixth section is going through the classification of landslide objects, including the preliminary selection of landslide candidate objects and the following removal of false positives. The seventh section shows the result of this object-oriented approach with subsequent accuracy assessment. The final section summarizes the whole chapter regarding the application of OOA in landslide mapping.

3.1 What is OOA?

OOA is mainly dealing with the measuring unit of 'object'. The term 'object' inside OOA can be defined as 'individually resolvable entities located within a

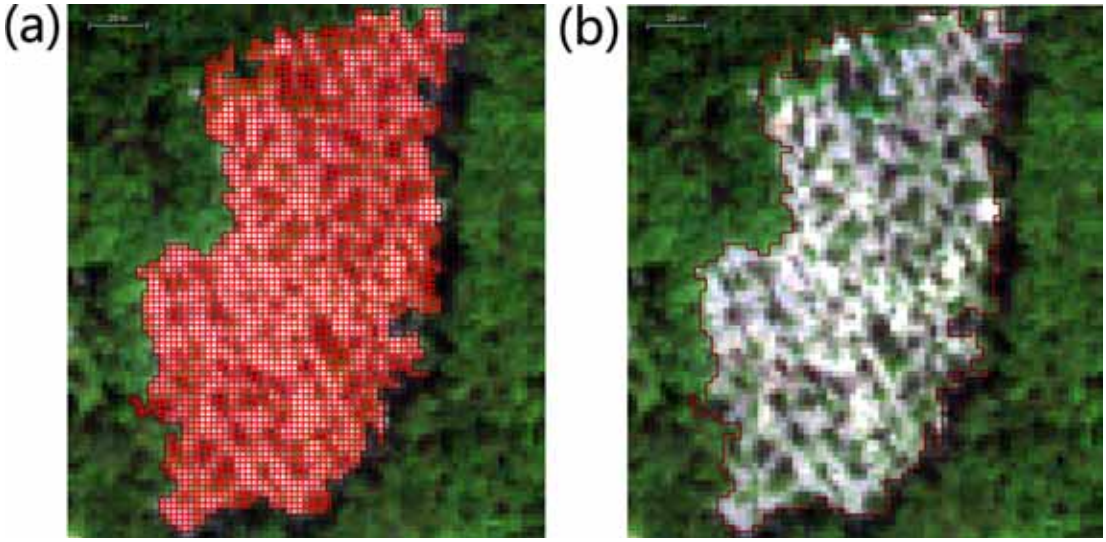

Figure 3.1: The concept of OOA illustrated in GeoEye-1 VHR imagery over a landslide near Pistoia, Italy. (a) The landslide is analyzed at the pixel level. (b) The landslide is rendered at the object level.

digital image which are perceptually generated from high-resolution pixel groups' [Hay and Niemann, 1994; Hay et al., 1997, 2001, 2003]. In detail, OOA initiates with a image segmentation approach that spatially divides the digital image (including remote sensing imagery) into several homogeneous segments which contain high spectral autocorrelation, so as to form these 'objects', and the following analysis can be then performed on the unit of these segmented objects instead of original pixels [Benz et al., 2004; Hay et al., 2003]. Figure 3.1 renders an example of analyzing a landslide at both pixel (figure 3.1(a)) and object levels (figure 3.1(b)), for a landslide occurred near Pistoia in Italy from a VHR imagery of GeoEye-1.

3.1.1 What's wrong with pixels?

In general, the traditional approach of analyzing optical remote sensed imagery, which has been prevalently used for the pasting 30 years, is based on pixels of multi-spectral bands. However, this pixel-based approach sometimes shows its limitations in the image analysis, not only due to those traditional problems related to geometry, pixel mixture, point spread functions and resampling [Cracknell, 1998], but also the weakness in describing the complex targets which seem to exist 'beyond pixels'. Especially for the latter, those weaknesses can be elaborately summarized as follows.

Firstly, the pixel-based approach, including both per-pixel and sub-pixel analysis, chiefly shows its usefulness when pixels sizes are similar to or coarser than the targeted objects of interest [Blaschke, 2010]. However, with the increasing development and availability of VHR images, which bring huge improvement in spatial resolution (e.g. Worldview-1: 0.44m panchromatic; GeoEye-1: 0.41m panchromatic) and wide applications in different study purposes, the only focus on pixels is possibly not sufficient because a targeted object can be represented by a large number of pixels. These pixels need to be further grouped into, so-called 'objects', for a more systematic and accurate characterization. Also, it should be noticed that pixel-based analysis on VHR imagery introduces the potential disturbance of noises and artefact, such as those 'salt-and-pepper' effects.

Secondly, pixel-based image analysis is exclusively employing the approach with statistical analysis of pixels based on their spectral responses, however without a consideration of contextual properties of these pixels [Benz et al., 2004; Flanders et al., 2003]. This leads to the difficulty in calculating some features of

targeted objects, such as those textual behaviors, which can hardly be extracted without a definition of object context. Also, pixel-based approach fails to render the shape and the spatial relationship between neighboring pixels or distant image regions, especially for high resolution imagery, whose neighboring pixels are possibly having the same spectral behavior if only considering the classification of multi-spectral bands [Blaschke, 2003].

Thirdly, as indicated by Hay et al. [2003], scale is the critical part of image understanding for pattern recognition, and it can be described as a 'window of perception'. However, the traditional approaches of analyzing remote sensing images based on pixels fail to explicit the scaling laws which define a scale to and from an image, the number of classes to be dealt with, and the suitable upscaling approach to employ [Hay et al., 2001]. That is, the pixel-based approach only has the ability to analyze image with one scale. Therefore, it is difficult describe different characteristics of each targeted object, since these characteristics appear diversely with different visualizing and analyzing scales. Moreover, it is troublesome for pixel-based approach to analyze different objects with different scales, considering that these objects usually have their own inherent scale and are not necessarily remaining as same [Burnett and Blaschke, 2003]. These problems limit the understanding of image at different scale levels and multiple hierarchies in simultaneous time.

In sum, the only focus of image analysis on pixels cannot adequately provide the reliable pixel unit, and cannot represent potential spatial, contextual and multi-scale environment for a specified analysis. This brings the request for a more advanced approach possibly processed 'beyond pixels', which is the essence of OOA approach to be introduced in this chapter.

3.1.2 The advantages of OOA

Compared to the traditional pixel-based analysis, OOA nevertheless represents a more advanced image analysis approach, gaining benefits from several advantages listed in the following:

- OOA represents a more advantageous approach for analyzing VHR remote sensing data because image pixels can be meaningfully grouped into networked homogeneous objects, and noise can be consequently reduced [Benz et al., 2004; Blaschke, 2010].

- OOA is not only focusing on the spectral statistics of pixels, but instead an inclusion of neighboring and surrounding pixels, thus allowing a further contextual analysis such as textural, spatial and shape measurement.

- OOA provides a multi-scale hierarchical approach which is closer to real-world entities and is more fitting to human vision and perception. This is also in accordance with the prerequisite of a knowledge-based analysis.

- OOA enables a powerful but low-cost computation [Hay et al., 2005]. In particular, in many applications OOA shows the potential in automatic and semi-automatic image analysis for targeted objects extraction (e.g. al Khudairy et al. [2005]; Castilla et al. [2008]; Diaz-Varela et al. [2008]; Ehlers et al. [2003, 2006]; Lackner and Conway [2008]; Pascual et al. [2008]; Weinke et al. [2008]; Zhang et al. [2005]).

It should also be noted that, although the existence of several OOA-based analyzing softwares, in recent years primary OOA studies for remote sensing

imagery, including the following work described in this chapter, have been carried out using the software of Definiens eCognition [Definiens, 2010].

3.2 Problem definition

As already indicated in Chapter 2, traditionally, landslide mapping has relied on visual interpretation of aerial-photos and intensive field surveys. However, for mapping of large areas those methods are too subjective, time-consuming and not always easy to be carried out, creating a gap that remote sensing has been increasingly filling. Due to restrictions in spatial resolution, traditional optical satellite imagery, such as acquired by Landsat TM, has limited utility for landslide studies [Hervas et al., 2003]. More recently, high resolution images and LiDAR derivatives have started to offer an alternative way for effective landslide mapping.

However, most researches of landslide mapping using above-mentioned remote sensing data and imagery, have been focusing on pixel-based analysis. For example, Borghuis et al. [2007] have employed unsupervised image classification in automated landslide mapping using SPOT-5 imagery. Besides, McKean and Roering [2004] also successfully delineated landslide features using statistical measures of surface roughness from LiDAR DTM. Moreover, Booth et al. [2009] detected and mapped 82% of landslides in the inventory using Fourier and continuous wavelet transformation on 1m LiDAR DTM. With increasing spatial resolution, however, pixel-based methods have fundamental limitations in addressing particular landslide characteristics due to finite spatial extent. Only those object characteristics allow landslides to be further assigned to different type classes, and other features of similar appearance to be discarded. Such methods focusing

on features instead of pixels are the basis of object-oriented analysis (OOA).

OOA, the approach employing initial image segmentation and subsequent analysis and classification of the image objects, on the other hand, offers a more reliable way to analyze high resolution remote sensed data, considering that image pixels are spectrally merged to systemized objects with a removal of 'salt-and-pepper' noises [Benz et al., 2004; Blaschke, 2010]. Moreover, OOA offers a potentially automated approach for landslide mapping, with a consideration of spectral, morphological and contextual landslide features supported by expert knowledge [Martha et al., 2010], thus allowing a cognitive approach comparable to visual image analysis. Nonetheless, so far few studies have focused on OOA-based landslide mapping. Preliminary efforts by Barlow et al. [2003] and Martin and Franklin [2005] focused on automatic landslide detection using low resolution Landsat ETM+ images. The methodology was further improved by Barlow et al. [2006] through the use of higher resolution SPOT-5 data, as well as an inclusion of more robust geomorphic variables. Also, Moine et al. [2009] have proposed a complex set of spectral, shape and textural features for automatic landslide characterization from aerial and satellite images. Additionally, Martha et al. [2010] developed an algorithm which integrates spectral, spatial and morphometric properties of landslides, and successfully recognize 76.4% and classify 69.1% of five different types of landslides in difficult terrain in the High Himalayas. These studies show the increasing utility and potential of OOA in detecting and mapping landslides automatically and rapidly. However, all of the proposed approaches tend to fail in situations where both fresh and older landslides are present and prevent an accurate event-related landslide inventory.

A potential solution could be the integration of pre-event image data. Change

detection from satellite imagery before and after a landslide event has already been proven useful for identification of newly-triggered landslides at a pixel-based level. Most frequently change detection has been based on image ratios and image differencing with a defined threshold [Hervas et al., 2003]. Additionally, image subtraction and post-classification comparison have been attempted. For example, Nichol and Wong [2005] have reported that a post-classification comparison using a maximum likelihood classifier produced a detection rate of 70%. Park and Chi [2008] have introduced the concept of change detection into OOA, using VHR images before and after landslide occurrence. However, their identification of changes was exclusively based on subtractive image differencing, i.e. a direct comparison of average spectral measurements from pre- and post-event images. Their aim is only to recognize change/non-change objects, without further efforts to remove those potential false positives from 'change' objects. The approach is apparently only suited for situations where all major changes are induced by landslides and all landslides occurred in forested terrain.

Therefore, the purpose of this work is to introduce a new approach for a rapid mapping of newly-triggered landslides using an objected-oriented change detection technique. The methodology aims at a semi-automatic and rapid analysis with a minimum of operator involvement and manual analysis steps. Compared to conventional approaches for landslide mapping, this approach benefits from (1) an image segmentation with problem-specified scale optimization, and (2) a multi-temporal analysis at object level with several systemized spectral and textural metrics.

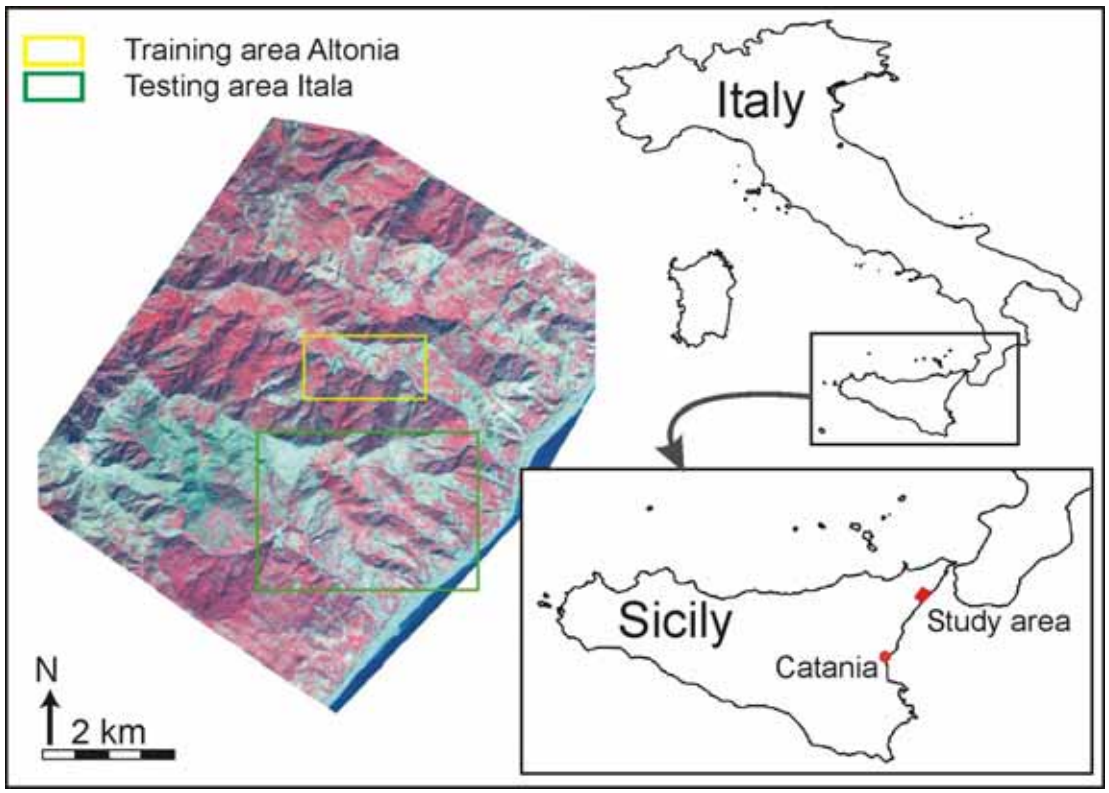

Figure 3.2: The location of the case study area, including a training area of Altolia and a testing area of Itala.

3.3 Study area

The application of this OOA approach for landslide mapping is demonstrated from a case study in the Messina province of Sicily, southern Italy of Sicily Region (figure 3.2).

3.3.1 Geographical, geological and geomorphological settings

The Province of Messina is located in the northeastern Sicily Region, with a total territory area of 3247 km^2. The capital of the province is the Messina city. The Messina province is divided by the Peloritani Mountains into two parts: the Tyrrhenian part in the north and the Ionian part in the east, with respectively 150 km and 68 km coastline. Along each of the coastline, several catchment areas were formed, with the channeled streams flowing into the Tyrrhenian and Ionian seas.

The detailed descriptions of geological settings for this area can be primarily found from several previous literatures and studies [Antonioli et al., 2006; Lentini et al., 1995; Monaco and Tortorici, 2000; Punturo et al., 2005; Somma et al., 2005], and summarized in the report of Italian civil protection [Civil-Protection, 2009] in the following: the Province of Messina is belonging to the mountain system of Peloritani which created the southern tip of the Calabrian-Peloritano Arch. The mountain systems was developed from the converging and collision processes between the African and European plates which determined in the course of time a complex structure of overlapping beds and tectonic flakes. The area is accompanied with land outcrops which were formed by the deformation of the original European edge due to continental crust consisting of crystalline rock. These sediments over the crystalline basement, which started from the quaternary floods to intramiocenic pelitic and conglomeratic sediment, were sedimented in land surfacing areas of clay and sand. Marine and fluvial Terraces can be largely found in the Peloritani Mountains, (Pleistocene superior) indicating the final

phase of the typical orogeny of this area. The deposits were chiefly formulated by gravel, sand, lime or possibly only abrasion plains [Antonioli et al., 2006; Civil-Protection, 2009; Lentini et al., 1995; Monaco and Tortorici, 2000; Punturo et al., 2005; Somma et al., 2005].

The geomorphological condition of the area is in poorly-developed state: a very intensive erosion activities especially strong during significant and long lasting hydrometric events when the degradation of the soil is changed in its diverse aspects by the pervasive rain water. The extraordinary rainfall fall in short time periods and under special hydro-geological circumstances often brings about a natural vulnerability to trigger potential disaster, such as landslides and floods [Civil-Protection, 2009].

3.3.2 The landslide event

The landslide event of Messina was triggered by heavy rainfalls during the period 16 September to 1 October 2009 (figure 3.3). On 16, 23 and 24 September 2009, the northeastern Sicily was continuously hit by heavy rainfalls, resulting in a saturation of terrain. During the night of 1 October 2009, a strong storm accompanied with even more intensive prolonged rainfall, ca. 223 mm in 7 hours, again affected several catchments south of Messina city along the Ionian side, including several municipalities of south Messina, Scaletta Zanclea, Itala and Ali Terme. Numerous landslides were consequently triggered as a result of steep slopes with saturated state of the soil, with most of them as rapid shallow landslides and debris flows (figure 3.4). These landslides were sliding and flowing into the populated inhabited areas, and 31 people were reported dead, with ad-

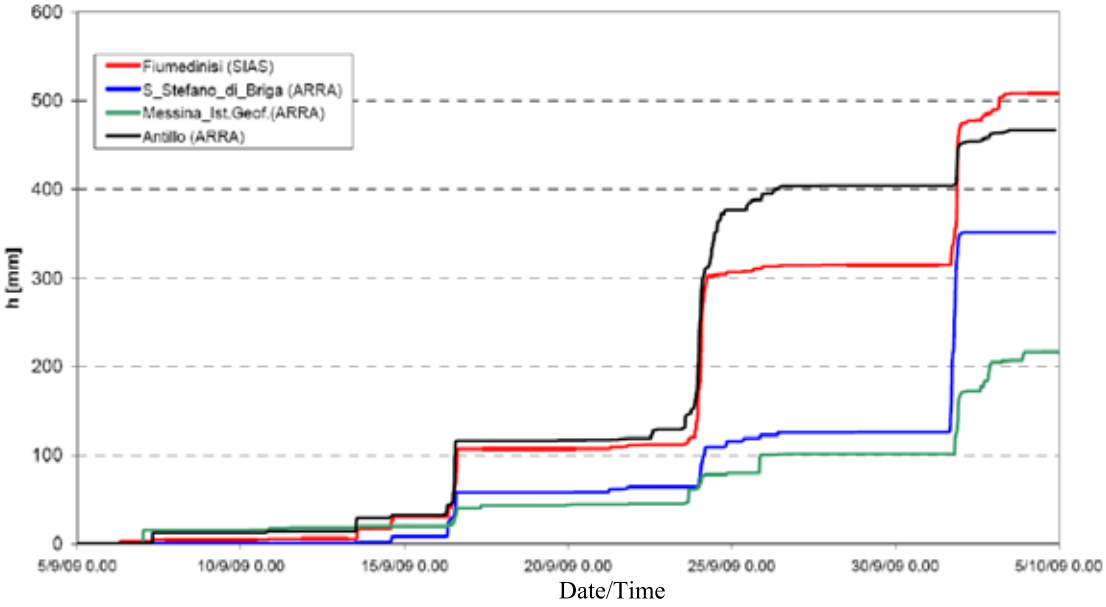

Figure 3.3: For the landslide event of Messina on 1 October 2009, accumulation of precipitation were recorded by four different weather stations nearby before and after the event. [Civil-Protection, 2009]

ditional 6 people missing. Besides, 122 people were injured and 2019 people were evacuated emergently. The event has caused huge damages to buildings and other infrastructures (figure 3.5). A total of 550,000,000 euros of direct damages were estimated with additional estimated 48,936,978 euros for operational costs [Civil-Protection, 2009].

The event caused severe damages to several towns, which were isolated due to the destruction of roads and railways. Two of the most damaged areas were studied, including a training area of Altolia (ca. 1.8 km^2) for algorithm development, and a larger independent testing area of Itala (ca. 8.1 km^2, see detailed locations in 3.2). The latter allows the robustness and transferability of the algorithm (without any change of ruleset and threshold) and the corresponding accuracy to be assessed by comparison with a manually mapped landslide inventory prepared

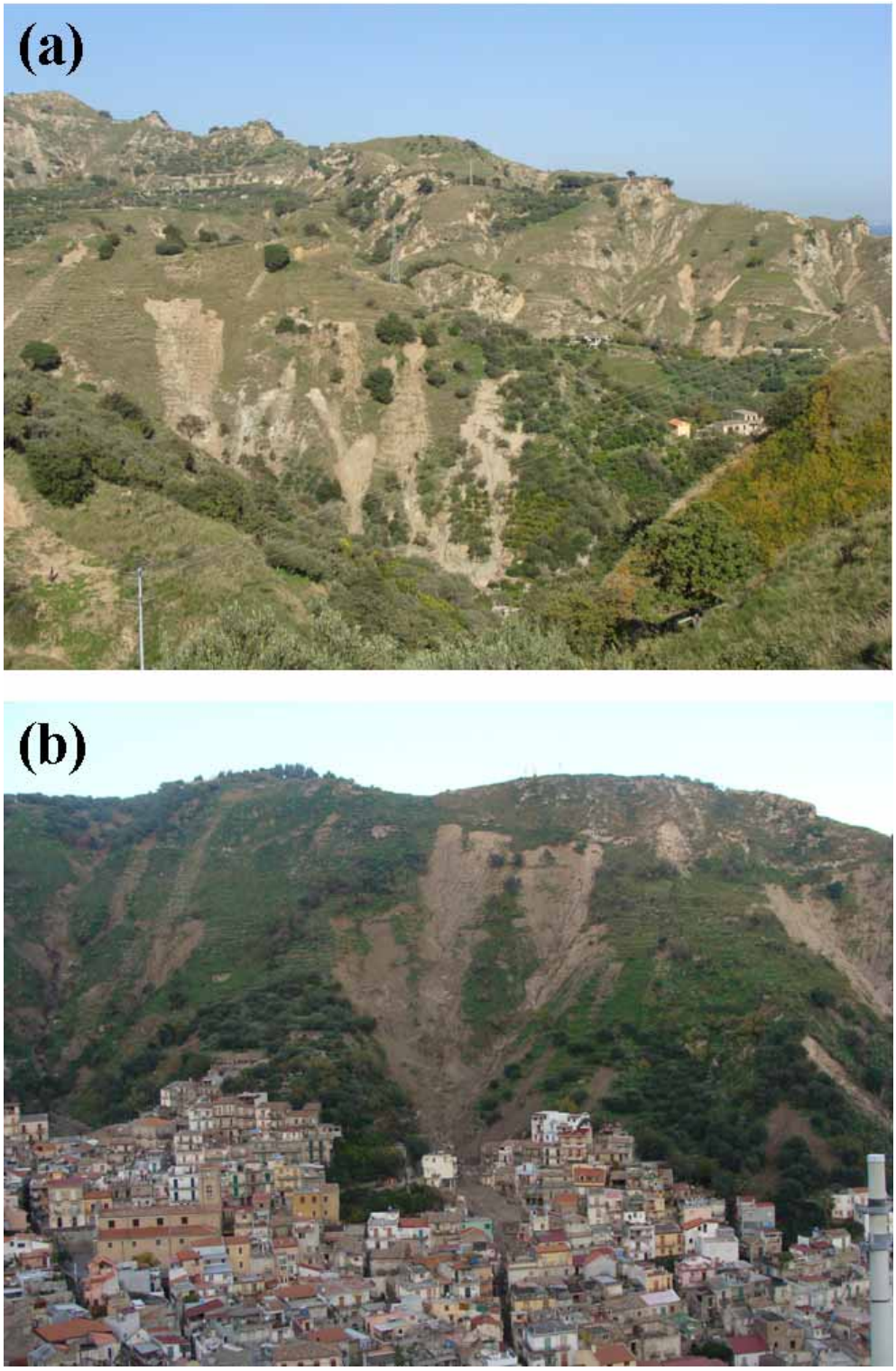

Figure 3.4: A view of numerous triggered landslides in the town of Giampilieri.

Figure 3.5: A view of the damages to the buildings caused by landslides.

from field works and subsequent modifications from image interpretation.

3.4 Flowchart and dataset

3.4.1 General flowchart

The adopted methodology for landslide mapping includes two parts: (1) image segmentation with multi-scale optimization, and (2) classification of landslide objects. The general methodology is shown in figure 3.6.

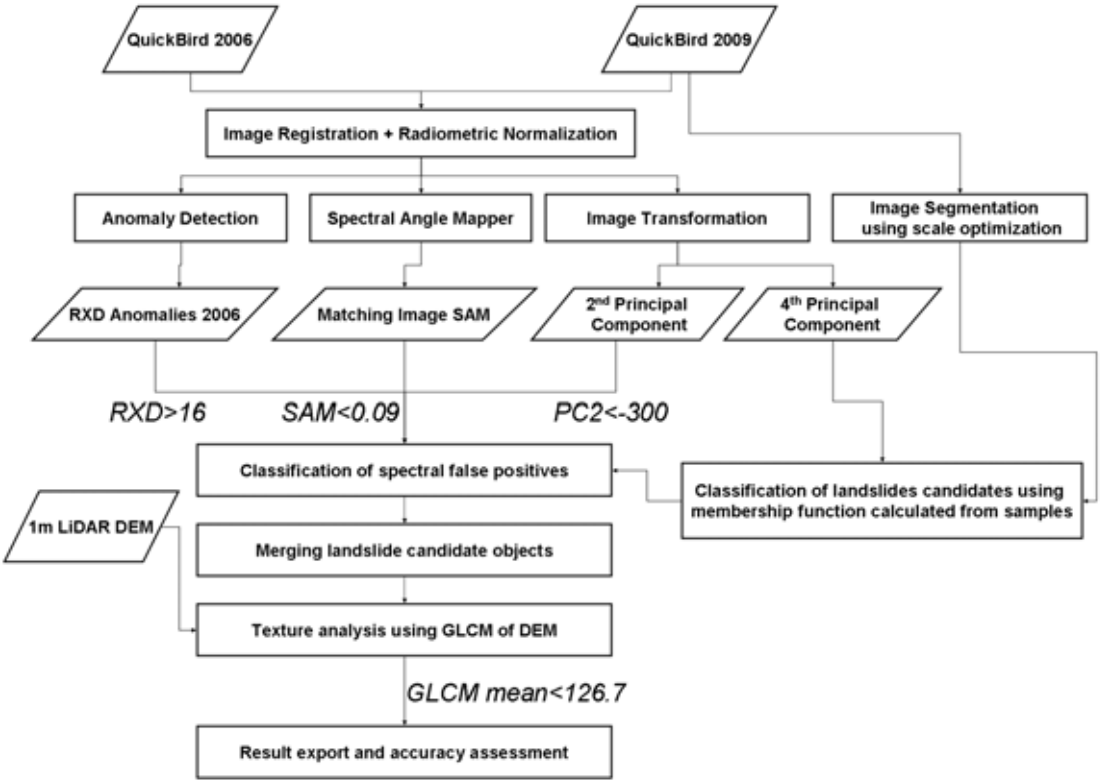

Figure 3.6: General flowchart of landslide mapping by OOA change detection. RXD: Reed-Xiaoli Detector; SAM: Spectral Angle Mapper; PC: Principal Component; GLCM: grey level co-occurrence matrix.

3.4.2 Dataset

Two QuickBird images were used in the study, acquired on 6 September 2006 and 8 October 2009, with respectively 0.3% and zero cloud cover (figure 3.7). For each image, only four multispectral bands (Blue: 450-520 nm, Green: 520-600 nm, Red: 630-690 nm, NIR: 760-900 nm) with the spatial resolution of 2.4 m were used. The panchromatic band (450-900 nm) was not used for pansharpening because of a reduction of computation time in ruleset development and testing. Also, the 2.4m spatial resolution of multi-spectral band is sufficient for landslide mapping given the dimension of these newly-triggered landslides. Additionally, a

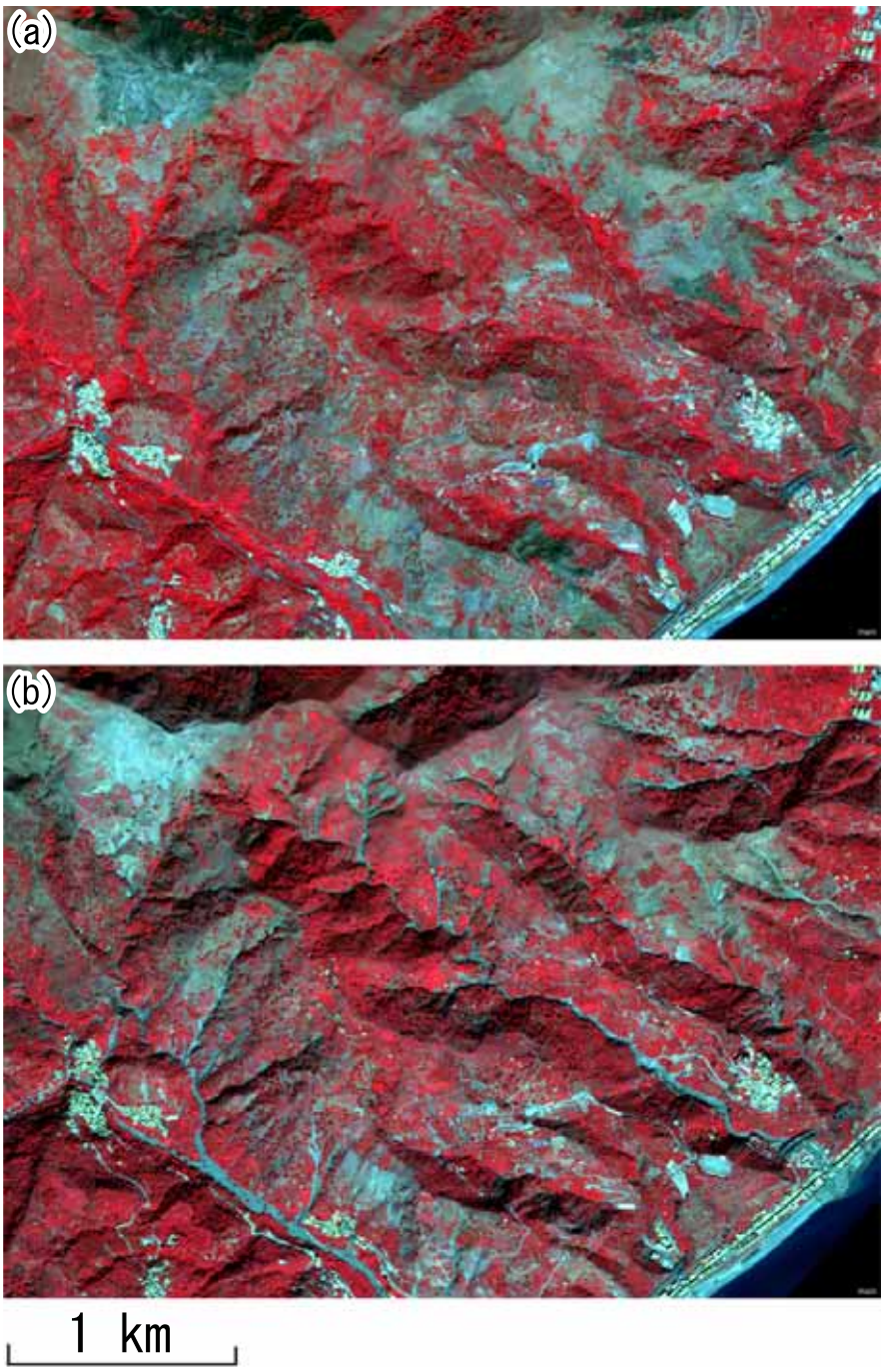

Figure 3.7: The used Quickbird imageries: (a) pre-event QuickBird imagery, (b) post-event QuickBird imagery (false color 4-3-2)

1m DTM was created from airborne LiDAR data acquired during 6 to 19 October 2009, shortly after the event, with a maximum point density of 8 points/m^2 (vertical and horizontal accuracy: 15cm and 40cm, 1-σ). The spectral analysis was performed with ENVI 4.7 software. The OOA and textural analysis were implemented in Definiens eCognition Developer 8.

3.5 Image segmentation with scale optimization

Image segmentation defines the building blocks for object-oriented image analysis and, to ease further analysis, should aim at meaningful delineation of targeted real-world objects. However, considering the complex characteristics of each single landslide, including land cover variance, illumination difference, diversity of spectral behavior and size variability, it is difficult to delineate each individual landslide as a single object [Martha et al., 2010]. Notwithstanding this difficulty, over- and under-segmentation can be reduced by means of a multi-scale optimization approach.

The multi-resolution segmentation based on Fractal Net Evolution Approach (FNEA) described by Baatz and Schaepe [2000] and implemented in Definiens eCognition software [Benz et al., 2004; Definiens, 2010], is employed for the initial segmentation, parameterized according to the specific needs of event-based rapid mapping of landslides, and incorporated in a multi-scale optimization routine. The FNEA approach requires the user to define weights for input layers (bands), as well as appropriate heterogeneity criteria. The targeted landslides are present in the post-event image, and consequently only the second QuickBird scene was used as an input for segmentation. The main change observed results

from removal of vegetation, and consequently a high ratio between the red and the near-infrared (NIR) bands is a typical feature of newly triggered landslides [Rau et al., 2007]. These bands are also least affected by atmospheric effects and were assigned with equal weights for the segmentation procedure.

FNEA is a region-growing segmentation algorithm, starting from individual pixels and merging the most similar adjacent regions as long as the internal heterogeneity of the resulting object does not exceed the user defined threshold scale parameter f. The scale parameter f is calculated as:

$$f = (1 - w_s) * H_{color} + w_s * H_{shape} \tag{3.1}$$

and it comprises color heterogeneity H_{color} and shape heterogeneity H_{shape} with user-defined weight of shape w_s. H_{color} is defined as:

$$H_{color} = \sum_{i=1}^{N} w_i * \sigma_i \tag{3.2}$$

where N is the number of input layer for segmentation, w and σ are respectively weight and standard deviation of input layer i.

Due to great variety of landslide shape, H_{shape} is excluded from the segmentation procedure by setting it to 0. Thus, 3.1 becomes

$$f = H_{color} = \sum_{i=1}^{N} w_i * \sigma_i \tag{3.3}$$

Since each input band in this study was treated as the same weight w_c, the scale

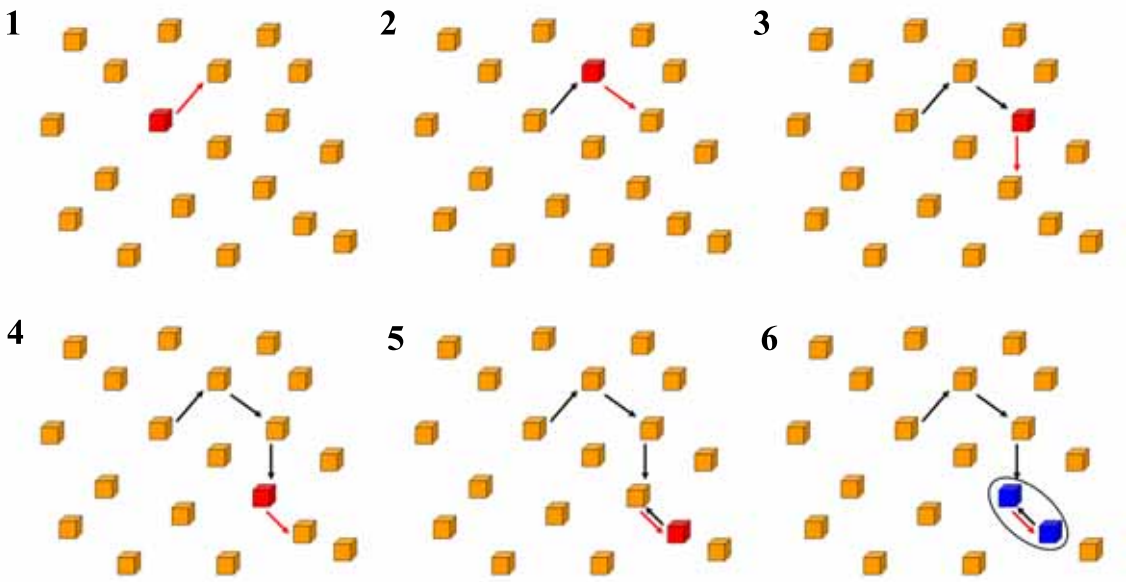

Figure 3.8: A sketch of the Fractal Net Evolution Approach (FNEA) approach for image segmentation. Each object employs the homogeneity algorithm to find the best neighbor (red) to continue the merging branch. The merging algorithm repeats until each branch finds the best merging object (blue) fitting the scale parameter f.

parameter is consequently defined as

$$f = \sum_{c} w_c(n_{mrg} * \sigma_{c,mrg}) - (n_{o1} * \sigma_{c,o1} + n_{o2} * \sigma_{c,o2}) \tag{3.4}$$

While n corresponding to the number of pixels within an object, and σ_c to the standard deviation of pixel values within the band c. The subscripts indicate objects prior to merge ($_{o1}$ and $_{o2}$) and the respective resulting object after merging ($_{mrg}$). The flowchart of FNEA can be simply sketched in figure 3.8.

FNEA is computationally efficient, enables an analysis among various user-defined scales and has been used successfully in various remote sensing studies. Nevertheless, the need to define the operational scale of the process under inves-

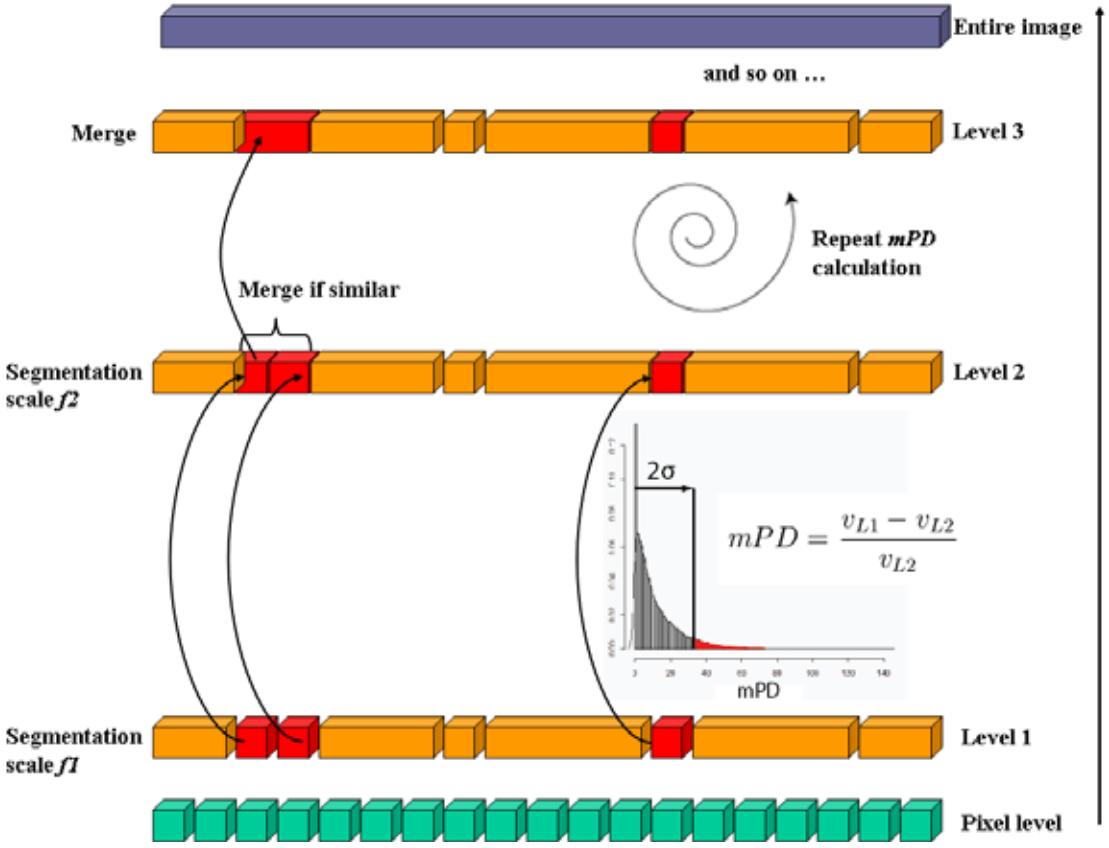

Figure 3.9: A sketch of the fully automatic approach for image segmentation with multi-scale optimization.

tigation and the corresponding scale parameter a priori or in a time consuming 'trial and error' procedure has been identified as one of its major limitations [Hay et al., 2003]. Statistical optimization methods (e.g. Dragut et al. [2009]; Espindola et al. [2006]) have been shown to allow the choice of the scale parameter to be made more objective if the targeted elements exhibit one operational scale. However, slope failures feature several orders of magnitudes in volume and area (e.g. Malamud et al. [2004]) which prohibits the definition of one single scale parameter. [Martha et al., in review] developed a modified version of Espindola's approach, by calculating a plateau objective function that has several scale parameter maxima to simplify segmentation parametrization and obtain a suitable multi-scale representation of satellite imagery. Additionally, Esch et al. [2008] proposed a multi-level segmentation optimization procedure (SOP). A modified version of this approach is used in this study (see the sketch in figure 6.2).

In an initial step the image is segmented with the above-mentioned settings and two hierarchical scales ($f1$=5, $f2$=10). The mean Percentage Difference (mPD) between sub-object level ($L1$) and super-object level (L2) is calculated as

$$mPD = \frac{v_{L1} - v_{L2}}{v_{L2}} \tag{3.5}$$

where v is the ratio of the intensities in the NIR and red band of the respective sub- and super-object. Each sub-object whose mPD exceeds the mean mPD of all sub-objects by more than 2σ is consequently classified as a real sub-object and transferred to the super-object level:

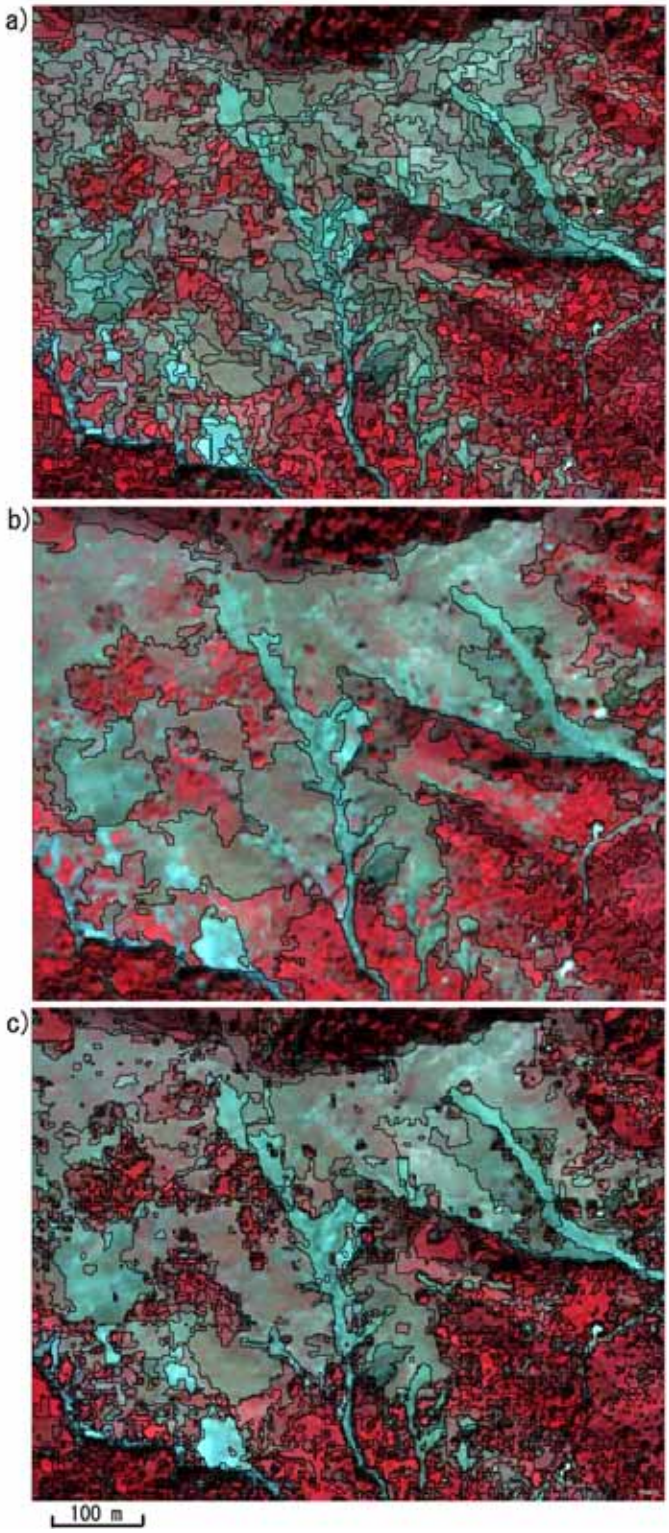

Figure 3.10: Detailed view of the image segmentation at: (a) a fixed scale of 30, (b) a specified scale of 200, (c) a described multi-scale optimization.

$$realobject = \begin{cases} 1, mPD > 2\sigma_{mPD} \\ 0, else \end{cases} \tag{3.6}$$

In this sense $2\sigma_{mPD}$ replaces the user defined thresholds introduced by Esch et al. [2008]. In a next step the similarity of transferred adjacent sub-objects ($ob1$ and $ob2$) is evaluated by their intensities difference in the NIR and red band. Similar objects are merged according to the following condition:

$$sim_{ob1,ob2} = \begin{cases} 1, (0.5 * |RED_{ob1} - RED_{ob2}| + 0.5 * |NIR_{ob1} - NIR_{ob2}|) < 10 \\ 0, else \end{cases} \tag{3.7}$$

The procedure is repeated for a total of 11 scales (15, 20, 30, 50, 70, 100, 150, 200, 300, 500, 700), where in each step the result of the previous cycle becomes the sub-object level, and according to the next larger scale factor a number of objects are merged to create a super-object level above. With each iteration further objects exceeding the initially derived $2\sigma_{mPD}$ are transferred to the next level. The complete procedure aims to provide a segmentation that represents sufficiently distinct objects independent of their particular scale.

Figure 3.10(c) shows the segmentation result of the multi-scale optimization on the post-event imagery (figure 3.7(b)). Compared to the original FNEA with only one segmentation scale (figure 3.10(a,b)), image segmentation using multi-scale optimization (figure 3.10(c)), although still facing some difficulties to delineate every individual landslide, decreases the degree of over- and under-segmentation and is able to capture better landslides as image objects among a

number of different scales. Furthermore, the optimization runs fully automatically and liberates the user from a time-consuming trial and error evaluation of the optimal parameterizations for the image segmentation.

3.6 Classification of landslide objects

Landslide classification in previous studies has become increasingly complex. While initial works were largely restricted to digital number (DN) values of multi-spectral bands, later indices such as Normalized Difference Vegetation Index (NDVI), different texture measures, DEM derivatives, and externally prepared vector layers (e.g. of flow accumulation and stream networks) or shadow masks were employed [Martha et al., 2010]. The landslide detection approach presented here makes use of additional spectral and textural measurements: change detection using temporal Principal Component Analysis (PCA), image matching through Spectral Angle Mapper (SAM), anomaly detection by Reed-Xiaoli detector (RXD), and textural analysis with grey level co-occurrence matrix (GLCM). The derivatives of PCA, SAM and RXD are calculated as separate layers and incorporated in OOA as features of each object that were derived during the hierarchical segmentation.

Both the QuickBird imageries were orthorectified by calculating a rational polynomial coefficients (RPC) model as described in Grodecki and Dial [2003], with the elevation information from 1m LiDAR DTM whose resolution is finer than multi-spectral bands of QuickBird, thus allowing an enhancement of the accuracy of RPC orthorectification process. A further image co-registration was performed using polynomial cubic convolution interpolation [Richards, 1999], by

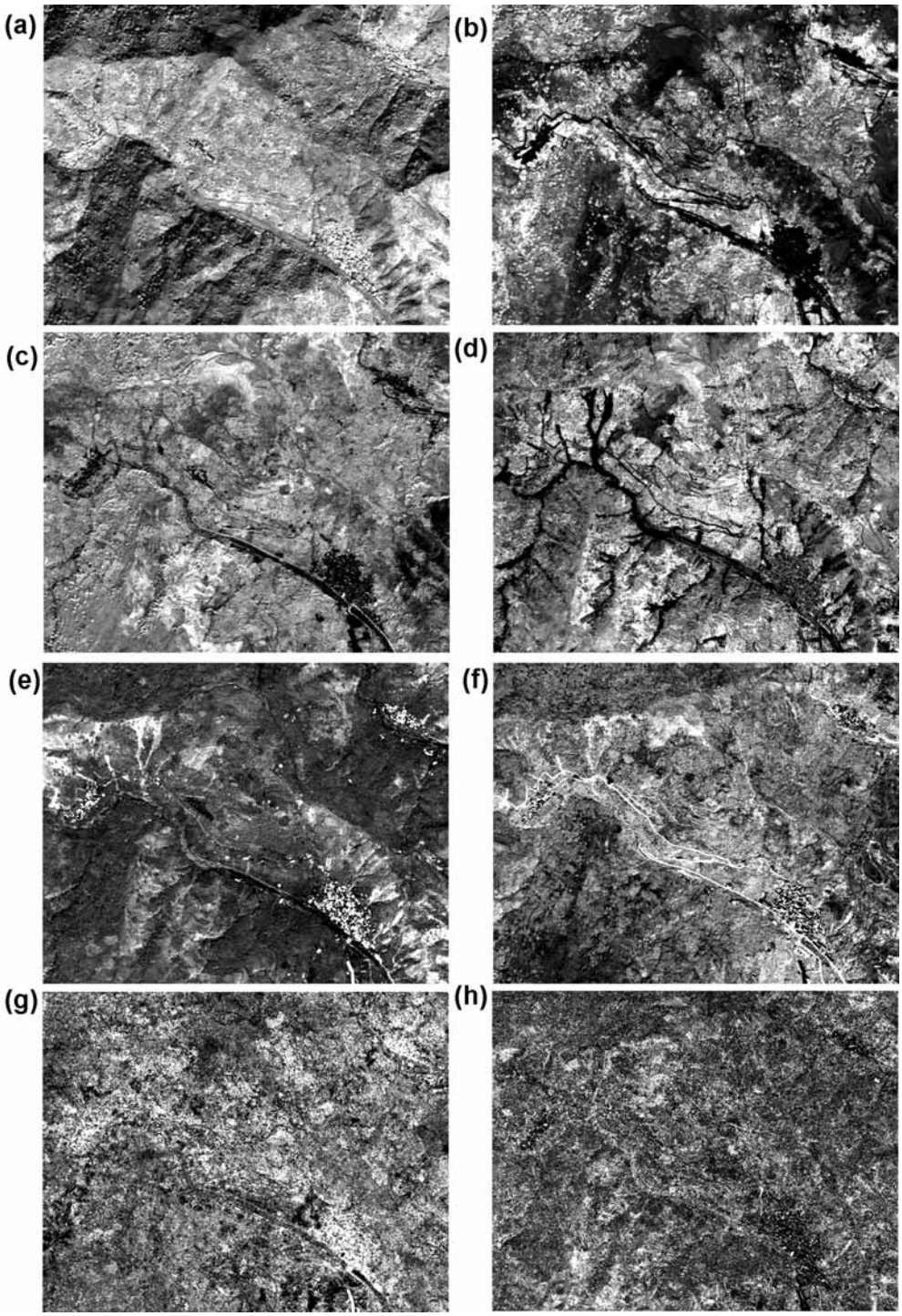

Figure 3.11: An overview of the PCA transformation result from pre- and post-event QuickBird images: (a)–(h) the 1st to 8th components derived from PCA.

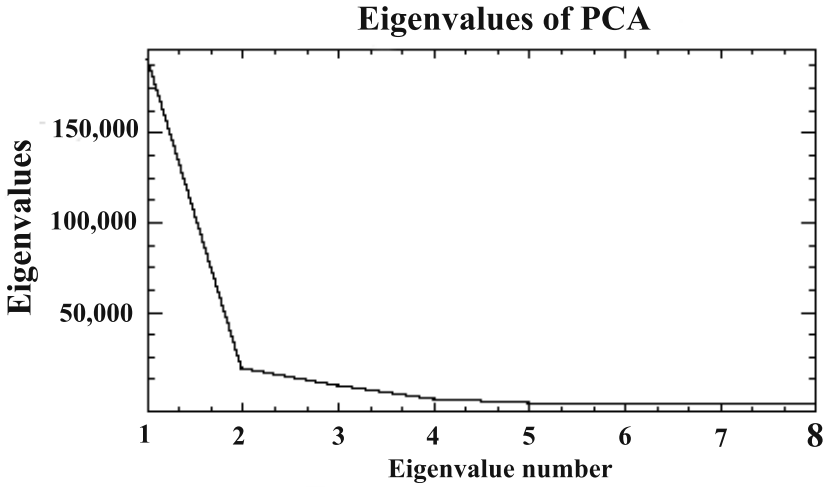

Figure 3.12: The eigenvalues of PCA for 8 bands from pre- and post-event QuickBird imageries

automatically selecting 60 tie points within the ENVI 4.7 software environment, with a RMS error of 0.45.

The change detection was first carried out using temporal PCA (figure 3.11), an image transformation of stacked pre- and post-event images based on eigenvector analysis of their image covariance matrix (figure 3.12), so as to extract principal components meanwhile segregate noise components [Deng et al., 2008; Richards and Jia, 2006; Singh, 1989]. Temporal PCA works by creating new orthogonal axes which rotate the original data by a maximized data variance. In this case, it combined all 8 bands of the pre- and post-event QuickBird images (namely 4 bands each), and transformed these bands into uncorrelated 8 components using:

$$Y_i = e_i^T(X_i - \mu_i) \tag{3.8}$$

where μ is the mean value of all pixel values in band i, e_i is the eigenvector of the data covariance matrix C defined as:

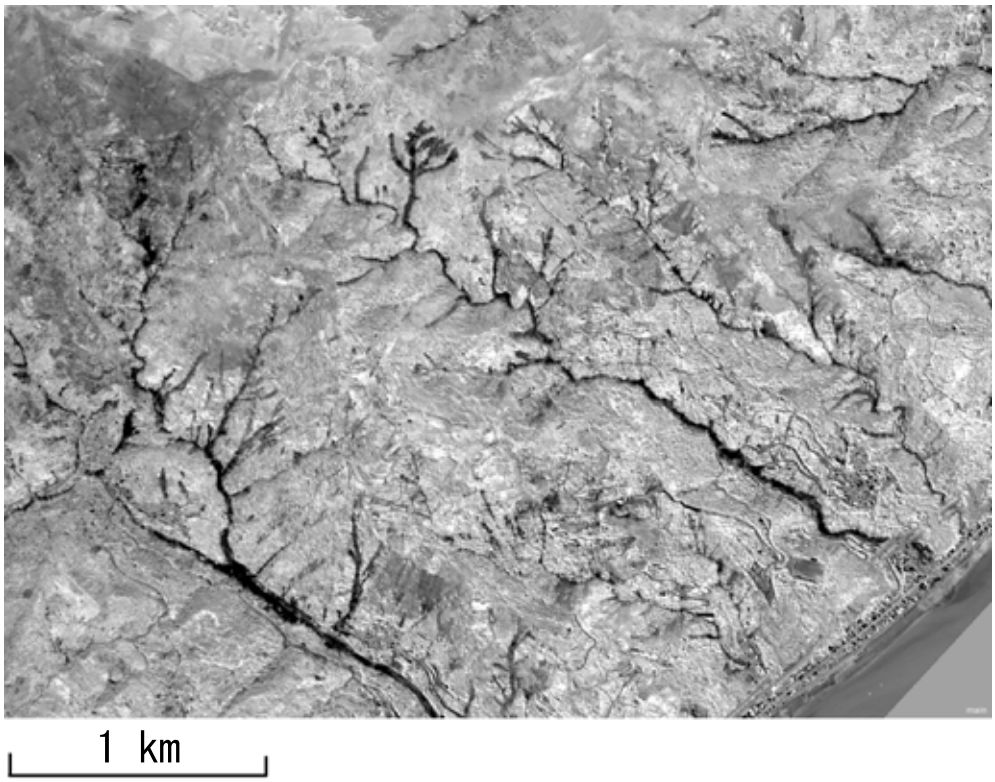

Figure 3.13: The fourth principal component derived from PCA of 8 pre- and post-event QuickBird bands

$$C = \frac{1}{N}\sum_{i}(X_i - \mu_i)(X_i - \mu_i)^T \tag{3.9}$$

N is the number of pixels of band i.

Two transformed image components, the fourth (figure 3.13) and the second (figure 3.14) principal components (respectively referred as PC4 and PC2), were incorporated as separate layers in the Definiens eCognition procedure. As was mentioned by Deng et al. [2008] most changes detected by temporal PCA are contained in the first four components, and in this case these changes of newly-triggered landslides are primarily recognized in PC4. The minor components

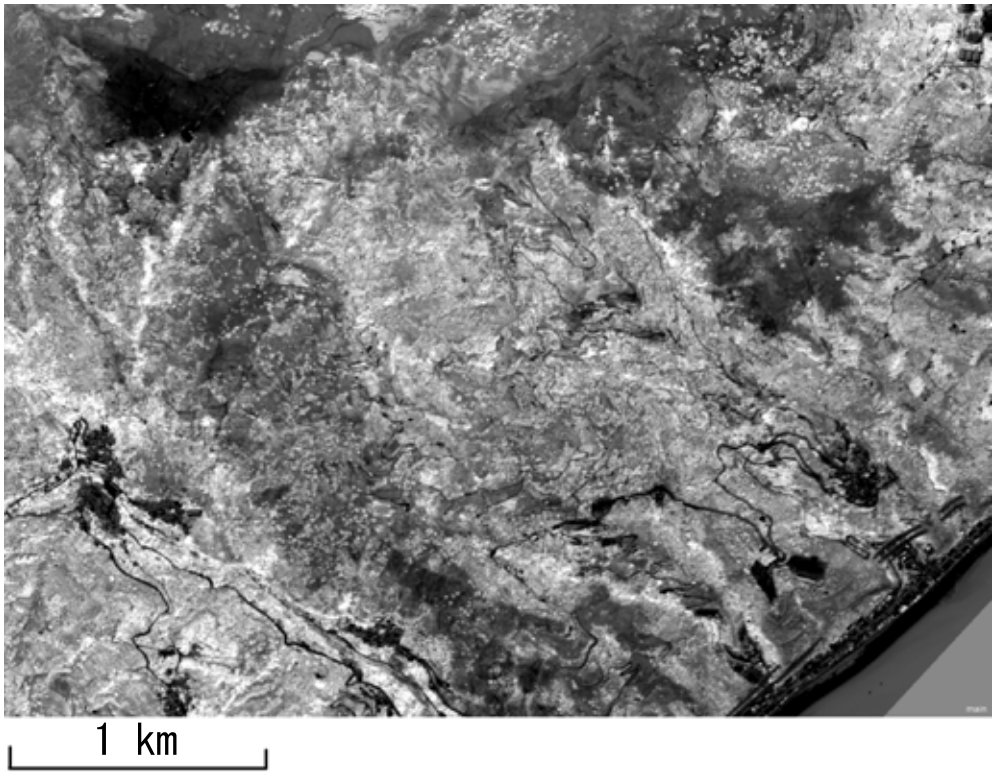

Figure 3.14: The second principal component derived from PCA of 8 pre- and post-event QuickBird bands

beyond PC4 are mainly composed of residuals of the transformation, in most cases as noises due to less variance. In the training area, landslide candidates were preliminarily chosen from PC4 using a membership function calculated from 10 selected samples of landslide objects (Figure 3.15). This membership function is then incorporated in the algorithm of classification and later employed without modification in the testing area. PC2 was also found useful for removing false positives of roads, infrastructures, deforestation areas and the water, most of which are contained in objects with low values of PC2, with a defined threshold of PC2 $<$ -300.

Since shadows were also recorded as changes in PCA, a spectral matching

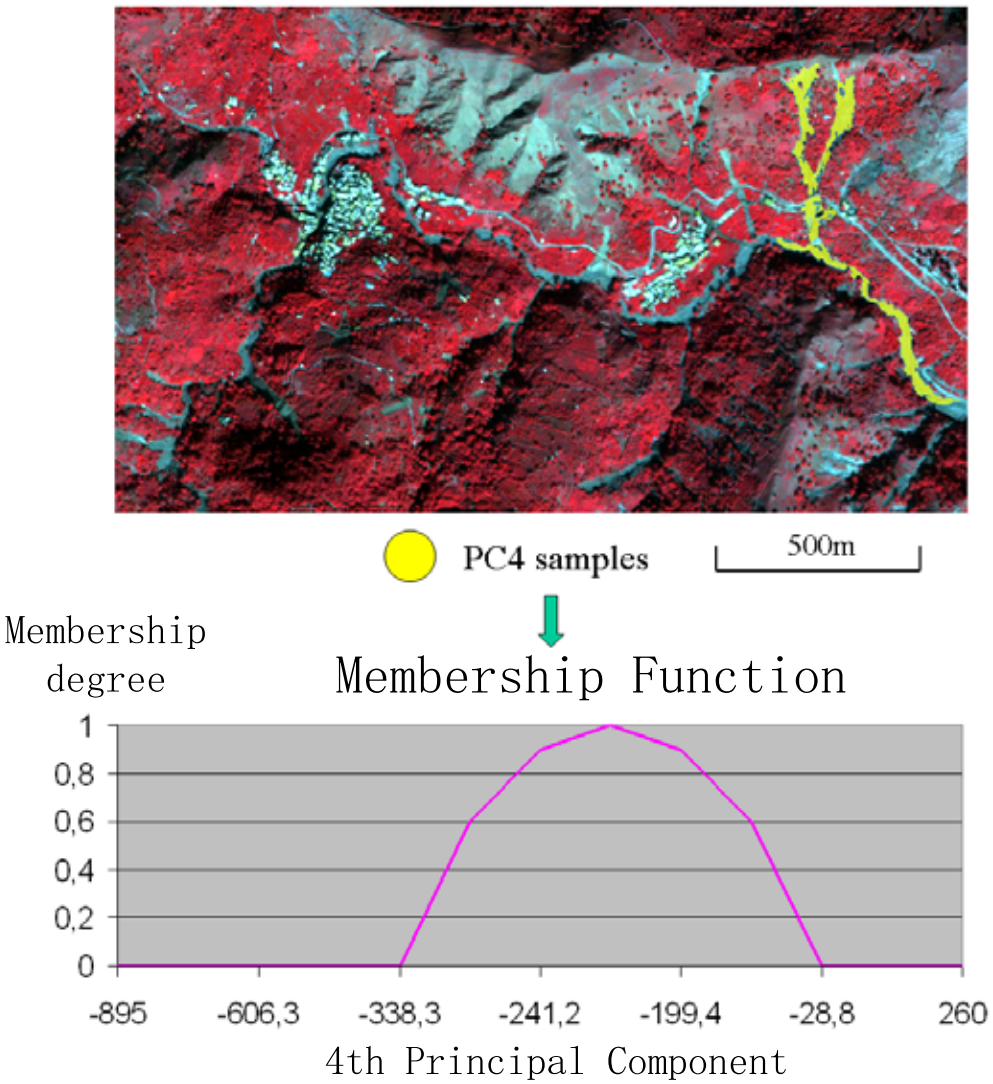

Figure 3.15: The training area of Altolia: (top) The 10 selected samples (yellow), (bottom) the generated membership function from these 10 samples

image (figure 3.16) between the pre- and post-event images was created using SAM [Dennison et al., 2004; Kruse et al., 1993; Sohn and Rebello, 2002] and then imported in OOA. The purpose of SAM is to remove the influence of these subtle spectral changes due to illumination differences and viewing angle variation. The matching image derived from SAM estimates spectral similarity by comparing

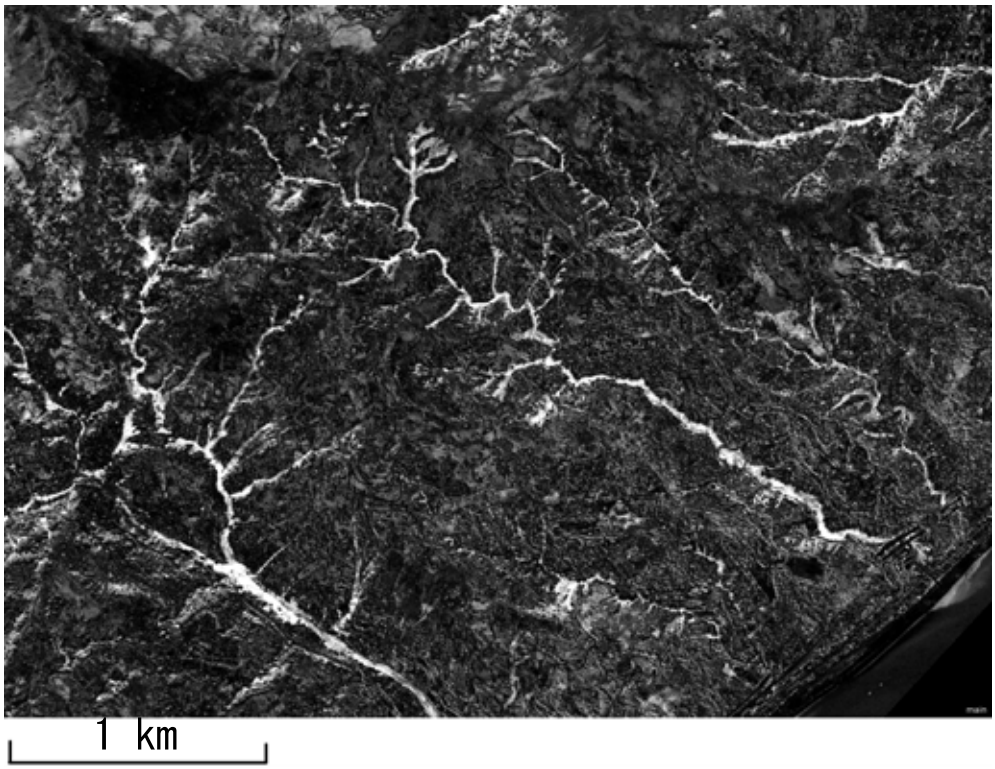

Figure 3.16: The matching image generated from spectral angle mapper using two pre- and post-event QuickBird images

spectral angle difference in terms of image space between the pre- and post-event QuickBird images. For both images each pixel is represented by a spectrum identified as a 4-dimensional vector with specified length and direction. The spectral angle θ was therefore calculated as:

$$\theta = \cos^{-1}\left[\frac{\sum_{i=1}^{4} a_i b_i}{\left(\sum_{i=1}^{4} {a_i}^2\right)^{\frac{1}{2}} \left(\sum_{i=1}^{4} {b_i}^2\right)^{\frac{1}{2}}}\right]. \tag{3.10}$$

while a_i and b_i are respectively the spectra of the pre- and post-event images. As SAM only considers the angle between the spectral vectors but not the vector

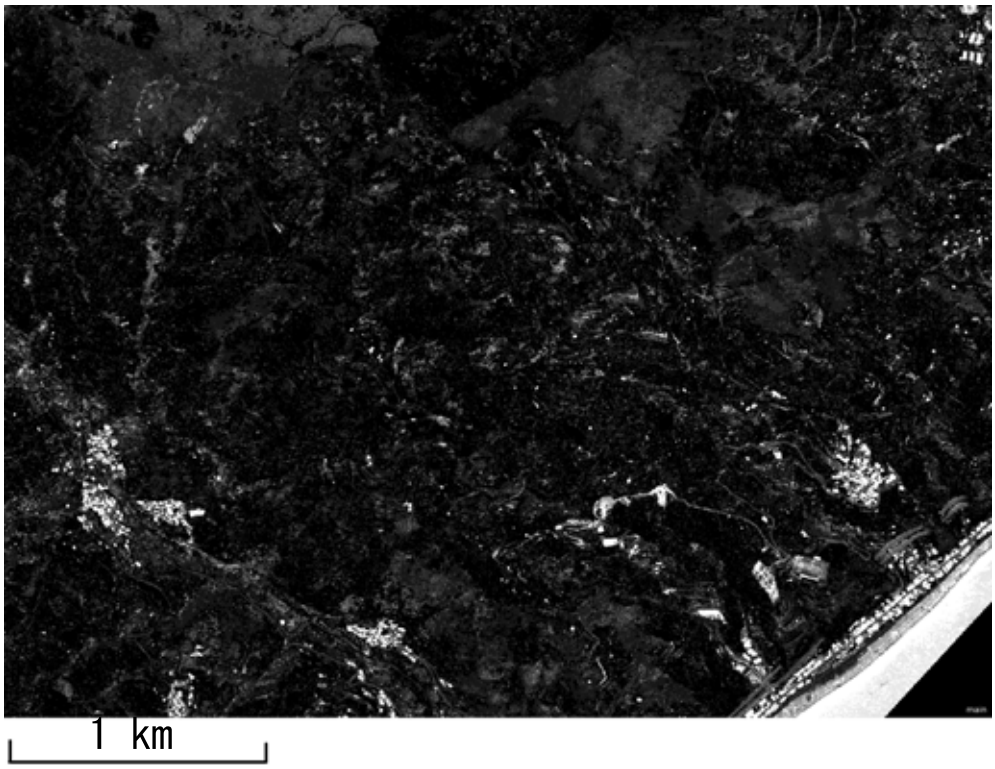

Figure 3.17: The result image of RXD anomaly detection performed on pre-event QuickBird images

length, it is less sensitive to changes due to illumination and shadowing [Kruse et al., 1993]. Excluding objects with low SAM values (SAM < 0.09) allows a removal of spectral false positives that result from subtle spectral changes in illumination as well as shadow, which are not always excluded from the change component of PCA.

In addition, in order to remove false positives such as urban areas as well as existing outcrops and clear-cuts, the RXD anomaly detector [Chang and Chiang, 2002; Reed and Yu, 1990] was used to estimate spectral anomalies based on the pre-event image, allowing the statistical removal of spectral noises. Assuming that urban areas, deforestation, roads and other infrastructure demonstrate

spectral signatures significantly different from the background, RXD can be used to highlight those areas. In this study RXD is applied on the pre-event imagery to detect spectral anomalies that existed already before the event, which are consequently excluded as newly-triggered landslides. The anomaly detector

$$\delta_{RXD}(r) = (r - \mu)^T K^{-1} (r - \mu) \tag{3.11}$$

was used in RXD, where r is 4x1 vector for 4-band pre-event QuickBird image, μ is 4x1 global mean vector, and K is 4x4 sample covariance matrix. A created anomaly image (figure 3.17) was then derived and employed as an additional layer in Definiens eCognition. Objects with large RXD values were considered as spectral anomalies and a threshold of $\delta_{RXD}(r) > 16$ was defined to exclude these anomalous false positives.

Following the spectral processing that identified landslide candidate objects, a texture analysis of a 1m LiDAR DTM was performed after merging those candidates. Limited attempts have been made to use texture analysis of airborne and satellite imagery for the identification of landslides (e.g. Mason et al. [1998]; Whitworth et al. [2005]). These studies applied texture measures to quantify image roughness and thereby highlight hummocky landform with turbulent texture. The texture analysis here was performed on elevation data for the purpose of analyzing topographic variability, using second-order statistics of the widely-applied GLCM [Haralick et al., 1973]. The objective is to remove false positives with low-frequency elevation variation, such as undisturbed or unfractured areas, homogenous flat surfaces, and objects with low height variation (e.g. roads and water bodies). Haralick et al. [1973] have introduced 14 texture features calcu-

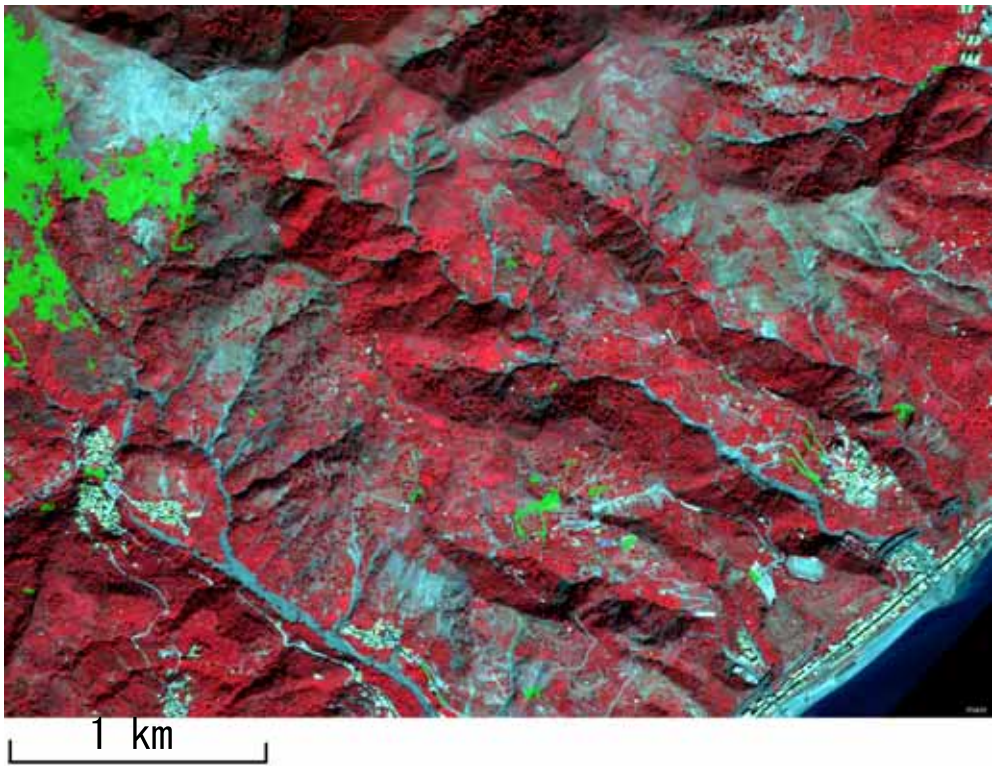

Figure 3.18: The false positives mapped by texture analysis of grey level co-occurrence matrix (GLCM) mean (in green)

lated from GLCM. In our study, since no local contrast and variation inside each object is focused, only the GLCM mean m is used, determined by:

$$m = \sum_{i,j=0}^{N-1} i(P_{i,j}) \times 100 \tag{3.12}$$

where i and j are respectively the row and column of GLCM of DEM, $P_{i,j}$ is the normalized value of cell (i,j) in GLCM of DEM. Texture features calculated from GLCM mean were used in our study. Neighboring pixels in all directions (0°, 45°, 90°, 135°) were considered for the GLCM generation, accounting for the potential different aspects of landslide objects. Objects with low GLCM mean

values were considered to be false positives, and a threshold of GLCM mean < 126.7 was defined (figure 3.18). The remaining landslide candidates were then classified as final output of newly-triggered landslides.

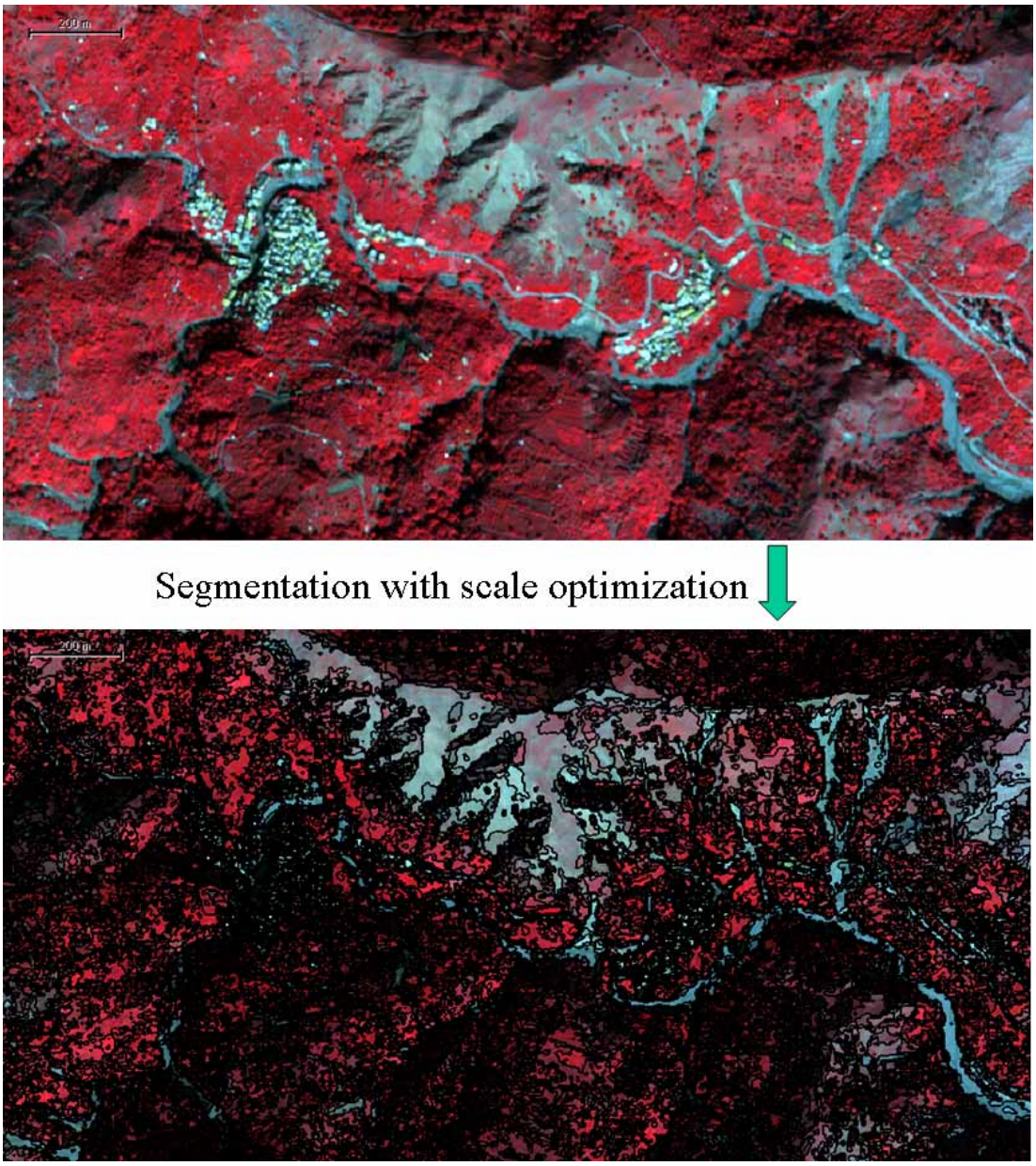

Figure 3.19: The segmentation using scale optimization in the training area of Itala.

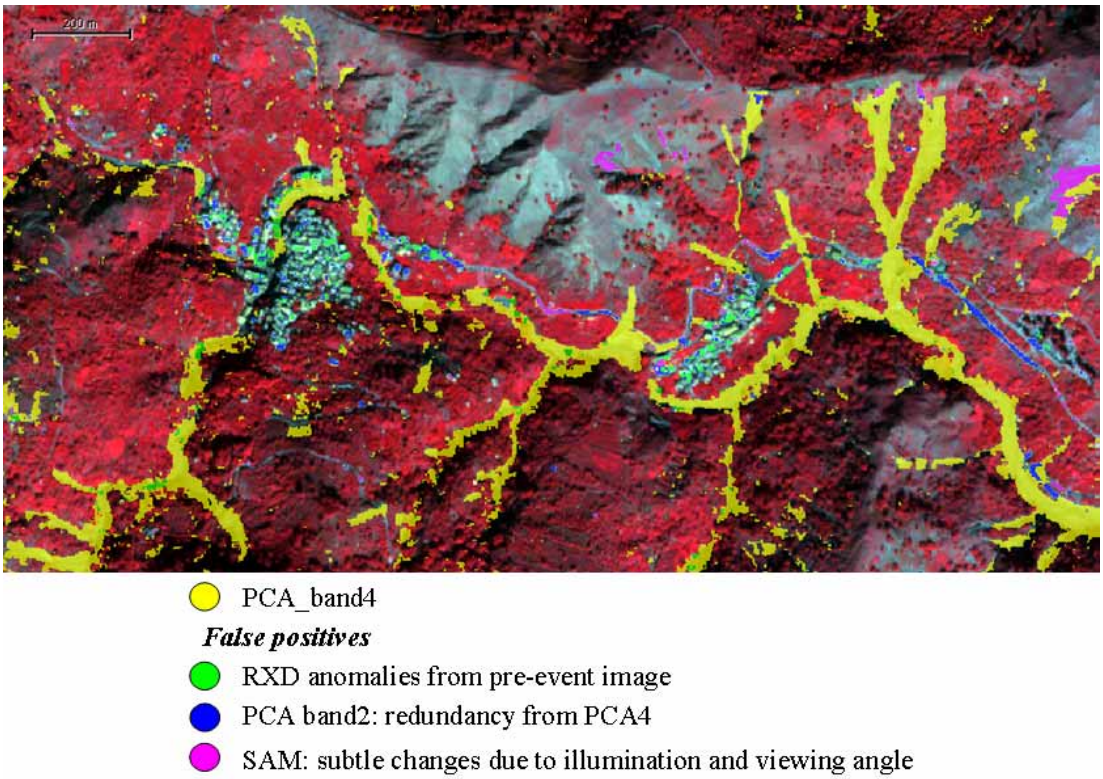

Figure 3.20: The classification result from OOA spectral analysis in the training area of Itala.

3.7 Result and accuracy assessment

The algorithm developed based on the training area of Altolia was directly applied in the testing area of Itala, without any changes in membership function values and previous defined thresholds in the ruleset. The segmentation result of the training area is shown in figure 3.19. The classification result of landslide candidate objects and false positives from spectral analysis in the training area is displayed in figure 3.20. The outcome of a further textural analysis outcome is demonstrated in figure 3.21. The final outputs for the testing area are shown in figure 3.22. To evaluate the accuracy of this approach, OOA-derived land-

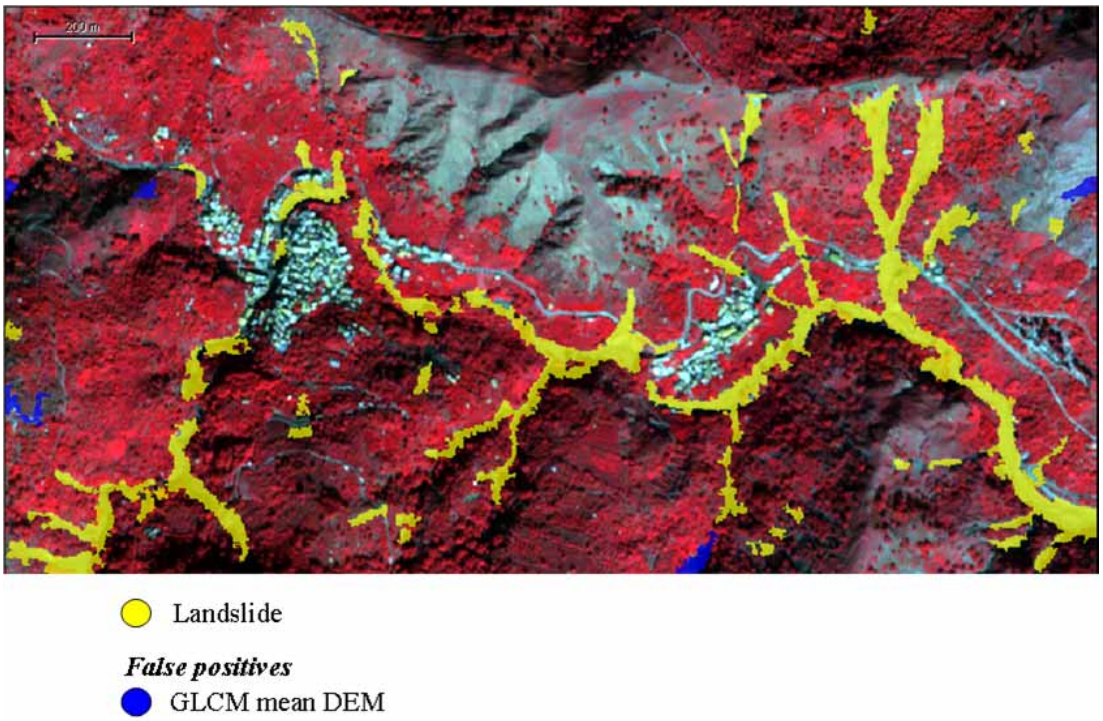

Figure 3.21: The classification result from OOA textural analysis in the training area of Itala.

slides were compared with a manually-mapped landslide inventory. The accuracy assessment was carried out for the number and the spatial extent of mapped landslides (table 3.1), both of which are considered critical in a subsequent quantitative landslide hazard assessment and prospective risk analysis. The number of landslides is useful for a quantitative estimate of the temporal probability of landslide occurrence, whereas the spatial extent of landslide is beneficial for the estimate of probability of landslide size through the landslide frequency-area statistics [Guzzetti et al., 2005a; van Westen et al., 2006].

The accuracy assessment calculates the commission and omission errors, which are measures of the user's and producer's accuracies [Congalton, 1991; Story and

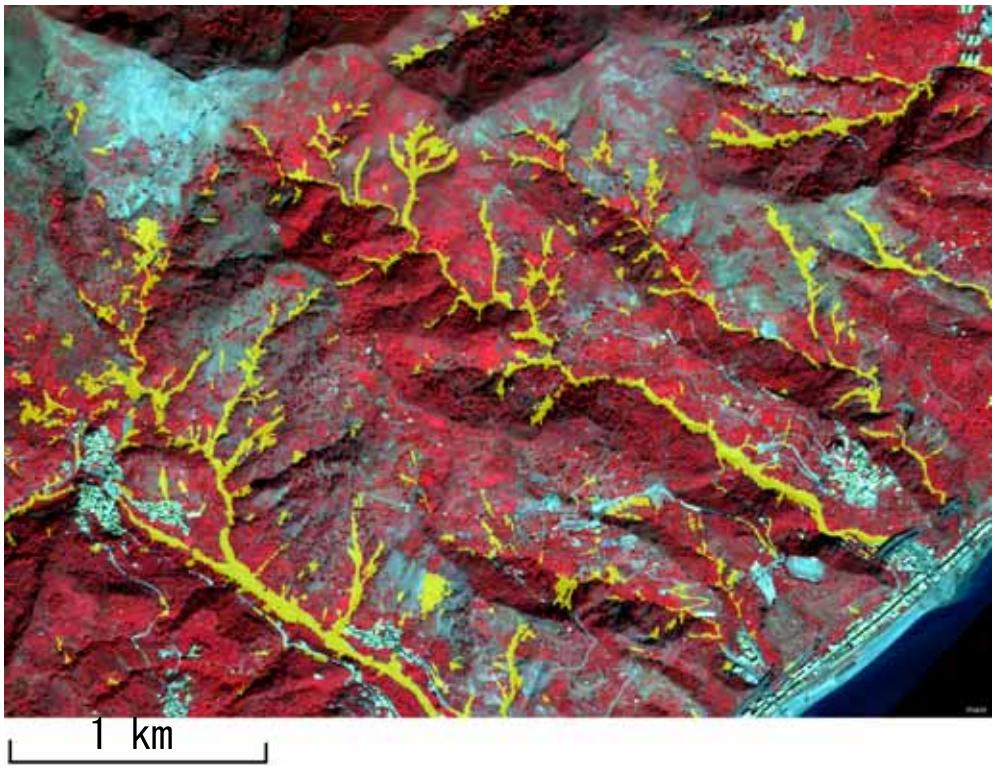

Figure 3.22: The result of OOA landslide mapping in the independent testing area of Itala

Congalton, 1986] of the mapped landslides, respectively. For the spatial extent of landslides a user's accuracy of 75.9% and a producer's accuracy of 69.9% were achieved. In terms of the number of landslides, user's and producer's accuracies of 81.8% and 69.5%, respectively, were reached. For both number and spatial extent of landslides the results show a lower producer's accuracy than user's accuracy: specifically, ca. 31% of all manually mapped landslides were omitted in the OOA-based detection. This indicates an overestimation of false positives during their classification, accompanied with an underestimation of true positives obtained from the membership function of the selected samples. Further improvements should include a more accurate definition of these thresholds for classifying false

Table 3.1: Accuracy assessment for OOA mapped landslides.

	Manual	OOA	TP [1]	UA [2]	PA [3]
Number	285	242	198	81.8%	69.5%
Extent (km^2)	0.602	0.555	0.421	75.9%	69.9%

[1] TP: true positives
[2] UA: user's accuracy
[3] PA: producer's accuracy

positives and a more careful selection of representative samples.

3.8 Conclusion

This chapter describes a novel approach of object-oriented change detection for rapid mapping of newly-triggered landslides after major events, using VHR satellite images and LiDAR data. The approach used semi-automatic mapping with a minimum user involvement and benefited from systemized OOA work processes. First, a problem-specific multi-scale optimization of FNEA was proposed to reduce the degree of over- and under-segmentation of landslides among a number of different scales, avoiding a time-consuming trial and error evaluation of the optimal segmentation parameters that has characterized most OOA research in the past. Second, change detection using image transformation of PCA was not only found to be useful for a preliminary selection of landslide candidates from PC4, but also enabled a removal of false positives directly from PC2. Third, the matching image derived from SAM allowed the detection of subtle spectral changes from the change of spectrum vector direction. Fourth, spectral anomalies detected by RXD in the pre-event image allowed the removal of false positives, such as landslides that already existed before the landslide event of October 2009.

Finally, surface texture measures based on a 1m LiDAR DTM were incorporated to remove false positives with low-frequency elevation variation.

For the case study in Messina, the approach achieved user's and producer's accuracies of 75.9% and 69.9%, respectively, for the extent of landslides, and 81.8% and 69.5%, respectively, for the number of landslides. Although the accuracy of the automatic approach does not entirely match what can be achieved in manual mapping, it provides an efficient supplement for traditional methods. The chosen spectral object features are expected to be useful to accommodate multi-spectral information from a great variety of different sensors. The proposed thresholds typically need further adjustment for the application in other cases, whereas in the presented example the visual inspection of one fifth of the study area was sufficient for this purpose. Also, it should not be forgotten that considerable time can be saved for landslide mapping because the manual drawing of landslides boundaries is replaced by image segmentation. Hence, for an effective landslide hazard assessment, the approach provides an efficient tool to retrieve lacking temporal data for an event-based landslide inventory, thus allowing the assessment of temporal probability and magnitude of landslide events for a quantitative hazard assessment.

Chapter 4

PSI hotspot and clustering analysis for detection of slow-moving landslides

As mentioned in Chapter 2, the InSAR technique has already gained its importance in landslide mapping and monitoring applications, due to its strength in mapping topography and estimating surface deformation [Massonnet and Feigl, 1998]. However, the usefulness of conventional differential InSAR applications is often limited by disturbing factors such as temporal decorrelation and atmospheric disturbances. The Persistent Scatterers Interferometry (PSI) technique is a recently developed InSAR approach. It generates stable radar benchmarks (namely persistent scatterers, PSI point targets) using a multi-interferogram analysis of SAR images. The PSI technique has the advantage of reducing temporal decorrelation and atmospheric artefact. It is suitable for the investigation of extremely slow-moving landslides for its capability to detect ground displacements

with millimeter precision. However, the interpretation of PSI outputs is sometimes difficult for the large number of possible persistent scatterers (PS).

In this chapter, a new approach of PSI Hotspot and Cluster Analysis (PSI-HCA) is here introduced in order to develop a procedure for mapping landslides efficiently and automatically. This analysis has been performed on PS in hilly and mountainous areas within the Arno river basin (Italy). The aim is to use PS processed from 4 years (2003-2006) of RADARSAT images for identifying areas preferentially affected by extremely slow-moving landslides. The Getis-Ord G_i^* statistic was applied in the study for the PSI-HCA approach. The velocity of PS was used as weighting factor and the G_i^* index was calculated for each single point target. The results indicate that both high positive and low negative G_i^* values imply the clustering of potential mass movements. High positive values suggest the moving direction towards the sensor along the satellite Line-of-Sight (LOS) whereas low negative values imply the movement away from the sensor. Furthermore, the kernel function was used to estimate PS density based on these derived G_i^* values. The output is a hotspot map which highlights active mass movements. This spatial statistic approach of PSI-HCA is considered as an effective way to extract useful information from PS at a regional scale, thus providing an innovative approach for rapid mapping of extremely slow-moving landslides over large areas.

4.1 Persistent Scatterer Interferometry

4.1.1 Introduction to the technique

SAR interferometry (InSAR), as a major branch of remote sensing, plays an important role in landslide mapping and monitoring applications, thanks to its utility in detecting ground movements with millimeter precision [Corsini et al., 2006; P.Canuti et al., 2007; Rott and Nagle, 2006; Squarzoni et al., 2003]. Also, these applications are benefited from the advantages of InSAR which is independent of weather conditions and is regardless of day and night. Besides, the side-looking imaging radar ensures an improvement of pixel resolution in the viewing direction. In addition, for satellite-based radar, it has the advantages of global access, large swath (area seen on the ground), regular repeated image acquisition, huge data archive and low cost [Santoro, 2008]. A general sketch of InSAR can be found in figure 4.1.

However, the conventional InSAR processing technique for ground movement detection, which is primarily focused on the differential InSAR (DInSAR) technique [Massonnet and Feigl, 1998; Rosen et al., 2000] and based on the assumption that surface deformation change is linear, is often affected by the temporal decorrelation and atmospheric disturbances [Colesanti and Wasowski, 2006; Ferretti et al., 2001; Kimura and Yamaguchi, 2000; Massonnet and Feigl, 1998]. These disturbing factors, which produce a bias during the phase measurement and the difficulty in fulfilling a baseline criteria, bring the need for further advanced processing approaches of SAR images.

One possible solution is the utilization of multi-temporal SAR images for a long-term interferogram processing, such as the technique of Persistent Scatter-

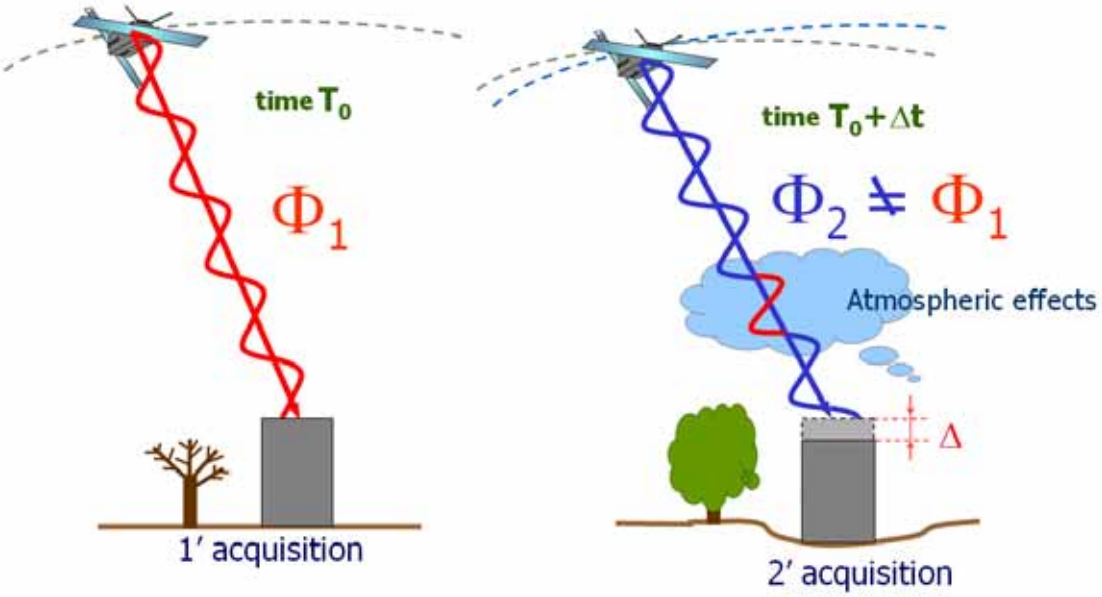

Figure 4.1: A general sketch of the concept of InSAR. ϕ refers to the interferogram phase.

ers Interferometry (PSI) which was developed over recent years. The general flowchart of PSI can be found in figure 4.2. Several approaches using different statistical approaches have been developed for this technique in order to extract long-term stable benchmarks as PSI point targets, namely persistent scatterers (PS), from some multi-interferogram analysis of SAR data. For example, the $PSInSAR^{TM}$ technique was proposed by Ferretti et al. [2000, 2001] and improved by Colesanti et al. [2003]. Besides, Hooper et al. [2004] presented a method to develop a time series of deformation by using the spatially correlated nature of ground deformation. Its measuring accuracy was further improved by Hooper et al. [2007] whose approach is the Stanford Method for Persistent Scatterers (StaMPS). Meanwhile, a small baseline approach known as the Coherent Pixels Technique (CPT) was suggested by Mora et al. [2003] and Blanco-Sanchez et al.

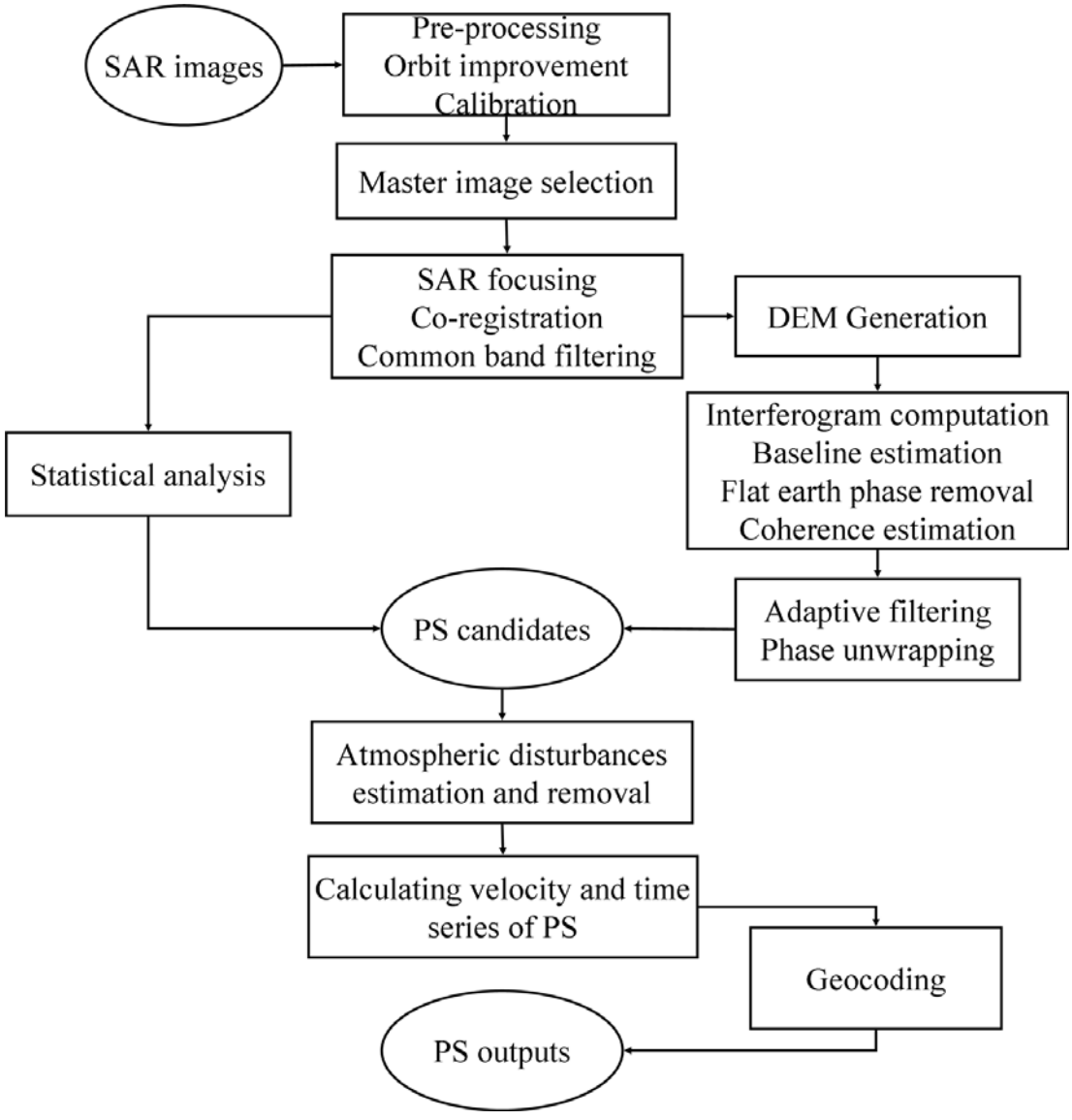

Figure 4.2: The general flowchart of Persistent Scatterer Interferometry processing. Different statistical approaches are summarized in table 4.1

[2008]. Moreover, an Interferometric Point Target Analysis (IPTA) was presented by Werner et al. [2003] and Strozzi et al. [2006]. This approach has the advantages of finding persistent benchmarks in low-coherence regions and allows the use of large baselines for phase interpretation. Other recently-developed long-term InSAR techniques include Small Baseline Subset (SBAS, Berardino et al. [2002]; Casu et al. [2006]; Lanari et al. [2004]) and Stable Point Network (SPN, Crosetto et al. [2008]; Duro et al. [2003]). A summary of these PSI techniques can be found in table 4.1. Some successful cases have shown the suitability of PSI for detecting, investigating and monitoring landslides [Bovenga et al., 2005; Colesanti and Wasowski, 2006; Colesanti et al., 2003; Farina et al., 2003, 2006; Ferretti et al., 2005; Hilley et al., 2004].

4.1.2 $PSInSAR^{TM}$ technique and available dataset

The PSI point targets available in this study were processed by Tele-Rilevamento Europa (TRE) on behalf of the Arno River Basin Authority. The processing procedure employs the $PSInSAR^{TM}$ technique, a long-term multi-image interferometric approach proposed by Ferretti et al. [2000, 2001]. This approach is able to overcome major disadvantages of DInSAR (e.g. temporal decorrelation and atmospheric disturbances). Long temporal series enables the decoupling of height and deformation. Meanwhile, atmospheric artifacts can be estimated and moved out. Interferometric phase was analyzed on a pixel-by-pixel approach. Stable radar benchmarks, namely PS, can be identified using a coherence map. PS are usually recognized as man-made structures (e.g. buildings, dams and bridges) as well as natural reflectors (e.g. bared rocks). The velocity of each single PSI

Table 4.1: A summary of current major Persistent Scatterers Interferometry techniques

Technique	Developer	Description	References
$PSInSAR^{TM}$	TRE (Italy)	Expected phase stability of scattering barycenter of sampling cell; low differential atmospheric phase contributions; interferogram regardless of normal and temporal baseline	Colesanti and Wasowski [2006]; Colesanti et al. [2003]; Ferretti et al. [2000, 2001]
StaMPS	Stanford University (USA)	A time series of deformation using the spatially correlated nature of ground deformation for pixels with low phase variance	Hooper et al. [2004, 2007]
CPT	UPC (Spain)	Separation between amplitude and coherence-based approach for pixel selection criteria; obtain the non-linear deformation component	Blanco-Sanchez et al. [2008]; Mora et al. [2003]
IPTA	GAMMA Remote Sensing (Switzerland)	Finding persistent benchmarks in low-coherence regions and allows the use of large baselines for phase interpretation	Strozzi et al. [2006]; Werner et al. [2003]
SBAS	CNR (Italy)	Performing only on small-baseline interferograms; employing Singular Value Decomposition (SVD) method	Berardino et al. [2002]; Casu et al. [2006]; Lanari et al. [2004]
SPN	Altamira (Spain)	Estimate both the linear and non-linear components of deformation; Adaptive filters in space and time domains; Combine temporal and spatial filters	Crosetto et al. [2008]; Duro et al. [2003]

Table 4.2: Some parameters of RADARSAT

Agency	CSA
Band	C
Wavelength	5.6 cm
Polarization	HH
Beam mode	S3
Incidence angle	37°
Resolution range	30 m
Resolution azimuth	30 m
Scene width	100 km
Passage rate	24 days

point target can be estimated by performing a statistical analysis on amplitudes of electro-magnetic returns. The detailed description of $PSInSAR^{TM}$ technique can be found in Colesanti and Wasowski [2006]; Colesanti et al. [2003]; Ferretti et al. [2000, 2001, 2005].

A PS dataset derived from 4 years of RADARSAT (see detailed parameters in table 4.2) images spanning from March 2003 to January 2007 is available for the Arno river basin. As indicated in table 4.3, a total of 102 images (54 ascending and 48 descending scenes) were used to conduct $PSInSAR^{TM}$ analysis, with an acquisition cycle of 24 days. These images were captured by a beam mode of S3 that renders an incidence angle ranging between 30° and 37°. The used satellite track is 54 for descending and 247 for ascending acquisition. These two tracks cover about 6300 km^2, ca. 70% of the whole basin area.

The selection of a master image is important for the processing. The principle is to choose an image able to minimize the high dispersion of the baseline values and the geometry distortion of slave images [Brugioni, 2007]. The master image should be selected on a day without intensive precipitation to also avoid the atmospheric disturbance and not to compromise the quality of differential in-

Table 4.3: RADARSAT data used for the processing of $PSInSAR^{TM}$

RADARSAT - ascending orbit				
Track	Beam mode	No. of scenes	Temporal coverage	master image
247	S3	54	April 2003 – January 2007	27 March 2005
RADARSAT - descending orbit				
Track	Beam mode	No. of scenes	Temporal coverage	master image
54	S3	48	March 2003 – January 2007	14 November 2004

terferogram. The final chosen master images are listed in table 4.3. The focusing and co-registration were performed on the sampling grid of the master acquisition with the lowest dispersion of the normal baseline values.

Each pixel of SAR image is associated with the information of amplitude and phase. As illustrated in Ferretti et al. [2005], the phase information is composed of:

$$\phi = \psi + \frac{4\pi}{\lambda} r + \alpha + \varepsilon \tag{4.1}$$

where ϕ is the interferogram phase, ψ is the reflectivity of an object, r is the distance from the satellite to target, λ is the signal wavelength, and α is the atmospheric phase contribution. The noises (ε) are composed of decorrelation noise and the residual topographic phase contribution resulting from errors in the reference DEM. In two radar images, the phase shift can be described as:

$$\Delta\phi = \Delta\psi + \frac{4\pi}{\lambda} \Delta r + \Delta\alpha + \varepsilon \tag{4.2}$$

if the reflectivity phase contribution ψ remains unchanged for both scenes ($\Delta\phi = 0$), and if atmospheric disturbances and noise can be removed, the phase shift can be written as:

$$\Delta\phi = \frac{4\pi}{\lambda}\Delta r \tag{4.3}$$

and the possible target motion (Δr) can be estimated from phase shift $\Delta\phi$.

According to this basic model of signal phase definition, a time series analysis of phase values for each RADARSAT pixel (beam mode S3, 20m East-West, 5m North-South) was performed. Multiple differential interferograms were generated between each pair of two successive acquisitions, and the phase of master image was compared with all slave images. Totally 53 ascending and 47 descending differential interferograms were generated. These interferograms get the information of both ground motion of the target, topographic phase contribution and atmospheric disturbances. The following step was to individualize the sub-pixel persistent scatterers independently from the sensor position (geometric baseline) and the moment of acquisition (temporal baseline), by estimating and isolating different interferometric phase contributions, using a numerical and statistical analysis as indicated in Colesanti and Wasowski [2006]; Colesanti et al. [2003]; Ferretti et al. [2000, 2001, 2005].

The PSI point target can then be identified by the coherence maps linked to the exploited interferograms. Approximately 700,000 PS were obtained, with a coherence higher than 0.60. The precision of displacement rates ranges from 0.1 to 2 mm/year along LOS, depending on coherence and distance to the reference point. The geocoding accuracy of PS location is within 10m in East-West and

5m in the North-South direction. The density of ascending data is 54 PS/km^2 while the density of descending point targets is 60 PS/km^2. For the purpose of landslides detection, PS located within the flat area were masked out so that the processing was only performed in mountainous and hilly areas. PS density after masking decreases to 31 PS/km^2 for ascending data and 32 PS/km^2 for descending data.

4.2 Problem definition

The PSI technique has increased its usefulness in different solutions. However, information extraction from PSI technique is sometimes difficult due to a possible large number of PS, thereby entailing long interpretation times. Especially in those regions where there are a lot of stable reflectors such as buildings and bared rocks, the PS density is possibly higher than 500 PS/km^2 [Colesanti and Wasowski, 2006]. A large number of PS also limit the efficiency for detection and mapping of landslide hazards. Especially for a study over large areas, a manual interpretation of PS is nevertheless inefficient and subjective, thereby decreasing the use of PS in landslide rapid detection purposes. Hence, an efficient approach of data processing and analyzing over a large amount of PS is needed.

The need for an efficient processing approach is also reflected in the rapid improvement of sensors and its platforms. For example, PSI point targets are expected to be acquired and updated even more frequently in the near future as a consequence of the rapid development of new satellite platforms with short revisit time [Galeazzi, 2000]. Furthermore, PS density is going to be largely increased with the recent launch of several X-Band satellites (e.g. COSMO-SkyMed and

TerraSAR-X) leading to a significant improvement in the resolution [Bamler et al., 2006]. Therefore, the need for a rapid approach is also needed due to the rapid development of space technology.

Additionally, other efforts of increasing target density have always been performed by improving processing approaches of SAR images, such as the methodology illustrated by Leijen and Hanssen [2007] and the $SqueeSAR^{TM}$ technique mentioned by [Novali et al., 2009]. Especially for the newly developed $SqueeSAR^{TM}$ technique, the point density of PS can be significantly improved in rural areas. This is essential for the PS application in landslide studies. As a result, the demand of efficient PS data interpolation is also resulted from the improvement of SAR image processing techniques.

In sum, an effective approach of data interpretation over large and very-large datasets is generally needed for analyzing PS datasets. This is also for the purpose of a rapid and semi-automatic detection of landslide hazards, which is always within the detection range of PSI techniques.

4.3 Study area

4.3.1 Geographic location

The Arno river basin is situated in central Italy (figure 4.3), 98.4% of the area within the region of Toscana and 1.6% within the region of Umbria. The basin covers completely 5 provinces: Firenze, Prato, Pistoia, Pisa and Arezzo. Also, the basin partly covers the province of Siena, Lucca, Livorno and Perugia.

The total area of the basin is approximately 9130 km^2, with hydrographic

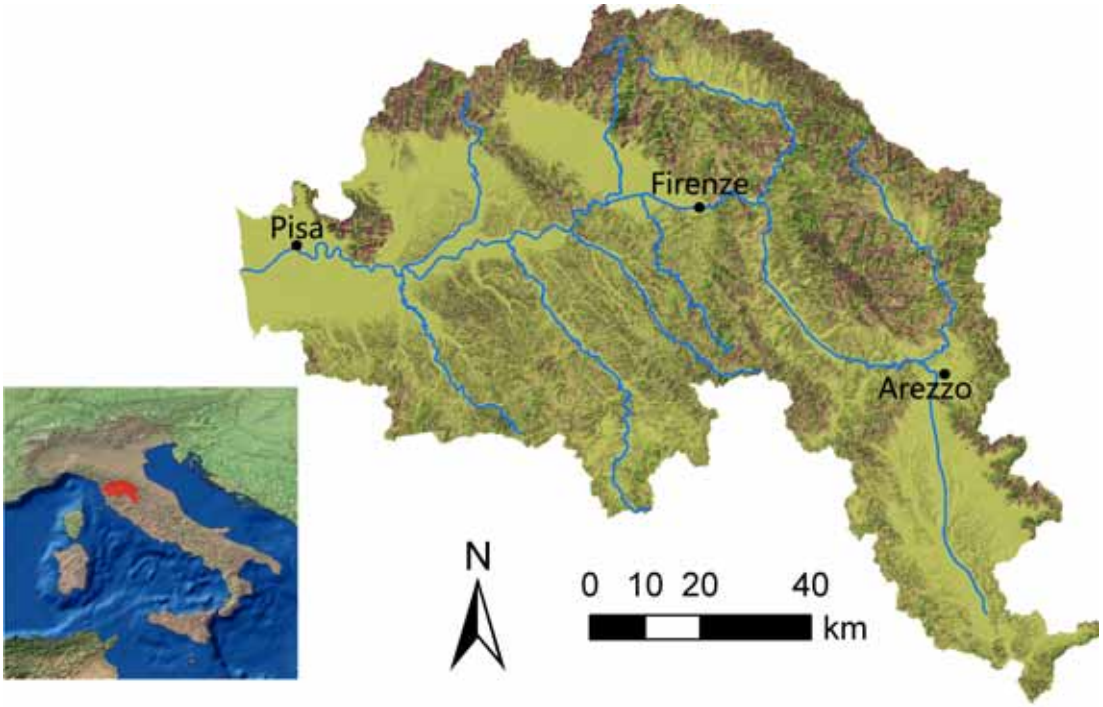

Figure 4.3: The location of the Arno river basin

area of approximately 8200 km^2. The basin is across the Apennines chain and accordingly 78% (ca. 7190 km^2) of the total area is located in mountainous and hilly areas. The mean elevation of the whole basin is about 235m above sea level, with ca. 55% of the basin lower than 300m, ca. 30% between 300m and 600m, ca. 10% between 600m and 900m, and another 5% higher than 900m [Marks, 2006].

The basin includes 2.2 million inhabitants which are distributed within 166 municipalities [Marks, 2006]. The major cities include Arezzo, Pisa and Firenze which is also the capital of Toscana region (see their locations in figure 4.3).

4.3.2 Geological settings

The Arno river basin is situated across the Northern Apennines orogenic belt which is a complex thrust-belt system formed by the juxtaposition of several tectonics units, built during the Tertiary under a compressive regime followed by extensional tectonics from the Upper Tortonian [Catani et al., 2005b].

The latter phase brought several horst and graben structures with an alignment of NW-SW which induced the emplacement of Neogene sedimentary basins that could arise during the Pliocene and Pleistocene [Catani et al., 2005b; Vai and Martini, 2001]. The basin sediments are of marine (west) or fluvio-lacustrine origin (east), depending on the location of the intra-mountainous basins, and resulted from marine transgression and regression cycles (west to east), which occurred during Miocene and Pliocene. Marine transgression and regression cycles occurred during the Miocene and Pliocene while fluvio-lacustrine sedimentation occurred during the Pliocene-Quaternary ages [Boccaletti and Sani, 1998; Marks, 2006; Vai and Martini, 2001].

The drainage system of the Arno river is accordingly influenced by this structure, thus bringing the prevailing NW-SE trending streams. Four main ridges can be identified as follows: (1) Mt. Pisano-Montagnola Senese, made up of clastic and carbonate rocks of Mesozoic and Paleozoic age; (2) Mt. Albano-Chianti, prevalently composed by flysch units emplaced during the Tertiary and the Mesozoic; (3) Calvana-Mt. Morello, Pratomagno, made up of calcareous and arenaceous flysch of respectively the Ligurian and the Tuscan Series and (4) Mt. Falterona-Mandrioli-Alpe di Catenaia, constituted by arenaceous and marly flysch formations of the Ligurian Series. The main basins can be specified

as: (1) Lower Valdarno, prevalence of Pliocene marine deposits; (2) Middle and Upper Valdarno, with Villafranchian and Pleistocene fluvio-lacustrine sediments; (3) Mugello and Casentino sub-basins, featured by Upper Villafranchian fluvio-lacustrine terrains and (4) Chiana Valley, influenced by the Pliocene marine and the Villafranchian lacustrine cycles [Catani et al., 2005b; Marks, 2006].

4.3.3 Landslide hazard within the basin

The Arno river basin is very susceptible to landslide hazard and the total affected area of landslides is about 800 km^2. In the past few years, more than 27,000 landslides were mapped by the Arno River Basin Authority [Catani et al., 2005b] and by the SLAM project of European Space Agency [Farina et al., 2006], using aerial photo-interpretation, field surveys, historical archive data, optical image interpretation and PSI technique. These landslides are dominated by rotational slides (about 74%). The other types of mass movement include solifluction, shallow landslides (18%) and flows (5%). Most of these landslides are slow and intermittent, accompanied with accelerations due to prolonged and/or intense rainfall (Canuti and Focardi 1986). In addition, the occurrence of some rainfall events may also result in the transition of landslides activity from dormant to active [Canuti et al., 1979]. The prevalence of landslides in the Arno river basin poses a great risk to vulnerable elements considering the high density population within the basin. More than 16,000 civil buildings, 460 industrial areas and 350 km of roads are affected by landslides. Over the basin ca. 6 billion euro losses were predicted in the upcoming 30 years [Catani et al., 2005b].

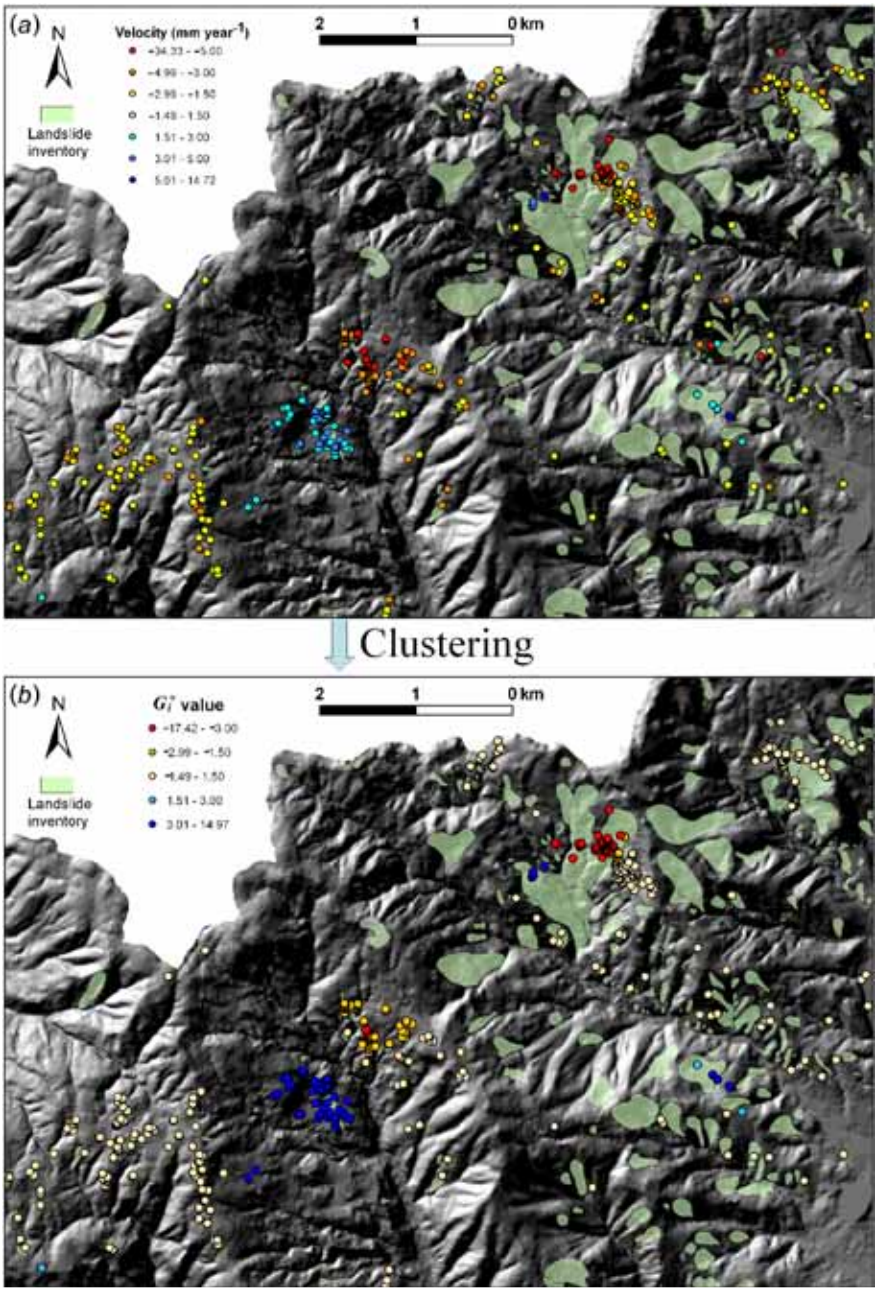

Figure 4.4: The clustering of PS using Getis-Ord G_i^* statistic, in northern part of the basin in Pistoia Province: (a) the PS distribution map before clustering using a color rendering on velocity; (b) the PS distribution map after clustering, with a color coding of derived G_i^* values.

4.4 Methodology

The spatial distribution of velocities, as visible from a standard point-based map using a color coding, is clearly scattered and affected by noises (figure 4.4(a)). Furthermore, it offers no reliable information on the probability of movement for intervening areas. For a better understanding of the connection between preparatory terrain-related factors and landslide processes for hazard mapping purposes, it is necessary to average in some way the point data and to spatially distribute displacement figures for obtaining a continuous estimate (figure 4.4(b)). This is even truer in the case of mass movements, which occur in specific areas with discontinuous nature and tend to cluster.

To automatically detect extremely slow-moving landslides from large amount of PS distributed within the basin, a new spatial statistic approach known as PSI-HCA is introduced. The purpose is to automatically identify concentrations of high velocity PS. Here high 'velocity' does not refer to the landslide velocity scale, but to PS displacement rates, usually over 4–5 mm/year which is fairly large compared to the technique precision mentioned above (0.1–2 mm/year). For landslides 4–5 mm/year movement is extremely slow [Cruden and Varnes, 1996; Varnes, 1978], but for displacement rates of PS it is significantly high (> 2 standard deviation).

The PSI-HCA approach is based on two statistics approaches: Getis-Ord G_i^* statistic and kernel density estimation.

4.4.1 Getis-Ord G_i^* statistic

The Getis-Ord G_i^* statistic [Getis and Ord, 1992, 1996; Ord and Getis, 1995] is a kind of local spatial statistic which represents the association up to a specified distance. The G_i^* statistic is applied in PSI-HCA in order to evaluate the clustering level of PS (G_i^* value in figure 2(b)). The statistic specifies a single PS at a site i, and its neighbors j within a searching distance d. For each single PS at a site i, the G_i^* index is calculated as:

$$G_i^*(d) = \frac{\Sigma x_j + x_i - n_{ij} \times \overline{x^*}}{s^*\{[(n \times n_{ij}) - n_{ij}^2]/(n-1)\}^{0.5}} \tag{4.4}$$

where n is the total number of PS datasets. n_{ij} is the number of PS in the vicinity of searching distance d, namely the summation of PS at the site i and its neighbors j. x is the velocity of PS. $\overline{x^*}$ is the mean value and s^* is the standard deviation of PS velocity for whole datasets.

In order to define the searching distance of d, a DTM of the Arno river basin with the spatial resolution of 10m was utilized. For each pixel of DTM, both the shortest path to a channel (referred as $d1$) and the shortest distance to a ridge pixel ($d2$) were calculated based on steepest descent direction as proposed by Tucker et al. [2001]. The searching distance of each pixel (d_i) was calculated using the mean value of $d1$ and $d2$, since the sum $d1$+$d2$ can be used as a proxy for slope length (the limiting dimension for a landslide over the same hillslope). An estimation of the searching distance d for a given step of G_i^* computation was rendered by the average value of d_i for all the DTM pixels in hilly and mountainous areas. In the case of the Arno river basin, the searching distance d is calculated as 114m compared with a DTM of 10m resolution.

This approach offers an easy and straightforward way to define the searching distance d. However, the reliability of this methodology can be decreased by inaccurate extraction of ridge and stream network, thus influencing the numerical computation of G_i^* index. This requests the availability of a good quality DTM. The very low resolution DTM often leads to an over-clustering of PS datasets, thereby resulting in an overestimation of landslides or the difficulty in differentiating landslides with other geophysical processes. In addition, a DTM with intensive noises can considerably underestimate the searching distance d as well as the clustering level. This always brings to a lack or underestimation of a potential landslide-affected area.

The G_i^* index was then calculated for each single PSI point target (figure 4.4(b)), choosing velocity as the weighting factor. The G_i^* index measures concentrations of high velocity PS compared with the entire dataset. The larger (positive) the G_i^* index is, the more intense the clustering of high velocity values it indicates, with moving displacement vector towards Line-of-Sight (LOS) of the satellite. The smaller (negative) the value is, the more intense the clustering of low velocity values (negative) it suggests, with the PS moving away from LOS.

4.4.2 Kernel density estimation

According to the G_i^* statistic analysis, the kernel density estimation was used in PSI-HCA in order to fit a smoothly tapered surface as a hotspot. Here is the kernel density calculation proposed by Silverman [1986]. It shows a kernel estimator which is defined as:

$$f(x) = \frac{1}{nh} \sum_{i=1}^{n} K(\frac{x - X_i}{h}) \tag{4.5}$$

where h is the window width, $x - X_i$ is the distance of each calculating pixel to each PSI target point i. K is the quadratic kernel function defined as:

$$\begin{cases} K(x) = \frac{3}{4}(1 - x^2), \mid x \mid \leqq 1 \\ K(x) = 0, x > 1 \end{cases} \tag{4.6}$$

The kernel estimator is then performed on PS, choosing the previous derived G_i^* index as the weighting factor. The output is a smooth kernel density map which converts large amount of PS into several hotspots for an easier and straightforward visualization.

4.5 Result

The output of PSI-HCA is a hotspot map which highlights areas preferentially affected by extremely slow-moving landslides. The result includes two types of hotspot maps: individual orbit (ascending or descending) map and combined map with an overlay of both ascending and descending orbits.

Figure 4.5 is the example of an individual hotspot map which separates the information provided by ascending (figure 4.5(a)) and descending (figure 4.5(b)) PS. Both ascending and descending hotspot maps cover the Pistoia-Prato-Firenze and the Mugello basin in the Arno river basin. In a preliminary phase, the flat area was masked out so that PSI-HCA was only performed on hilly areas for landslides detection. Both ascending and descending maps are displayed based on the kernel density estimation. Pixels with high positive values are rendered

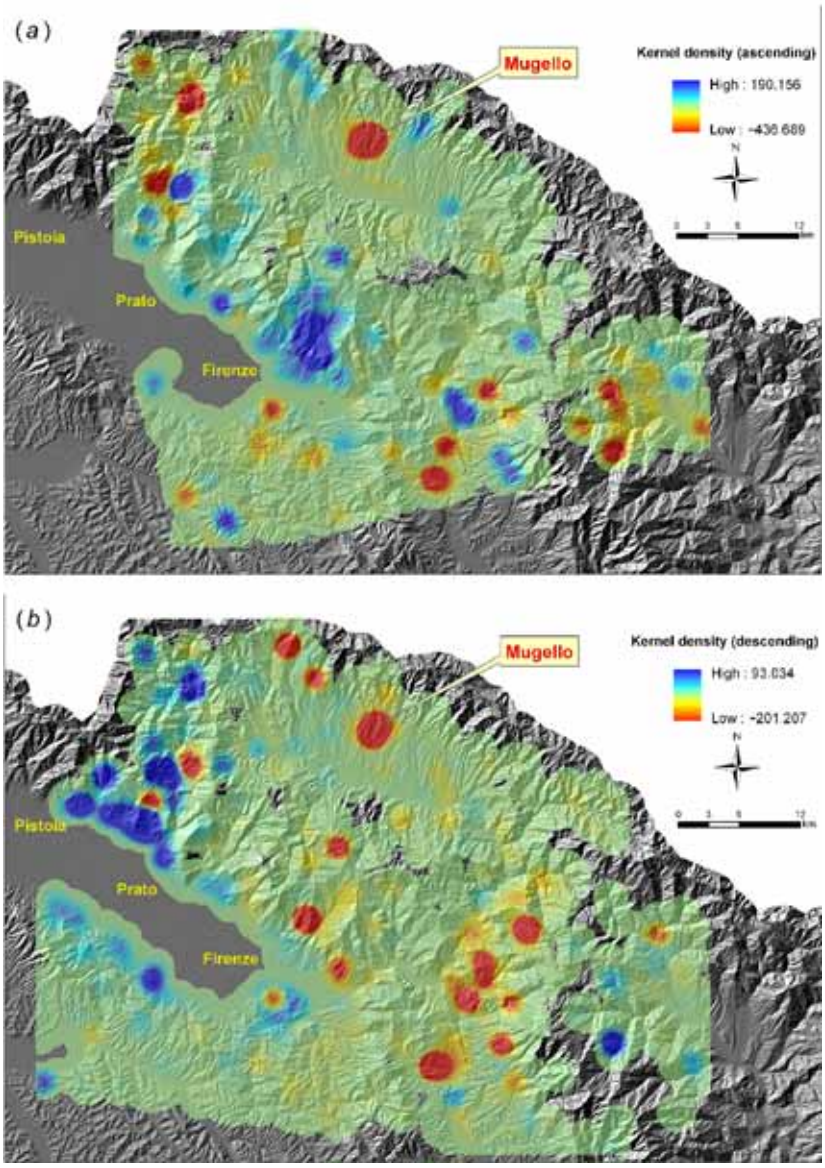

Figure 4.5: The PSI hotspot map of the Arno river basin covering the Pistoia-Prato-Firenze and Mugello basin area: (a) hotspot map derived from a kernel density estimation using ascending RADARSAT PS; (b) hotspot map derived from a kernel density estimation using descending RADARSAT PS. Red hotspot (low negative kernel density) indicates the clustering of high velocity PS moving away from sensor whereas blue hotspot (high positive kernel density) implies the clustering of high velocity PS moving towards sensor.

with blue color while clustering of low negative pixels is displayed with red color. Both blue and red hotspots indicate where mass movements exist. The deeper the color is, the more intense high-velocity PS are clustered, thereby indicating the existence of intensive mass movements. The color of hotspots provides the information of moving direction. Clustering of PS moving towards LOS (positive velocity) is indicated by blue hotspot whereas clustering of PS moving away from LOS (negative velocity) is plotted in red hotspot. Moreover, the radius of each hotspot implies the extent of a potential landslide-affected area.

Figure 4.6 is a hotspot map with an overlay of ascending and descending results in figure 4.5. The aim is to better visualize ground movements from two different looking directions of the sensor. Unlike the individual hotspot map in figure 4.5, the magenta areas in figure 4.6 are originated from the combination of red and blue hotspots. Some magenta hotspots are discovered in Vernio, Trespiano, Pomino, Carbonile and Rimaggio areas (see locations in figure 4.6). These hotspots suggest opposing moving directions (moving towards and away from LOS) detected separately by ascending and descending orbits, thus indicating the existence of horizontal components in the movement. The intensity of the clustering is displayed by its color deepness. The deeper magenta it displays, the more intense PS with high velocity are clustered. Also, deep blue hotspots that are prevalent in the north Pistoia-Prato-Firenze basin are overlays of two orbits. This can be interpreted as the same moving direction (moving towards LOS) that has been detected from both ascending and descending PS. Similarly, the deep red hotspot, such as the one in Mugello (see figure 4.6 for its location), shows both ascending and descending PS are moving away from LOS.

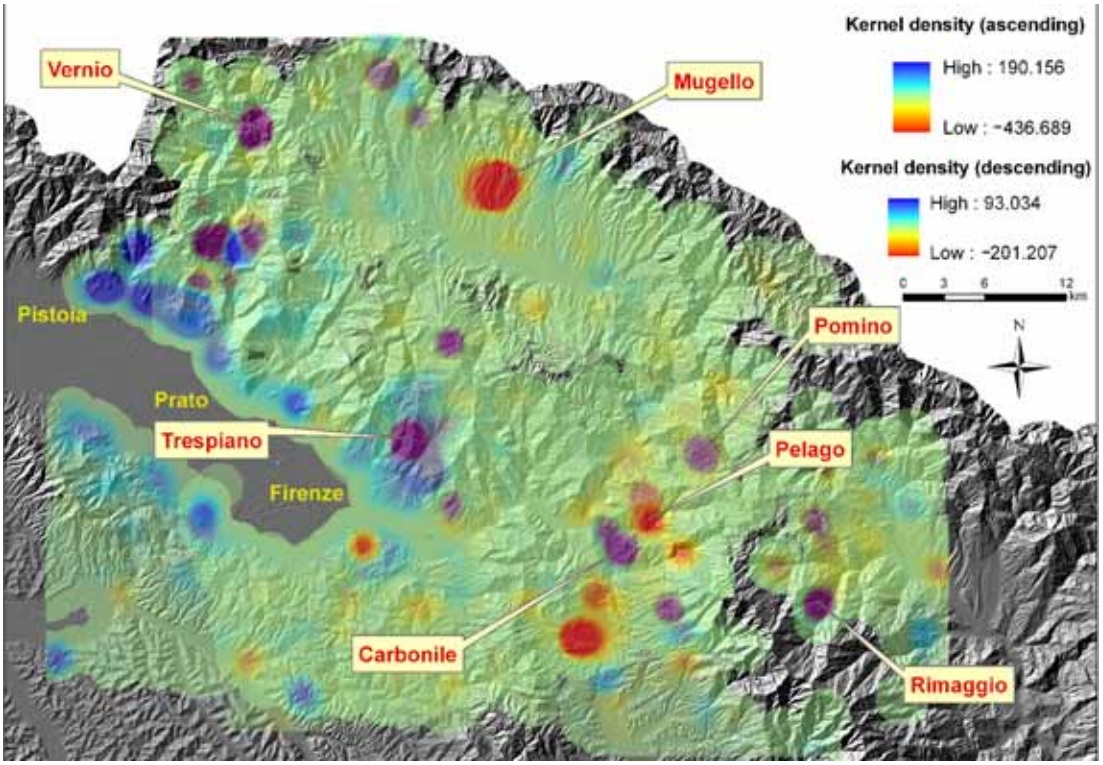

Figure 4.6: The PSI hotspot map obtained from a combination of ascending and descending data for the Pistoia-Prato-Firenze and Mugello basin area. The magenta hotspots indicate the clustering of high velocity PS detected by ascending and descending PS, with opposing LOS directions. The deep red and blue hotspots indicate the clustering of high velocity PS detected by both ascending and descending data, with consistent direction along LOS. The labelled hotspots have been chosen for results validation and further investigation.

4.6 Validation

In total 110 hotspots were obtained from ascending PS and 155 hotspots were detected from descending data. Accuracy assessment (table 4.4) was carried out by comparing the hotspot result with the existing landslide susceptibility map [Catani et al., 2005b], landslide inventory, aerial photos, historical archive data, optical image interpretation, topographic maps and some field surveys. 79.1% of

Table 4.4: Statistics about the results of PSI-HCA for landslide detection

	No. of hotspots	For existing landslide confirmation	%	For new landslide detection	%	Mis-detection of landslides	%
Ascending orbit							
Blue hotspot	38	26	68.4	7	18.4	5	13.2
Red hotspot	72	61	84.7	7	9.7	4	5.6
Total	110	87	79.1	14	12.7	9	8.2
Descending orbit							
Blue hotspot	54	18	33.3	17	31.5	19	35.3
Red hotspot	101	80	79.2	15	14.9	6	5.9
Total	155	98	63.3	32	20.6	25	16.2

the ascending and 63.2% of the descending hotspots are connected with existing landslides. Also, 12.7% of the ascending and 20.6% of the descending hotspots are associated with new landslides, thus providing an important source for updating landslide inventory. Detection errors also exist when mass movements are associated with other geophysical processes that PSI can identify but not discriminate. Especially for blue hotspots, the misdetection rate reaches to 13.2% for ascending and 35.2% for descending data. This is because down-slope landslide movements moving towards sensor can hardly be detected from PSI analysis.

4.6.1 Confirmation of existing landslides

The hotspot analysis provides an important support for confirming existing landslides in the Arno river basin. Compared to the landslide inventory which was previously mapped by the Arno river basin Authority and SLAM project [Catani et al., 2005b; Farina et al., 2006], 3203 landslides (14.9%, totally 21,444 landslides within orbit coverage) are confirmed by PSI-HCA, including intensively affected areas in Rimaggio, Pomino, Pelago, Vernio and Carbonile (see locations in figure 4.6).

A case study in Carbonile village (figure 4.7) is presented to illustrate the usefulness of PSI-HCA in landslide confirmation and further investigation. The area was affected by historical earth-slides reactivated in 1984, as a result of intense prolongated rainfall [Farina et al., 2006]. Currently mapped landslides are prevailed by translational and rotational slides. Several remedial works (including drainage collectors, trench drains and sheet piles) were built to stabilize slopes (see their distributions in figure 4.7). Also, a monitoring system composed of 30

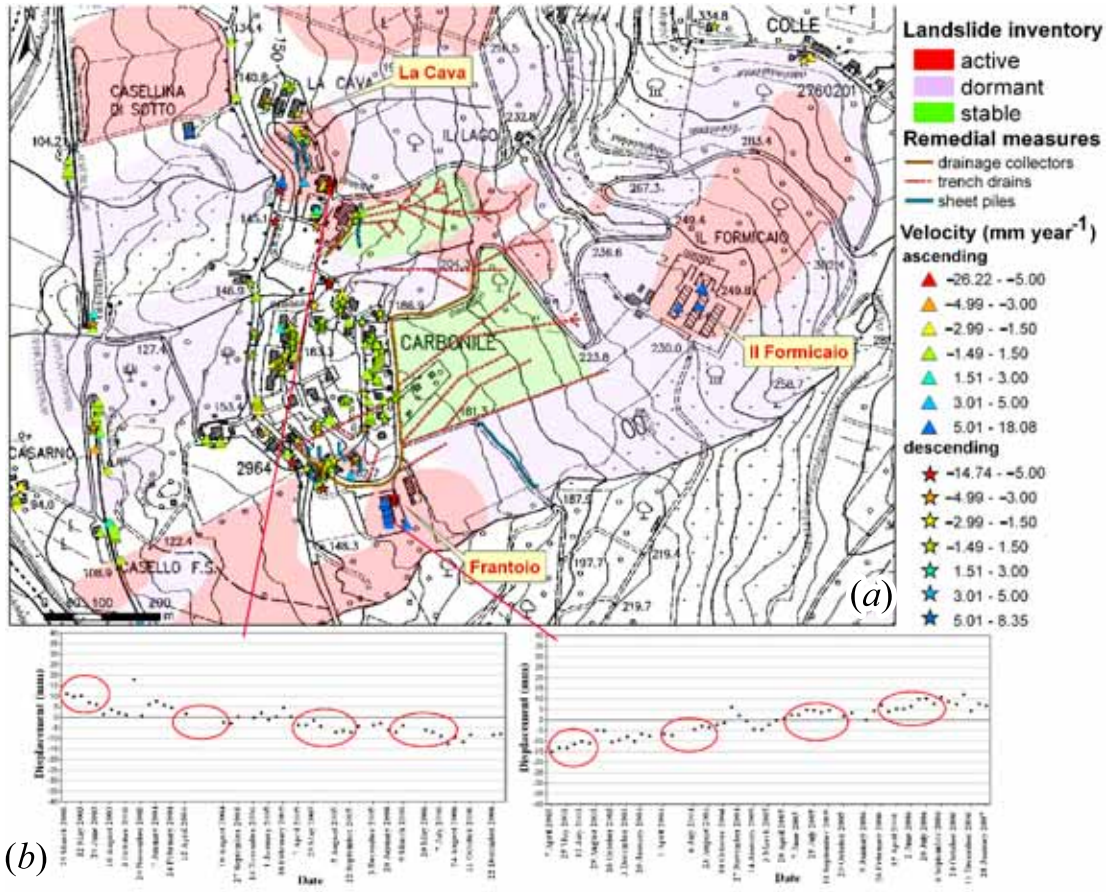

Figure 4.7: The Carbonile landslide as confirmed by PSI-HCA result: (a) RADARSAT PS (from 2003 to 2006) used for PSI-HCA are displayed. The landslide inventory is classified based on state of activity (active, dormant and stable). Several remedial works have been performed to stabilize the Carbonile village; (b) the time series of PS, indicated with the periods of displacement acceleration.

inclinometric tubes with piezometers was established after this reactivation.

The hotspot detected in Carbonile includes 211 RADARSAT PS covering the period from 2003 to 2006. 125 of them are from the ascending data and the other 86 PS are from the descending orbit. The maximum velocity detected by ascending data is 18.08 mm/year (positive value, moving towards LOS) and the

minimum velocity noticed by descending data is -25.04 mm/year (negative value, moving away from LOS). The result was compared with the investigation by Farina et al. [2006], which employs PS derived from 350 ERS images covering the period from 1992 to 2001.

The result of RADARSAT PS reveals that the central part of the village was observed to be stable during the period from 2003 to 2006, with PS velocity ranging from -3 to 3 mm/year. This observation is in accordance with the result from ERS PS. As mentioned above the decrease in velocity can be attributed to mitigation efforts carried out in the past few years. Major unstable sites are located in the north side zone called 'La Cava', in the 'Frantoio' area, in the south side zone 'Il Formicaio' and in the eastern part of the Carbonile village (see locations in figure 4.7). All sites are located in the upper part of the slope, just above those remedial structures. Velocity of PS ranges from 4 to 9 mm /year in 'La Cava'. The rate is equivalent to the monitoring result during period from 1992 to 2001 obtained from ERS PS. Also, accelerations of movement are detected in the time series of RADARSAR PS from 2003 to 2006 (figure 4.7). These accelerations are mainly occurring during the summer period of each year. In 'Frantoio', the mean PS velocity is -7.7 mm/year for descending data and 6 mm/year for ascending data. The rate is higher than the average velocity (4.5 mm/year) detected by ERS PS (1992 to 2001). Similar to the 'La Cava' area, some accelerations of movement during the summer period are suggested in the time series of RADARSAT PS (figure 4.7). The most unstable site is located in the 'Il Formicaio' area. The ground moving rate detected in this area ranges from -14 mm/year to -18 mm/year. The instability of 'Il Formicaio' turns out to be a consequence of lacking stabilization works. In the lower part of the slope, at least

300 m away from the affected area, there are existing drainage wells and sub-horizontal drainages. Such instability was also detected by the ERS PS whose average rate is around -8.7 mm/year. However, the movement has been increased since 2003 compared to previous 10 years.

4.6.2 New landslide detection

PSI-HCA is also an effective tool to detect new extremely slow-moving landslides. Ancillary inputs such as aerial photos, topographic maps and optical images can be integrated into hotspot and PS information for landslide mapping. To illustrate its applicability, a newly detected landslide in the cemetery of Trespiano (see location in figure 4.6) is presented. This landslide is situated a few kilometers north of Firenze. The lithology of this area is mainly composed of pelitic units with a downslope attitude of the geological beds. The landslide is considered to be a slow slide with the slip surface possibly located in correspondence of the pelitic layers.

The landslide was firstly detected by a hotspot indicated in figure 4.5 and figure 4.6. The hotspot represents a cluster of 678 RADARSAT PS from 2003 to 2006 (figure 4.8). Among them, 211 PS are from ascending orbit and 467 are from descending acquisition. The detection of this hotspot is owing to the existence of a cemetery which is built on the slope. Thus, a bunch of stable benchmarks are identified and they are recognized as buildings, walls, roads and man-made structures.

The orbit information reveals that ascending displacement vectors are oriented towards the sensor whereas the descending movements are away from LOS.

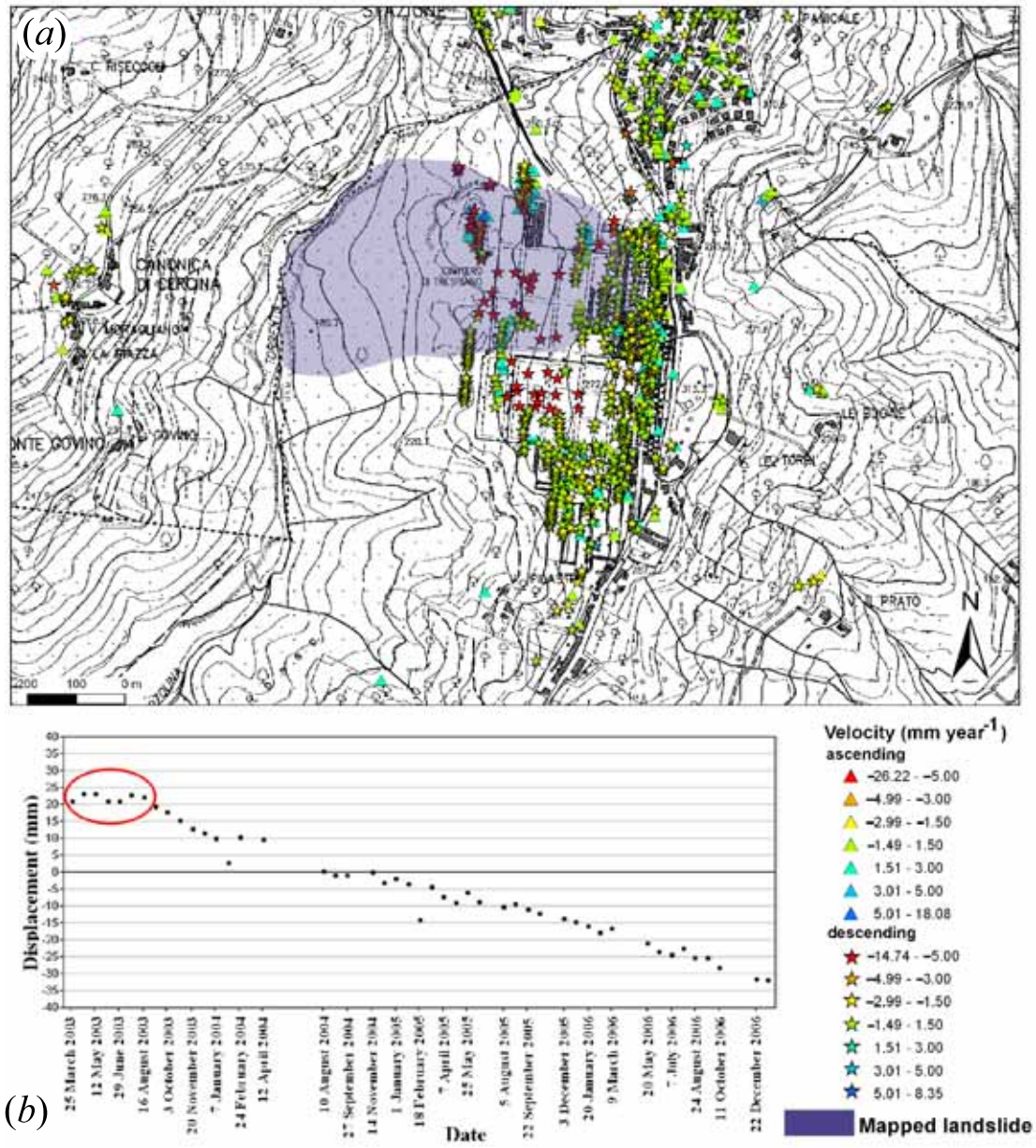

Figure 4.8: A landslide in the Trespiano cemetery detected by PSI-HCA: (a) RADARSAT PS distribution and mapping results of the new landslide; (b) the time series of PS located in the northern part of the cemetery.

It indicates the direction of ground movements is along the west-facing slopes.

No landslide located inside the cemetery is reported by the existing inventory.

Figure 4.9: The damaged walls (a), roads (b, c) and structures (d) inside the Trespiano cemetery.

Also, no evidence of movement is attested by ERS PS covering the period from 1992 to 2001. However, the time series of RADARSAT PS suggests that the

movement was accelerated since October 2003 (figure 4.8). The velocity of these RADARSAT PS in the cemetery reaches to 15 mm/year. Stable and unstable parts can be easily distinguished by checking the velocity distribution of PS where a sharp increase of velocity can be seen along the slope (figure 4.8). PS information in the lower part of the slope is missing because of a lack of stable scatterers.

The landslide was then mapped with the help of the topographic map and aerial photos. It was mapped across the northern part of the cemetery. The result was validated by the field evidences: a field check carried out in March 2009 discovered existing damages on walls, roads and structures (figure 4.9). The southern part of the cemetery was not included within the landslide because some stable PS are present (figure 4.8). However, the stability of the southern cemetery is not certain. Since PS velocity is measured along LOS and it is strongly affected by the change of slope inclinations, the stability indicated by these stable PS in the southern cemetery is probably influenced by the gentle slope of their locations (ca. 7°), thus possibly underestimating the displacement rate of these PS. Further investigations will be needed in the near future to better understand the possible deep structure and general dynamics of the mass movement, using field instrumentation. As a result of this study, the new detected landslide has been updated in the existing landslide inventory, classified as active slide as proposed by Cruden and Varnes [1996].

4.6.3 Ground movement related to other processes

PSI-HCA shows its usefulness in landslide detection in mountainous and hilly areas. However, ground motion detected by PSI-HCA is not only related to landsliding. The movement observed by PSI can also be associated with other geophysical processes. Concerning ground instability with downward movement away from LOS, landslide is not the only factor that InSAR can identify. Other geo-processes like local subsidence [Canuti et al., 2007; Ferretti et al., 2000; Massonet et al., 1997], sinkholes [Al-Fares, 2005; Ferretti et al., 2004], building consolidation [Stramondo et al., 2008], erosion [Smith, 2002], tectonics [Buergmann et al., 2006; Colesanti et al., 2003; Massonet et al., 1994; Vilardo et al., 2009] and underground works related to tunnelling or mining activities [Perski, 1998] could also be associated with detected displacements. Similarly, for upward movement (moving towards LOS) detected by PSI-HCA, some possibilities could be taken into consideration: uplift due to fluid injection [Doubre and Peltzer, 2007], excavation or abandonment of buildings, sedimentation of rivers [Smith, 2002] and tectonics again. Also, termination of activities related to subsidence can lead to the uplift detected by PSI. For instance, the area around Pistoia-Prato-Firenze basin (see location in figure 4.5 and 4.6) was usually well-known for the subsidence due to intensive pumping activities. However, due to the gradual termination of pumping activities since 2000, the area is detected with uplift motions from PSI interpretation [Lu et al., 2010]. These possibilities lead to some limitations in PSI-HCA and its interpretation. Possible mis-detection of landslides must warn us towards a careful interpretation process in which automated mapping procedures should always be backed by expert judgement.

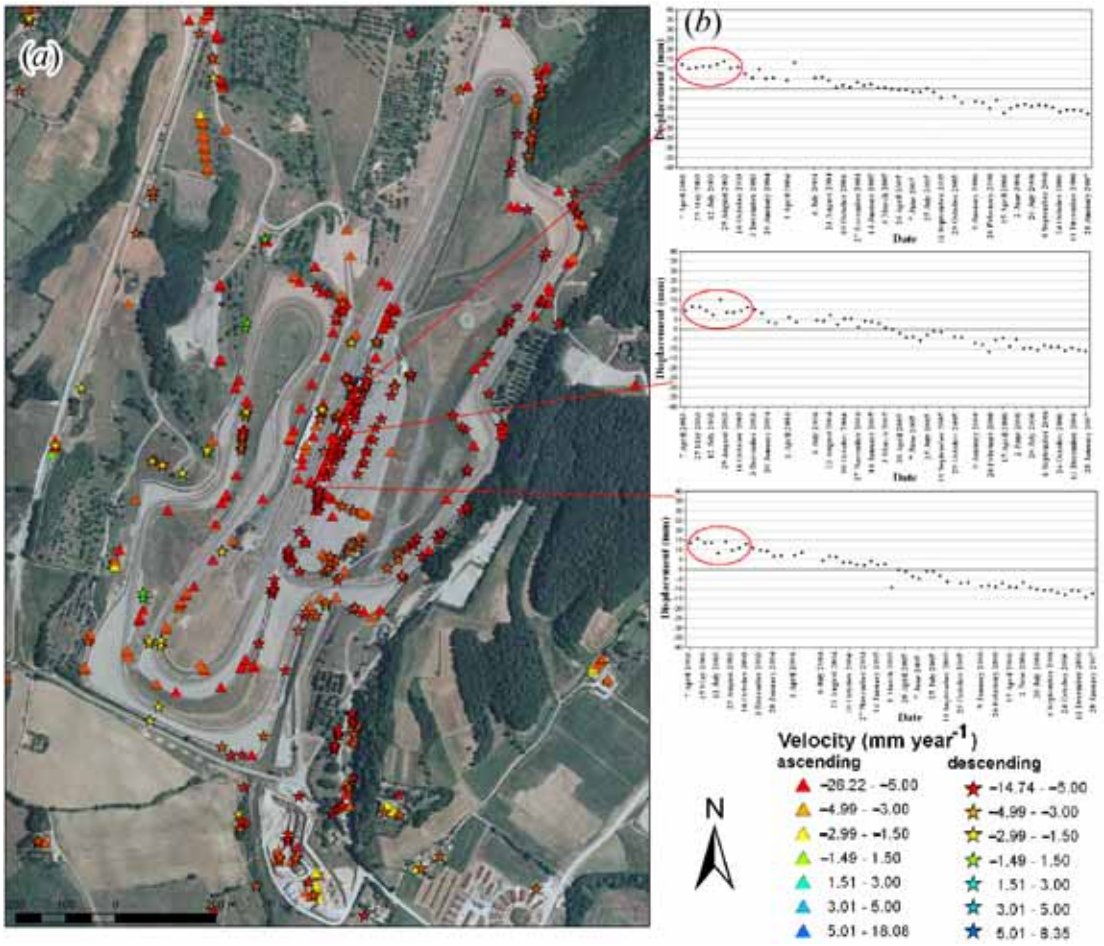

Figure 4.10: Ground movements in the Mugello circuit area as detected by PSI-HCA: (a) the RADARSAT PS distributed along the track; (b) the time series of PS indicating the acceleration of movements since the end of 2003.

An example of a hotspot related to a mixing of different geo-processes is presented. The case study is relative to a hotspot covering the Mugello and Scarperia area (see hotspot location in figure 4.5 and 4.6). The hotspot suggests that PS from both ascending and descending orbits are moving away from the sensor. Displacement rates of PS inside the hotspot reach up to 17.69 mm/year. The hotspot was firstly considered as a consequence of intensive landslide activity

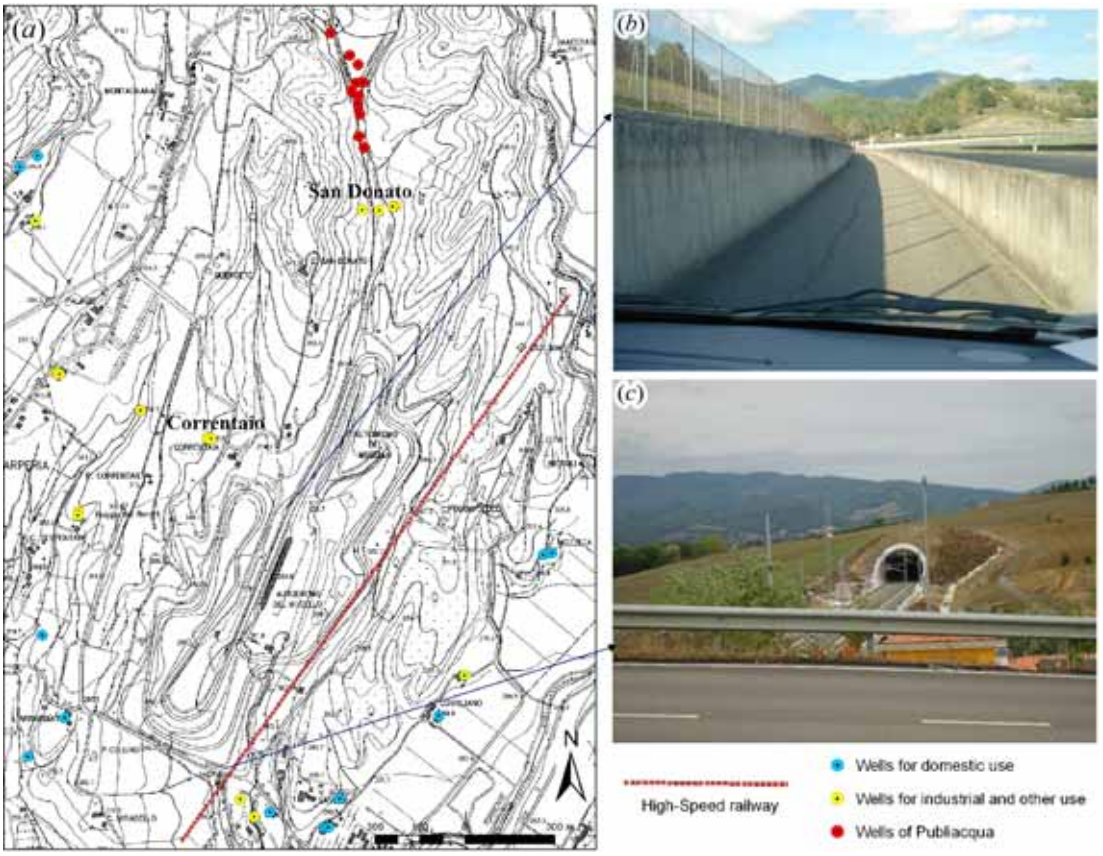

Figure 4.11: The Mugello circuit area: (a) the distribution of the pumping activities; (b) the field check confirms the existence of damages inside the circuit; (c) a view of the high-speed railway tunnel.

distributed in the Scarperia area. This interpretation is verified by the landslide inventory: a total of 25 landslides (15 of which are active) have been included in the hotspot. However, when the PS distribution is checked in greater detail, it can be noticed in figure 4.10 that a small cluster of PS with high velocity are located along the Mugello circuit which is the race track for Gran Prix motorcycle racing (MotoGP) and also the testing track for Ferrari Formula 1 team. The rapid ground motion of the circuit is not likely to be an outcome of landslides. No landslide was reported inside the inventory for the race track. Also, both

ascending and descending PS, distributed over differently exposed and sloping hillslopes, reveal a rapid ground movement away from LOS, thereby indicating the prevalence of downward ground movement. Considering the gentle slope (¡ 8°) of the circuit, other geo-processes might exist for the interpretation of the detected rapid mass movement.

Such considerations lead to the idea that ground subsidence has to be taken into account here. The subsidence was thought to be linked to two types of human activity. Firstly, the construction of the Italian high-speed railway tunnel might be considered responsible for the downward ground movement. This tunnel was built for the high-speed rail line which connects Firenze and Bologna. The location of the construction is below the eastern part of the Mugello Circuit (figure 4.11), with a maximum depth of 40m [Lunardi, 2000]. Therefore, the hypothesis of ground subsidence caused by the construction of this tunnel should not to be discarded. More details about the tunnel construction and its connection with the Mugello Circuit can be found in Lunardi [2000]. However, the tunnel was not likely to influence the whole area of the Mugello circuit because the excavation of the tunnel is not deep. Also, there is no evidence from PS is shown that the eastern part of the track is moving faster than the western part. As a result, the pumping activities in the surrounding area of the circuit can also be considered as an optional or joint cause. A database of wells was obtained from the Firenze Province. It records the type of use and the pumping rates for each well. According to the database, pumping activities are diffuse in the Scarperia and Mugello area. Several wells operating for different uses have been built around the Mugello Circuit (figure 4.11). In the San Donato area which is 500m north from the circuit, several pumping wells have been established for

industrial uses since 1996, at a depth of about 120m. Also, another large pumping facility managed by the company Publiacqua for public drinkable water supply is situated 200m north from San Donato. Still, in the Correntaio area which is 200m west of the race track, recent pumping activities at a depth of 380m have been established since March 2003. The time series of PS in figure 4.10 are harmonized with pumping activities in Correntaio. For PS located in the western part of the track, accelerations of ground movements can be observed from the end of 2003. This conformity indicates a likely connection between the ground subsidence and the newly established pumping activities.

Therefore, the hotspot covering the Mugello and Scarperia area is involved in various ground moving processes. These movements include landslides around Scarperia and the subsidence affecting the Mugello Circuit due to ground works of pumping and tunnel excavation. This example illustrates the limitation of PSI-HCA application in differentiating various geo-processes. As a result, additional data sources such as cartographic, optical imagery and in situ monitoring are needed for an accurate interpretation of PSI-HCA results in this area.

4.7 Conclusion

This chapter introduced an innovative approach for efficiently detecting extremely slow-moving landslides from PSI analysis. The approach is based on PSI-HCA which can automatically detect clustering of PS with locally high velocity. The advantage of this methodology takes both PS velocity and spatial distribution into consideration. When the flat area was masked out and only PS in mountainous and hilly areas were focused upon, PSI-HCA showed a high potential

for extremely slow-moving landslide detection. First, PSI-HCA outcomes can be used to confirm activities of existing landslides. 3203 (14.9% of total) existing landslides in the Arno river basin are confirmed by PSI-HCA derived hotspots. The detected landslides can be further studied for a deeper investigation of possible PSI-HCA interpretation keys, such as the illustrated example of the Carbonile landslide. Second, the proposed PSI-HCA can be useful for new landslide detection. The Trespiano landslide was detected and mapped by PSI-HCA on RADARDSAT PS from 2003 to 2006. Time series of PSI displacements over the same area show an acceleration of movement since October 2003 and this might well explain the absence of record in the previous landslide inventory. Both applications indicate that PSI-HCA presents an effective way for landslide inventory updating. However, detection errors cannot be avoided. The major errors can rise where the joint contributions of several geo-processes mix up in PSI measured displacements. In particular, the study in the Mugello Circuit area reveals that a hotspot can represent a mixing of different geophysical movements having similar displacement vectors. Notwithstanding this drawback, PSI-HCA seems still very promising. PSI-HCA could represent an efficient way to extract useful information from large amount of PSI data especially considering the rapid development of short wavelength X-band sensors which largely increases PS density and decreases the revisit time. Future improvements should include, as priority objectives, a better spatial definition of the G_i^* statistic parameterizations (e.g. by spatially distributing d_i values) and the possible inclusion of some series in spatial averaging schemes.

Chapter 5

Landslide hazard and risk assessment

5.1 Landslide hazard and risk mapping: literature review

5.1.1 Landslide risk

There are many efforts contributed to give a generalized definition of 'landslide risk'. Among them, one of the most used definition, was given by Varnes [1984], defined as 'the expected number of lives lost, person injured, damage to property and disruption of economic activity due to landslide occurrence for a given area and reference period'. Besides this, another well-accepted definition was illustrated in ISDR [1999], which concludes landslide risk as 'the probability of harmful consequences, or expected losses (deaths, injuries, property, livelihoods, economic activity disrupted or environment damaged) resulting from interactions

between landslide hazard and vulnerable conditions'. Nevertheless, it is widely agreed that these definitions of landslide risk can be quantitatively assessed with the formula as the product of hazard, vulnerability and amount [Catani et al., 2005b; Fell, 1994; Remondo et al., 2008; van Westen et al., 2006; Varnes, 1984], written as:

$$Risk = Hazard \times Vulnerability \times Amount \tag{5.1}$$

The application of this formula can be found in many literatures regarding landslide hazard and risk assessment, with different applied scales in different case studies [Cardinali et al., 2002; Catani et al., 2005b; Guzzetti, 2000; Guzzetti et al., 2005b; Jaiswal et al., 2010; Kanungo et al., 2008; Lee and Pradhan, 2006; Michael-Leiba et al., 2003; Nadim et al., 2006; Pradhan and Lee, 2009; Remondo et al., 2005, 2008; Sassa et al., 2004; Sterlacchini et al., 2007; Zezere et al., 2007, 2008].

It should also be noted that, aiming at a uniformity in terminology and landslide zoning structure, a guideline for landslide susceptibility, hazard and risk zoning was recently proposed by Fell et al. [2008], introduced with a general framework for landslide risk management.

5.1.2 Landslide hazard

Landslide hazard can be defined as the probability of landslide with a given intensity occurrence within a given area and period [Catani et al., 2005b; van Westen et al., 2006; Varnes, 1984]. According to this definition, the landslide hazard should take both spatial and temporal probability into consideration.

The spatial probability of landslide occurrence, or more appropriately called landslide susceptibility, can be estimated from remote sensing data or derivatives, based on a bunch of statistical approaches. The most-used approaches include discriminant analysis [Baeza and Corominas, 2001; Cardinali et al., 2002; Carrara et al., 1991, 2003; Guzzetti et al., 1999; Nagarajan et al., 2000; Santacana et al., 2003], artificial neural network [Catani et al., 2005b; Choi et al., 2010; Ermini et al., 2005; Falaschi et al., 2009; Gomez and Kavzoglu, 2005; Lee et al., 2004; Melchiorre et al., 2008; Nefeslioglu et al., 2008; Pradhan et al., 2010], likelihood ratio [Chung and Fabbri, 2003; Dewitte et al., 2010; Fabbri et al., 2003; Lee, 2004; Lee et al., 2007] and logistic regression [Ayalew and Yamagishi, 2005; Bai et al., 2010; Das et al., 2010; Eeckhaut et al., 2006; Falaschi et al., 2009; Lee, 2005, 2004].

The temporal probability is always difficult to be estimated and this is why most studies only focus on landslide susceptibility analysis [Ermini et al., 2005; van Westen et al., 2006]. Temporal probability is generally determined by historical records related to those triggering factors, or temporal historical landslide inventory itself if available, or estimated from those dynamic models [Guzzetti et al., 2005a; van Westen et al., 2006], including those widely-used models as proposed (e.g. Crosta [1998]; Guzzetti et al. [2005a]; Reichenbach et al. [1998]; Terlien [1998]).

5.1.3 Landslide intensity

The term ‘landslide intensity’, according to Hungr [1997], is defined as ‘a set of spatially distributed parameters describing the destructiveness of landslide’.

There is no common approach for landslide intensity assessment [Hungr, 1997]. Generally landslide intensity can be determined qualitatively and quantitatively based on a bunch of spatially distributed parameters of the landslide destructive power. A common measurement of relative intensity is related to kinetic characteristics, which could be defined as the function of estimated landslide volume and velocity using qualitative assessment [Cardinali et al., 2002; Hungr, 1995]. Nevertheless, a more complicated analysis can be carried out based on the prediction of runout distance of landslides (e.g. Corominas [1996]; Hungr [1995]; Revellino et al. [2004]; Sassa [1988]). In addition, Dai and Lee [2001] employed a magnitude-cumulative frequency relationship to define intensity classes for rainfall-triggered landslides.

5.1.4 Vulnerability and exposure

The vulnerability, ranging from 0 to 1, indicating from no destruction to full damage, describes the expected damage or the degree of loss, for an element at risk due to a landslide occurrence of a given intensity within the landslide-affected area [Catani et al., 2005b; Dai et al., 2002; Fell, 1994]. Exposure is closely related to vulnerability in practical assessment, often referring to the number of lives or the value of properties exposed at risk [Catani et al., 2005b; Schuster and Fleming, 1986].

It is hard to find a generalized or standard approach for quantitatively classifying and assessing the vulnerability of elements at risk to the types and magnitudes of specified landslides [Li et al., 2010]. Dependent on the available data, scale, areas and conditions, there are different methods to define vulnerability for

different properties. Some recently developed approaches for landslide vulnerability assessment include historical records [Finlay, 1996; Remondo et al., 2008; Zezere et al., 2008], damage matrices [Leone et al., 1996], 3D conceptual network [Duzgun and Lacasse, 2005], fragility curves [Mavrouli and Corominas, 2010] and function of landslide intensity and susceptibility [Kaynia et al., 2008; Uzielli et al., 2008].

5.2 Problem definition

The previous works mentioned above are mainly dealing with the application of remote sensing data in semi-automatic landslide mapping and detection. In particular, two semi-automatic approaches, OOA and PSI-HCA, were respectively introduced in chapter 3 and 4. These two semi-automatic techniques however focus on two different types of mass movements. In terms of OOA-based approach, it primarily concentrates on a quick mapping of rapid-moving shallow landslides and debris flows, for the purpose of an immediate response after a landslide emergency and an efficient risk management and decision making. Instead, the approach of PSI-HCA chiefly focuses on a semi-automatic detection of (extremely) slow-moving deep-seated landslides, for landslide hazard mitigation and following risk reduction, such as the case study previously illustrated in the village of Carbonile.

Although both two methods were initially developed for the same purpose: a rapid identification of landslide hazard, it is not easy to compare the results of them. The output of OOA-based approach is the semi-automatically generated landslide inventory whereas the outcome of PSI-HCA is a hotspot map indicat-

ing where the potential mass movements that could possibly exist. Both of these two approaches seem to be independent from each other, also because they were processed separately using diverse inputs of remote sensed data, which are significant different in terms of precision, accuracy and uncertainties. This leads to the particular difficulty in comparing the outputs of these two approaches.

One possible solution could be integrating these outputs in landslide hazard and risk assessment. In particular, the comparison at risk level is preferred because hazard analysis is only focusing on the probability of occurrence, which is still ambiguous for a quantitative comparison purpose. For example, supposing in a specified area, the hazard of slow-moving landslide is 0.9 whereas the hazard of rapid-moving landslide is 0.5, it cannot simply justify that the harmful consequence or expected losses of slow-moving landslide is higher than those of rapid-moving landslide, because 0.9 and 0.5 are only the probability of occurrences of these two hazards. As a result, to some extent it is more suitable and clearer to involve a quantitative risk assessment for comparing these two outputs from OOA and PSI-HCA.

The output of OOA-based landslide mapping is an event-based landslide inventory, without which it is often making a quantitative risk assessment very difficult to be performed [van Westen et al., 2006]. The landslide hazard and risk assessment from historical landslide inventory has already been widely used, and to some extent landslide inventory-based probabilistic method is best for quantitative risk assessment compared to other methods such as heuristic, statistical and deterministic approaches [van Westen et al., 2006]. A common approach is to derive frequency-size statistics of landslides from historical inventory such as indicated in Malamud et al. [2004]. Similarly, Chau et al. [2004] estimated

frequency-volume statistics of landslides through the historical inventory ranging from 1984 to 1998 for calculating return period and hazard zonation in Hong Kong. This approach can also be similarly used in hazard and risk assessment of rockfall, such as the case study in the Yosemite Valley of California illustrated by Guzzetti et al. [2003]. Besides, Crovelli [2000] have indicated two probability models suitable for landslide hazard assessment from historical inventory data: continuous and discrete time-based models. Also, Coe et al. [2004] have performed a probabilistic assessment of precipitation-triggered landslides using historical records of landslide occurrence during the period 1909 to 1999 in Seattle as inputs to their Poisson and binomial probability model. Moreover, Finlay et al. [1997] have combined both probabilistic and heuristic methods, using historical landslide inventory, for calculating probability of those triggering factors of landslides in Hong Kong. The similar approach can also be found in the study of New Zealand as described by Crozier and Glade [1999]; Glade and Crozier [2005].

However, how to integrate PS hotspot and clustering analysis with quantitative landslide hazard and risk assessment at the regional scale remains a challenge. Because of the recently-developed methodology, a quantitative risk assessment from InSAR-derived landslide hotspot map was never attempted. In this chapter, in order to fill this research gap, a new approach of quantitative risk hazard and assessment for slow-moving landslide using derivatives from PSI-HCA is introduced, choosing the same area of PSI-HCA, the Arno river basin, as the case study.

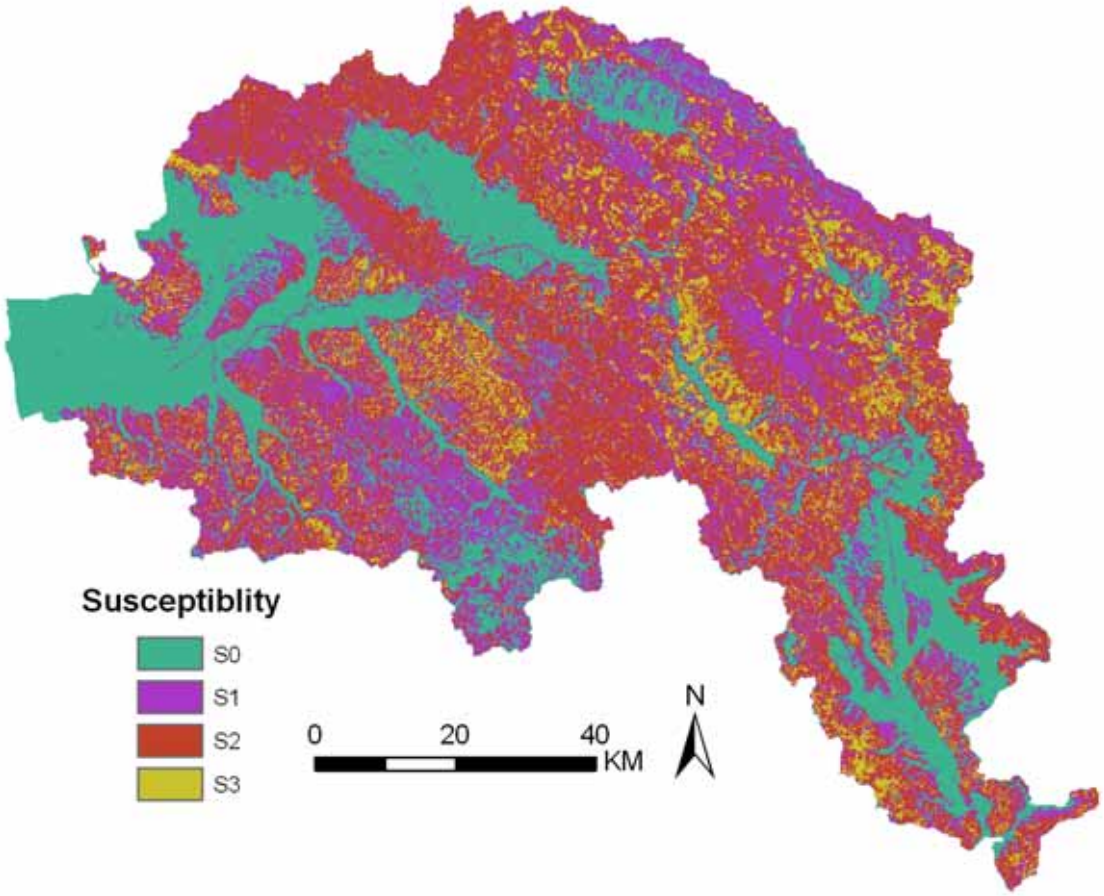

Figure 5.1: The landslide susceptibility map of the Arno river basin, as provided by Catani et al. [2005b].

5.3 Susceptibility and hazard assessment

5.3.1 Susceptibility: spatial prediction

The landslide susceptibility in the Arno river basin has previously been mapped by Catani et al. [2005b]. Since landslide susceptibility is only focusing on spatial probability of occurrences, regardless of temporal prediction, the susceptibility map was also used in this study with the same area focused.

The methodology to derive this susceptibility map was fully described in

Catani et al. [2005b]. The method is based on the artificial neural networks (ANN). Five preparatory factors related to instability were selected for the univariate statistical analysis: slope angle, lithology, profile curvature, land cover and upslope contributing area. Among them, slope angle, profile curvature and upslope contributing area factors were derived from a 10m DTM, respectively classified into 5, 3 and 3 classes. Land cover map were classified into 9 classes according to the legend of CORINE (Coordination of Information on the Environment) land cover project [Heyman et al., 1994]. Lithology map was published by Canuti et al. [1994] and was reclassified into 8 classes. The statistical prediction was then performed on the basis of unique condition units (UCU), with a preliminary training data. The derived susceptibility map can be found in figure 5.1 and it is classified into 4 classes (S0, S1, S2, S3, assorted with increasing susceptibility).

5.3.2 Hazard: temporal prediction

The landslide hazard, namely the temporal prediction of landslide occurrence, was accomplished on the basis of the previously derived landslide hotspot map (refer to figure 4.5, figure 4.6) which is derived from the approach of PSI-HCA as described in chapter 4.

At the beginning stage, five hazard levels (H0, H1, H2, H3, H4, assorted referring to increasing hazard levels) was initially determined from the kernel density values of the hotspot map. Ascending (figure 4.5) and descending (figure 4.6) hotspot maps were used separately for hazard analysis. This is due to the independent PSI processing of SAR images for different orbits, reflected in the

Table 5.1: The algorithm of assigning hazard levels from kernel density values of hotspot map

Ascending orbit	
Red hotspot	
H4:	kernel density < -280
H3:	-280 < kernel density < -140
H2:	-140 < kernel density < -35
H1:	-35 < kernel density < 0
Blue hotspot	
H4:	kernel density > 560
H3:	560 > kernel density > 280
H2:	280 > kernel density > 70
H1:	70 > kernel density > 0

Descending orbit	
Red hotspot	
H4:	kernel density < -200
H3:	-200 < kernel density < -100
H2:	-100 < kernel density < -25
H1:	-25 < kernel density < 0
Blue hotspot	
H4:	kernel density > 400
H3:	400 > kernel density > 200
H2:	200 > kernel density > 50
H1:	50 > kernel density > 0

difference in acquisition date, master images, reference points and coherence map. For each orbit, blue and red hotspots, indicating different moving directions of mass movements along LOS, were individually analyzed for initial hazard zonation. The algorithm for assigning five initial hazard levels were summarized in table 5.1. The boundary and threshold for hazard zonation were derived from heuristic determination by classifying hotspot maps into different levels. For each orbit, the zonation boundaries were respectively chosen as 10, 5 and 2.5 standard

Table 5.2: The probability of landslide occurrence for different hazard levels and time spans

	Recurrence time(yrs)	H(2 yrs)	H(5 yrs)	H(10 yrs)	H(20 yrs)	H(30 yrs)
H4	1	1	1	1	1	1
H3	10	0.1900	0.4095	0.6513	0.8784	0.9576
H2	100	0.0200	0.0490	0.0956	0.1821	0.2603
H1	1000	0.0020	0.0049	0.0099	0.0198	0.0296
H0	10000	0.0000	0.0005	0.0010	0.0019	0.0029

deviation for red hotspots and 20, 10, 5 standard deviation for blue hotspots.

After, the initial hazard classification estimated from hotspot map was compared with the susceptibility class (figure 5.1). For each pixel (10m), if initial hazard level is higher than corresponding susceptibility class, the final hazard level is then determined by the former value. Instead, if initial hazard level from the hotspot map is lower than the corresponding susceptibility level, the final hazard level was assigned from the values of the latter. This is due to the fact that underestimation of mass movements from PSI techniques possibly exists, resulted from a lack of stable benchmarks with high coherence values.

For each of these five hazard levels, a corresponding recurrence time was assigned (H0: 10,000 years, H1: 1000 years, H2: 100 years, H3: 10 years, H4: 1 year) as described in Catani et al. [2005b]. The temporal probability was then calculated for each hazard level, using the following equation as proposed by Canuti and Casagli [1996]:

$$H(N) = 1 - (1 - 1/T)^N \tag{5.2}$$

where T is the recurrence time, N is the time period for temporal probability assessment which was calculated here for 2, 5, 10, 20, 30 years respectively. The

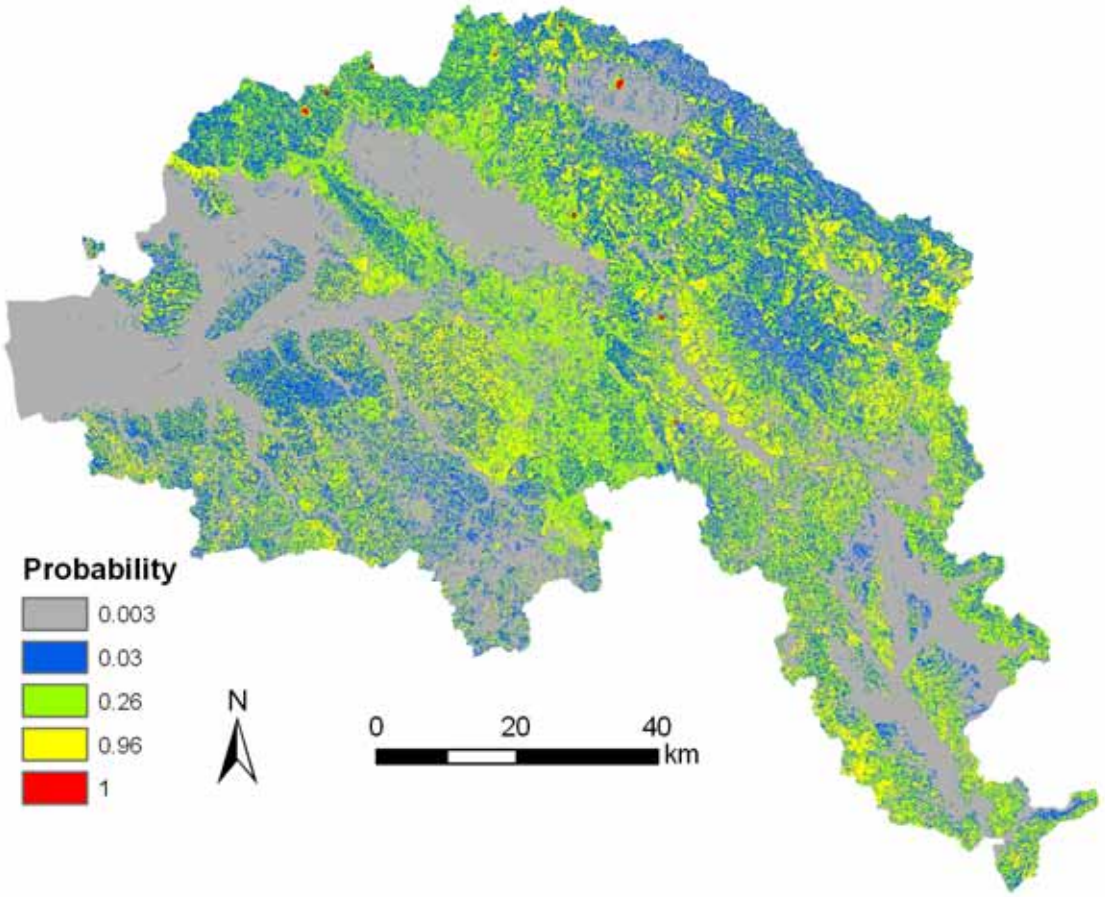

Figure 5.2: The landslide hazard map of the Arno river basin for 30 years, calculated from the landslide hotspot maps.

result of probability of occurrence for each hazard level is listed in table 5.2. It was assessed by five classes (from H0 to H4), with each corresponding probability of occurrences (from 0 to 1) over five time periods as mentioned above. An example of a derived hazard map over 30 years time period is displayed in figure 5.2.

5.4 Landslide intensity

As indicated by Hungr [1995], landslide intensity can be measured from the kinetic energy of mass movement, which is primarily considered as its volume and velocity, or a more complicated estimation of its run-out distance. In general, due to the difficulty in measuring velocity for slow-moving deep-seated landslides, the intensity is mainly measured from its estimated volume. For example, in the same study area of the Arno river basin, Catani et al. [2005b] measured the intensity of deep-seated landslides from the estimation of landslide volume using the post-failure geometry based the assumption that the shape of landslide is half-ellipsoidal. In this study, the intensity was additionally measured from the velocity of landslides, thanks to the technique of PSI which enables a detection of slow mass movement of millimeter accuracy. Besides, the PSI technique provides the complete time series record of landslides velocity over the period of processed SAR images, thus making possible a selection of maximum velocity of mass movement. This is especially useful for landslide intensity estimation due to the fact that landslide intensity is always determined by its maximum velocity instead of an average velocity over a period of time.

In this study, for each single PS, in order to remove noises, the time series data of PS was firstly smoothed using a moving average filtering with a smooth span of 5, given as:

$$v_s(i) = \frac{1}{5}(v(i+2) + v(i+1) + v(i) + v(i-1) + v(i-2)) \tag{5.3}$$

where $v(i)$ is the velocity calculated from the ith interferogram from two consecutive SAR images, namely the number of records for time series data of each

	v4	v3	v2	v1
I4	4	4	3	2
I3	4	3	2	1
I2	3	2	1	1
I1	2	1	1	1

Figure 5.3: The algorithm of rendering new intensity level based on kriging-interpolated velocity level v and current intensity level I mapped from landslide inventory.

single PS. $v_s(i)$ is the smoothed velocity after average filtering. Then the maximum velocity was selected from the time series of velocity for each single PS, for both ascending and descending orbits.

The intensity surface was then interpolated from the maximum velocity of PS incorporating the geostatistical approach of kriging [ESRI, 2008; Stein, 1999], with firstly quantifying the spatial structure of PS and subsequently performing a spatial prediction of other areas uncovered by PS data. The model of kriging employed the statistical relationships of spatial autocorrelation among the measured maximum velocity of PS for prediction of the surface. This was done by calculating its empirical semivariogram which estimated the squared difference between the velocity values for all pairs of PS locations.

The interpolated velocity surface was then classified into four classes: $v4$ (vel $>$ 10 mm/year), $v3$ (10 mm/year $>$ vel $>$ 4 mm/year), $v2$ (4 mm/year $>$ vel $>$ 2 mm/year), $v1$ (vel $<$ 2 mm/year). These four classes of velocity were used to

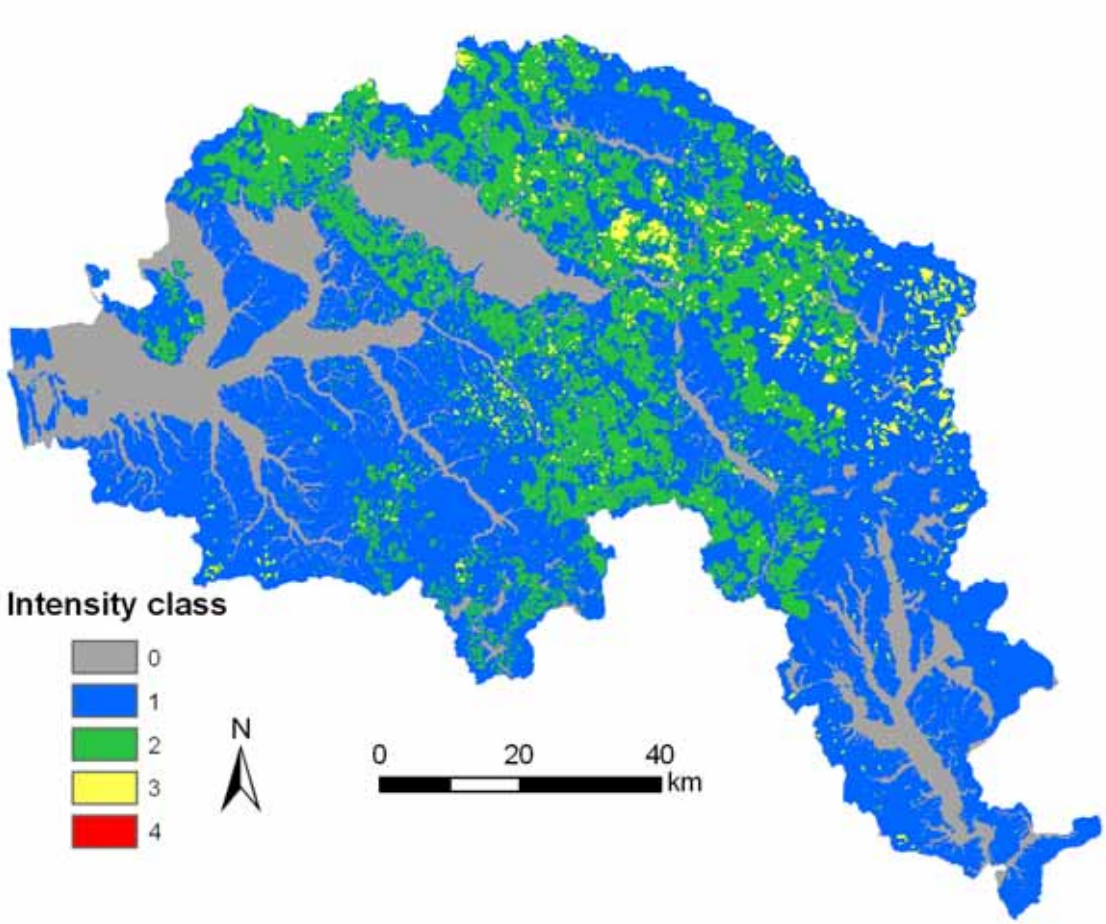

Figure 5.4: The landslide intensity map derived from the landslide hotspot map in the Arno river basin

define the level of intensity by a comparison with the intensity level ($I0$ to $I4$, with a significance of increasing intensity level) mapped by Catani et al. [2005b] from the existing landslide inventory. The comparison is on the basis of the classification matrix as indicated in figure 5.3. The intensity classification was performed for both ascending and descending orbits, which were subsequently merged into a unique intensity map based on the algorithm that higher intensity classes are used if one pixel has both values from two orbits. The final derived intensity map is displayed in figure 5.4.

5.5 Vulnerability and exposure

The vulnerability is generally defined as a function of a given intensity, as the expected degree of loss for an element at risk as a consequence of a certain event, ranging between 0 (without damage) to 1 (full destruction) [Fell, 1994; Varnes, 1984]. Exposure instead is more related to the practical use of vulnerability, usually considered as the number of lives or the value of properties exposed at risk [Schuster and Fleming, 1986].

The selection of these elements at risk for vulnerability assessment in this study was extracted based on the regional digital topographic maps at the scale of 1:10000. Besides, it is on the basis of an updated CORINE land cover map of 2002 at the scale of 1:50000 [Heyman et al., 1994]. A geodatabase of the elements at risks was then built, including the exposure values and vulnerability as a function of intensity which was previously determined. A detailed description of this geodatabase regarding vulnerability and exposure can be found in table 5.3. The elements at risk were classified into five categories: building, complex, road, railway and land cover. Each category was further subdivided according to their practical uses which render the exposure and vulnerability value for each element. For example, the complexes used for hospital and school are considered more vulnerable than sport facility, thus receiving higher values for exposure and vulnerability.

Table 5.3: Exposure and vulnerability for elements at risk. V refers to vulnerability (%) as a function of intensity I.

Code	Description	Exposure (euro/m^2)	$V(I0)$	$V(I1)$	$V(I2)$	$V(I3)$	$V(I4)$
Building							
201	Public, social, administrative building	3000	0	5	10	30	60
202	Industrial, commercial building and factory	1000	0	5	10	20	50
203	Religious building, bell tower, tabernacle	4000	0	5	15	30	60
204	Building under construction	100	0	5	15	30	40
205	Abandoned, ruined building	10	0	5	20	50	60
206	Projecting body, portico, loggia	100	0	5	10	20	40
207	Shed, kiosk	100	0	5	15	50	60
208	Awning, dormer window	10	0	5	10	20	40
209	Pressurized dome	10	0	5	20	50	60
210	Permanent greenhouse	10	0	5	20	40	60
211	Tollgate, railway station or stops	2000	0	5	10	30	50
212	Power station, power substation, power shed	2000	0	5	10	20	50
213	Monument	100	0	5	15	40	50

215	Nursery greenhouse	10	0	5	20	40	60
216	Stable, barn/breeding farm	10	0	5	15	40	60
217	Tower, chimney	100	0	5	15	40	50
218	Silo	10	0	5	15	40	50
219	Cross, tabernacle	1	0	5	10	30	40
Complex							
223	Hospital complex	4000	0	5	10	50	70
224	School complex	4000	0	5	20	50	70
225	Sport facility	100	0	5	10	25	50
226	Religious building complex	4000	0	5	15	50	70
227	Civil complex	4000	0	5	10	30	50
228	Cemetery complex	100	0	5	10	30	50
229	Campground, resort	100	0	5	20	50	80
Road							
301	Highway	200	0	5	30	50	80
302	Regional highway	100	0	5	40	60	100
303	Provincial road	50	0	5	50	80	100
304	Local road	50	0	5	60	80	100
Railway							
NA	In use, bridge, $>$ 2 platforms	300	0	5	10	50	100
NA	In use, gallery, 2 platforms	250	0	0	0	10	20
NA	In use, bridge, 2 platforms	250	0	5	10	50	100
NA	In use, railway, $>$ 2 platforms	200	0	10	30	70	100

NA	In use, railway, 2 platforms	150	0	10	30	70	100
NA	In use, gallery, 1 platform	200	0	0	0	10	20
NA	In use, bridge, 1 platform	200	0	50	20	60	100
NA	In use, street, 1 platform	100	0	10	40	80	100
NA	In use, railway, 1 platform	100	0	10	40	80	100
NA	No in use, bridge, 1 platform	20	0	5	30	60	100
NA	No in use, railway, 1 platform	20	0	10	40	80	100
Land cover							
111	Urban areas	50	0	5	20	30	60
112	Urban areas (discontinued)	30	0	5	20	30	60
120	Industrial areas	30	0	5	20	30	60
131	Quarries	1	0	5	40	60	80
132	Landfills	1	0	5	30	50	70
133	Yard	1	0	5	20	30	60
140	Artificial green zone	5	0	5	30	50	70
210	Cultivated crops	2	0	5	30	50	70
221	Vineyards	4	0	5	50	70	90
222	Fruit yards	5	0	5	40	70	90
223	Olive groves	5	0	5	40	70	90
231	Grassland	1	0	5	20	40	50
240	Farm	2	0	5	40	60	70
310	Tree	2	0	5	20	40	60

320	Vegetation	1	0	5	20	30	50
330	Graze	1	0	5	10	20	30
400	Wetland	1	0	5	10	20	30
511	canal, waterway	1	0	5	10	30	60
512	water basin	1	0	5	10	20	40

5.6 Quantitative risk assessment

The quantitative risk assessment was performed with the direct application of the equation 5.1 as indicated by Catani et al. [2005b]; Fell [1994]; Remondo et al. [2008]; van Westen et al. [2006]; Varnes [1984]: $Risk = Hazard \times Vulnerability \times Amount$. The calculation was fulfilled with each pixel with spatial resolution of 10m, completed for five different times spans of 2, 5, 10, 20 and 30 years, respectively. The final output is a 10m resolution landslide risk map with each pixel indicating the amount of expected loss in euros. An overview of landslide risk maps (2, 5, 10, 20, 30 years) is rendered in figure 5.5.

The total estimated economic loss is summarized in table 5.4, indicating the potential losses (euro) in the upcoming 2, 5, 10, 20 and 30 years. In particular, ca. 3.22 billion euro loss was expected in the upcoming 30 years in the whole Arno river basin, due to the slow-moving landslides within the detection range of PSI technique. The approximate losses for 20, 10, 5 and 2 years are respectively 2.72, 1.86, 1.14 and 0.54 billion euro. The increase of risk with time is nonlinear, similar to that observed by Catani et al. [2005b].

Compared to the previous risk mapping conducted by Catani et al. [2005b],

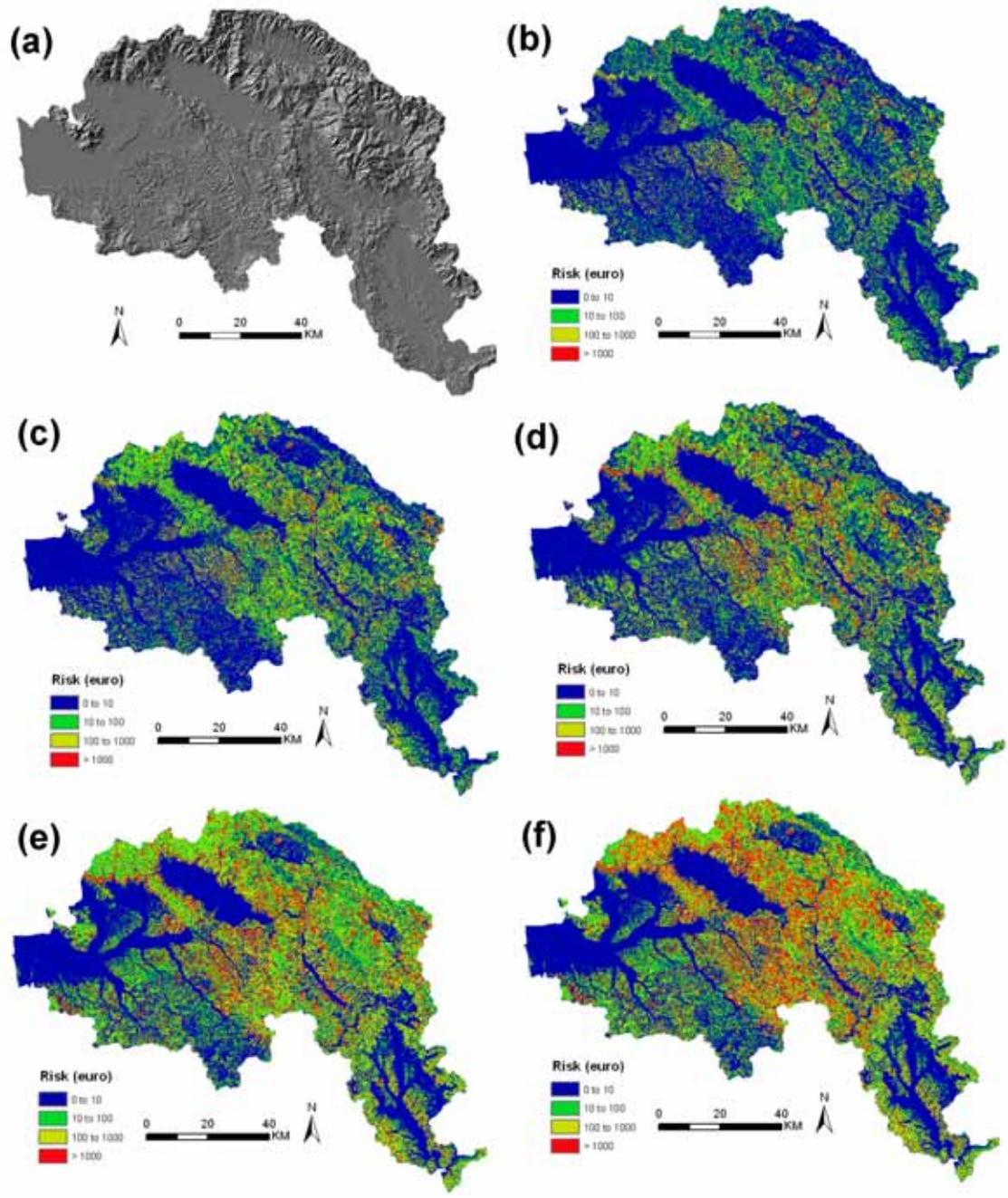

Figure 5.5: The landslide risk map estimated from landslide hotspot map in the Arno river basin: (a) shaded relief map, (b)–(f) risk map for 2, 5, 10, 20, 30 years respectively. See the corresponding number of losses in table 5.4.

Table 5.4: Landslide risks (losses in euros) in the Arno river basin calculated from PSI hotspot map for five time spans.

Time span (years)	Expected economic losses (euro)
2	543,980,444,2
5	1,143,746,730
10	1,864,851,052
20	2,721,273,302
30	3,224,446,172

the risk value in this study is significant lower. Catani et al. [2005b] expected ca. 6 billion euro loss for 30 years whereas the estimation in this study is ca. 3.22 billion euro. Also, Catani et al. [2005b] predicted a 1.6 billion euro loss for the upcoming 2 years, and in this study the prediction is around 0.54 billion euro. The decrease of the predicted risk is due to the fact that the risk assessment performed by Catani et al. [2005b] focused on all types of landslides in the inventory while in this study only the slow-moving landslides were concentrated on. This decrease is also reasonable because the major type of landslide in the Arno river basin is slow-moving rotational slides (about 74%). Another reason of the lower estimated risk is due to the limitation of PSI technique in areas without stable reflectors. This causes a low density of PS and a underestimation of landslide hotspot quantities. However, this limitation is expected to largely improved with these new processing approaches and the increasing wide use of X-band SAR sensors such as COSMO-SkyMed and TerraSAR-X.

5.7 Conclusion

This chapter primarily deals with a novel approach of quantitative landslide risk assessment using landslide hotspot map, the derivative from long-term InSAR

and PSI-HCA processing. The approach was developed and applied in the case study area of the Arno river basin. This quantitative landslide risk assessment provides a platform for comparing the derivatives of two semi-automatic landslide detection and mapping approaches: OOA for rapid-moving landslide mapping and PSI-HCA for slow-moving landslide detection. Since the application of OOA outputs, landslide inventory, in quantitative landslide risk assessment, has already been extensively developed, this study aims at filling a gap for another semi-automatic landslide detection approach of PSI-HCA for landslide risk mapping.

This quantitative risk assessment was based on the equation as introduced by Catani et al. [2005b]; Fell [1994]; Remondo et al. [2008]; van Westen et al. [2006]; Varnes [1984]: $Risk = Hazard \times Vulnerability \times Amount$. The approach was benefited from the case study area of the Arno river basin, thanks to the availability of large dataset necessary for hazard, vulnerability and exposure (amount) assessment. In particular, a susceptibility map completed by Catani et al. [2005b] using ANN predictor was included in this study, subsequently combined with the kernel density values of the hotspot map, for a generation of landslide hazard maps for 5 temporal predictions of 2, 5, 10, 20 and 30 years. Besides, a landslide intensity map was determined by the velocity map interpolated from the maximum velocity of PS time series data using ordinary kriging method. With given intensity, elements at risks were extracted from a regional digital topographic map and a CORINE land cover map. The result of risk mapping was displayed for 2, 5, 10, 20 and 30 years. Particularly, an expected loss of ca. 3.22 billion euro was estimated for the upcoming 30 years.

Chapter 6

Discussion

6.1 OOA for landslide mapping

6.1.1 Segmentation optimization procedure (SOP)

Esch et al. [2008] have proposed a multi-level segmentation optimization procedure (SOP), which iteratively compares the spectral characteristics of image objects generated with multiple scales. A simplified version of this approach which uses less spectral information and automatically-derived threshold was used in this study.

Since the approach was trained and tested on images by the same sensor, a major research question is, is this SOP approach only data-specified, or it is also problem-specified for landslide object segmentation? That is, since the case study of Messina event was using Quickbird imagery, the proposed multi-scale optimization only works on this imagery or it is also possible to work well in other imageries? To answer this question, it should be understood what is the

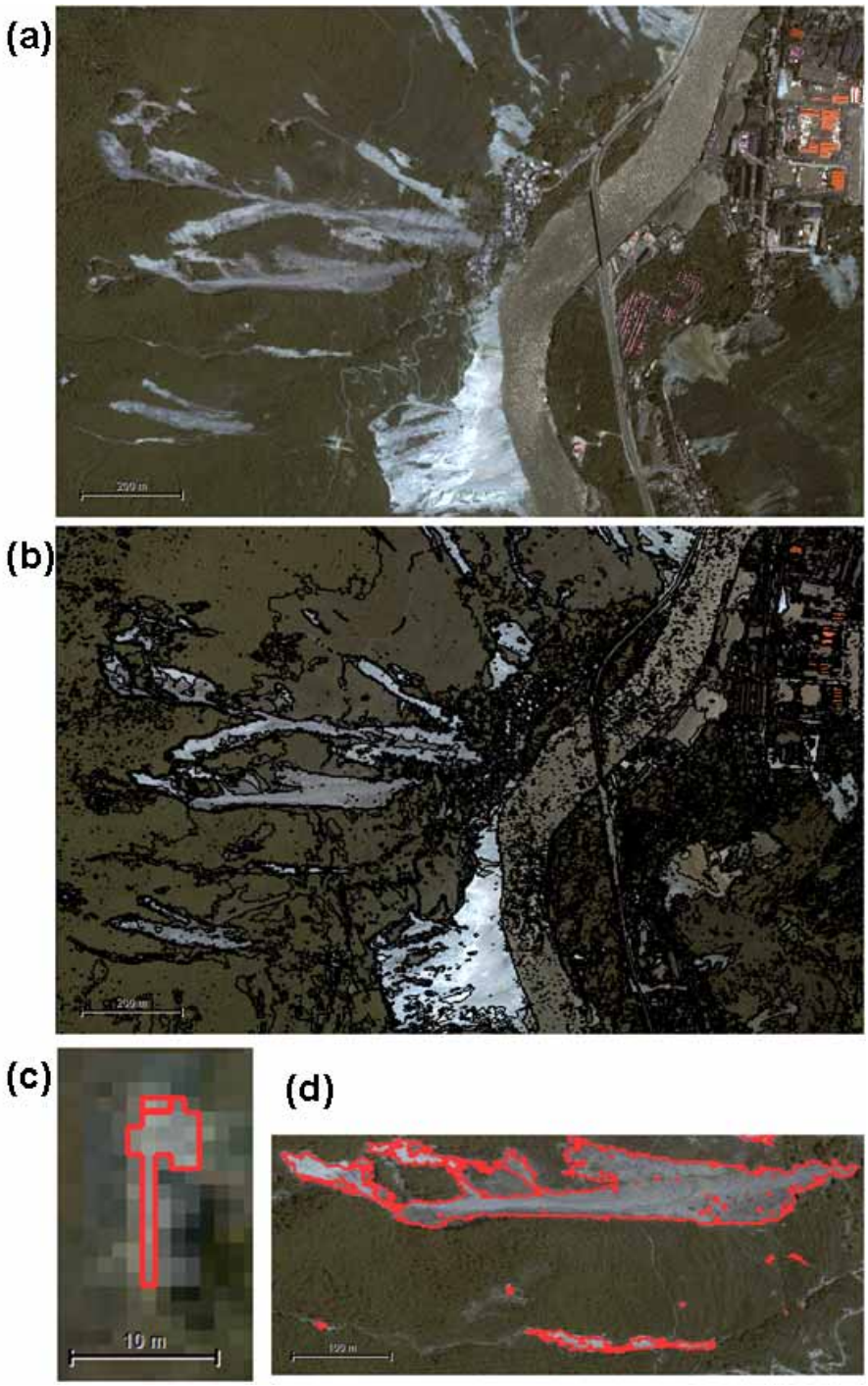

Figure 6.1: The performance of segmentation optimization procedure (SOP) without any modification in IKONOS image of Wenchuan, China: (a) the IKONOS imagery (3-2-1), (b) the result of image segmentation using SOP, (c) a detailed view of segmentation for a small landslide, (d) a detailed zoom of segmentation for a large landslide.

principle inside SOP. Since SOP is processed on multi-spectral NIR and red bands, a minimum requirement should be that the image contains these two bands.

For images with similar multi-spectral bands and spatial resolution, such as IKONOS imagery, the SOP approach can be directly used without any change. One example of applying SOP in IKONOS is presented in figure 6.1. The coverage area is in Wenchuan, China, which contains totally different geological and morphological settings from Messina. The SOP algorithm was directly used for this image segmentation without any change. The result indicates the good performance also on this IKONOS image from a different area. It shows that both small (figure 6.1(c)) and large landslide (figure 6.1(d)) can be well segmented.

For the imagery with lower spatial resolution, although the over- and under-segmentation can be to some extent reduced with this fully automatic SOP approach, in order to get the optimum segmentation, it is suggested to include other segmentation participation. Figure 6.2 shows the application of SOP in 10m ALOS AVNIR multi-spectral bands for segmentation. It is indicated in figure 6.2(a) that by directly applying SOP without modification, over-segmentation can be reduced, but slightly. As illustrated in figure 6.2(b), in order to get an improved segmentation, it is better to include a spectral difference segmentation [Definiens, 2010], with given multi-resolution scale of 7 and spectral difference scale of 11. However, this requires an intensive manual participation for a selection of optimal scale.

Therefore, it can be concluded the developed SOP is problem-specified: for the purpose of reducing over- and under-segmentation during the segmentation of landslide objects. The approach is working well for the imagery with similar spatial and spectral resolution. The segmentation algorithm is possible to be fully

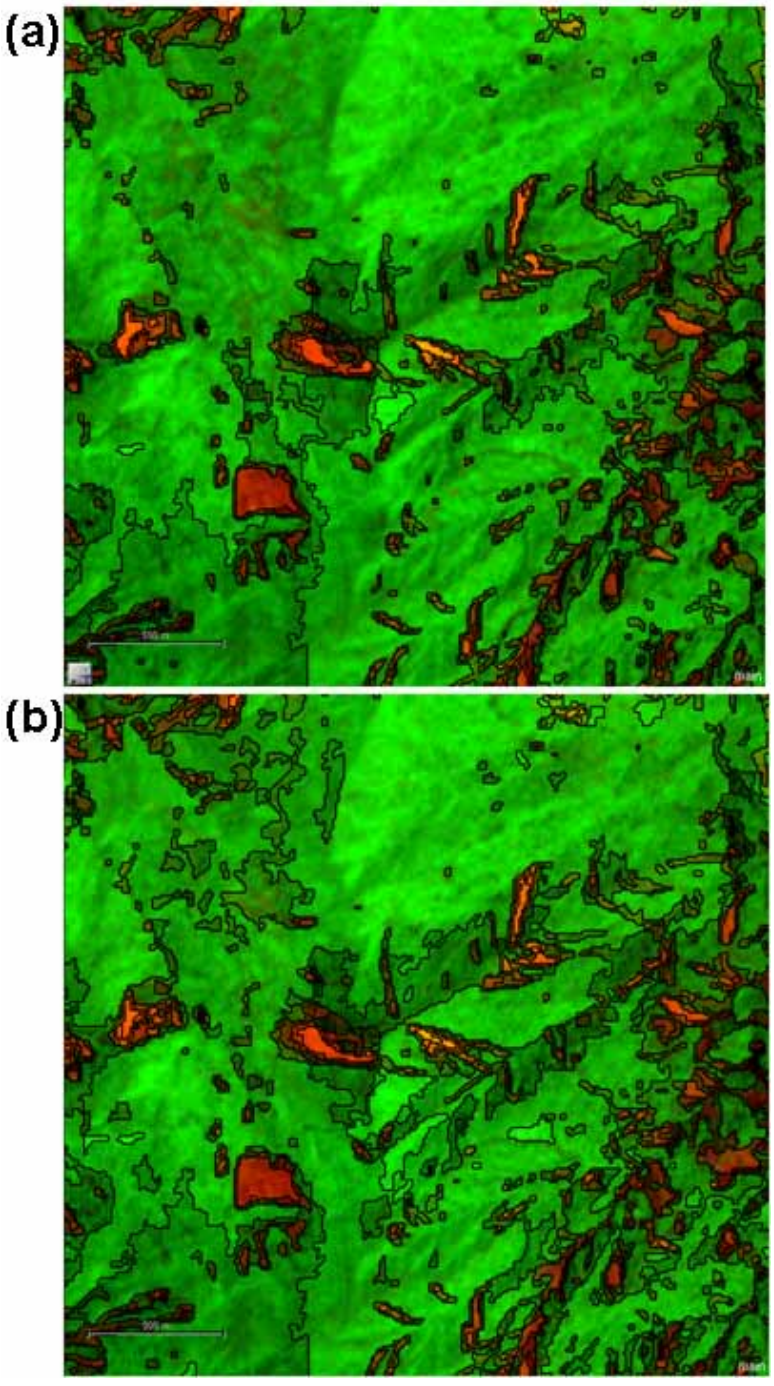

Figure 6.2: The performance of segmentation optimization procedure (SOP) in 10m ALOS AVHIR imagery in Wenchuan China for all multi-spectral bands (landslides in brown) using: (a) fully automatic approach; (b) the involvement of spectral difference segmentation with manual participation.

automatically used to get the good segmentation. However, the performance of SOP might be decreased for image with lower resolution. In this case, although the under- and over-segmentation is possibly to be reduced, it is better to involve other approaches for a further improvement in image segmentation.

6.1.2 Principal component analysis (PCA) for change detection

In this study, the change detection was performed based on principal component analysis (PCA). The principle of change detection using PCA is based on the transformation of multi-spectral images before and after the change into a different intensity space: the principal component images in relation to large eigenvalues are considered the unchanged part of the images, and minor component images refereing to smaller eigenvalues to changed parts of the images [Radke et al., 2005]. In particular, the 4th principal component was used for the detection of 'change' component, based on the membership function calculated from 10 selected samples. The approach of employing the 4th principal component is working well in the case study of Messina. However, the question is, considering that PCA is content specified, is the selection of the 4th principal component useful for its generic use of change detection?

This has been discussed by previous publications (e.g. Jensen [1996]; Niemeyer et al. [1999]; Radke et al. [2005]) that it is difficult to underhand which component can represent change without a visual interpretation of PCA components. It is mentioned by Gong [1993] that changed regions can be detected from the first or second principal components, however this is not justified in our study.

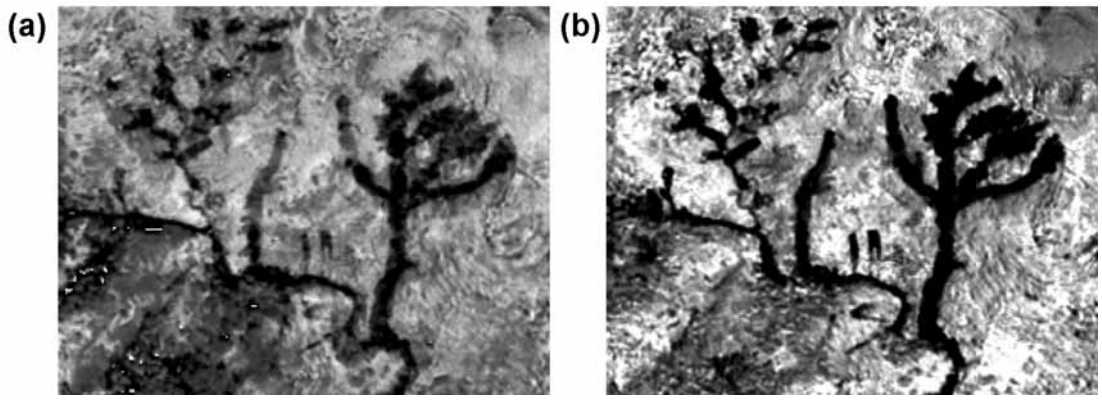

Figure 6.3: The performance of change detection using: (a) subtractive NDVI and (b) PCA.

Nevertheless, it can be generally agreed that the PCA is a generic feature for change detection, although a training area is preferred to be defined in OOA so as to identify the appropriate component and threshold. It is in so far generic as that the PCA can accommodate information from any kind of sensor.

Compared to other change detection approaches, PCA has several advantages especially useful for OOA. The importance of normalized difference vegetation index (NDVI) for landslide detection is emphasized in several literatures [Lin et al., 2004, 2005, 2006; Rau et al., 2007]. Thus, change detection for landslide mapping is possibly performed with subtractive differencing of NDVI. However, the derived subtractive image is not suitable for analysis at the object level because the pixel values for an object are not always uniform, thus tending to be very 'noisy'. Instead, PCA-based 'change' component minimizes these kind of noises because the calculation is based on the intensity space for image transformation. Therefore, for previous principal components, less noises are contained because they are transformed into last components. An example of comparing subtractive

NDVI and PCA is displayed in figure 6.3 for a zoom of debris flows in Messina.

Similar to PCA, there is another image transform approach of Minimum Noise Fraction (MNF, figure 6.4). MNF employs an approach of transformation similar to PCA however it considers noise fraction which is defined as the ratio of the noise variance to total variance for each band [Green et al., 1988]. MNF actually includes two cascaded steps of PCA [Phillips et al., 2009; Sesnie et al., 2008; Wu and Murray, 2003]. First step, aiming at separating noises from signals, employs a PCA transformation with a calculation of noise covariance matrix and subsequent processing of noise decorrelating and rescaling. Second step is a noise-adjusted PCA which is carried out using standard transformation on previous derived noise-whitened data.

Although MNF has been reported as an advantage of reducing signal to noise ratio (SNR) in the process of data transformation [Phillips et al., 2009; Wu and Murray, 2003], it shows some limitations in OOA change detection. Firstly, in terms of change detection, the output of PCA is aligned by the variance of each component with the increasing order of components. MNF however is more focusing on reducing noises level of all 8 input layers, thus ordering the transformed components as decreasing image quality instead of maximum component variance. As a result, change information contained within these reduced 'noises' is accordingly removed or transformed to higher order components but containing more noises. In the case of Messina, the change component would chosen as 5th component. The 4th contains very less information about the change of landslides (referring to figure 6.4). Secondly, due to the minimization of SNR, MNF renders lower variance between 'change' and 'non-change' objects inside the minor component. Therefore, with lower data variability, it renders the difficulty in

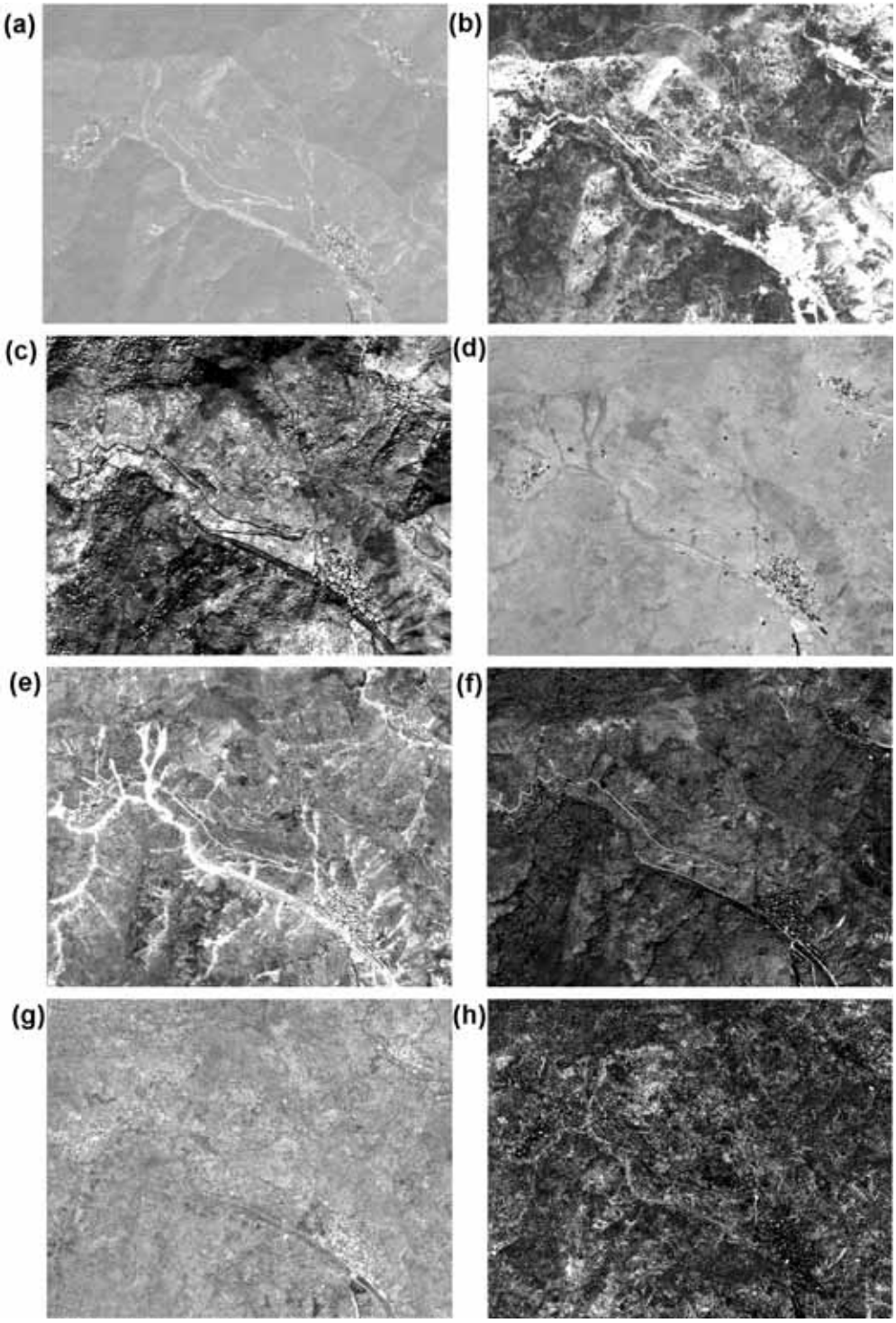

Figure 6.4: The change detection using Minimum Noise Fraction (MNF): (a)-(h) the 1st to 8th transformed components.

selecting representative samples and generating corresponding membership function for landslide objects, thus introducing another error source of classifying landslide candidate objects.

6.1.3 GLCM mean from DTM

In order to perform a textural analysis of landslide candidate objects, in this study the gray-level co-occurrence matrix (GLCM) mean was calculated based on the GLCM (i, j), with a consideration of neighboring pixels in all directions (0°, 45°, 90°, 135°) , written as:

$$m = \sum_{i,j=0}^{N-1} i(P_{i,j}) \times 100 \tag{6.1}$$

or alternatively written as:

$$m = \sum_{i,j=0}^{N-1} j(P_{i,j}) \times 100 \tag{6.2}$$

where $P_{i,j}$ is the normalized value of cell (i, j) in GLCM of DTM. N is the column or row number of GLCM. Both two equations can be used for the calculation, considering that the GLCM is symmetrical, namely $i = j$.

The purpose of GLCM mean is to remove false positives with low-frequency elevation variation whose GLCM mean values are lower than objects with high-frequency elevation variation. For instance, an object with no elevation variation, namely flat and obviously not landslides because of no elevation changes, has a GLCM mean value of 100, according to the definition of GLCM mean mentioned above. In this study, the threshold to remove these false positives of low-frequency

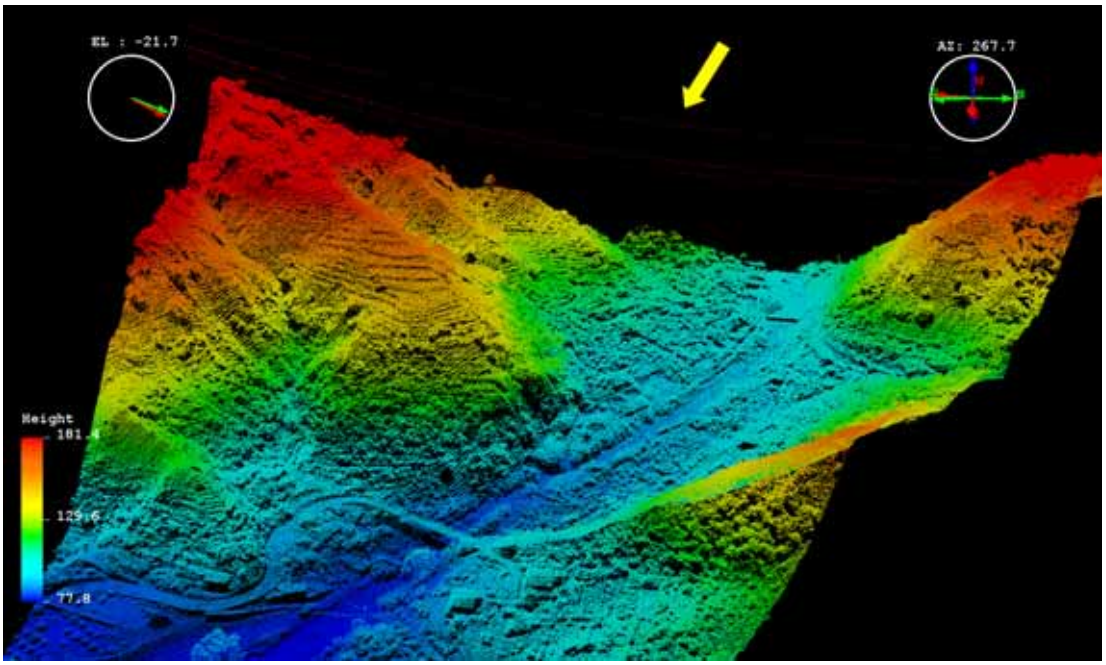

Figure 6.5: A 3D view of raw LiDAR points in the study area. The raw data suffers the problem of a bunch of off-terrain points such as those high-voltage lines in the sky (yellow arrow).

elevation variation was set as GLCM mean < 126.7.

The usefulness of this GLCM mean estimation is dependent on the quality of DTM. A DTM with rough resolution might decrease the utility of this approach, although it should also dependent on the dimension of landslides and the scale of landslide mapping. For this reason, a 1m resolution LiDAR DTM was preferred to be utilized in our study.

Future improvements for GLCM mean using LiDAR DTM should involve an inclusion of robust pre-filtering of LiDAR point clouds, for the purpose of eliminating off-terrain points, such as trees, houses and other disturbing objects (e.g. figure 6.5). A promising method is hierarchical robust interpolation (HRI, Briese et al. [2002]; Pfeifer et al. [2001]), embedded in SCOP++ software environment.

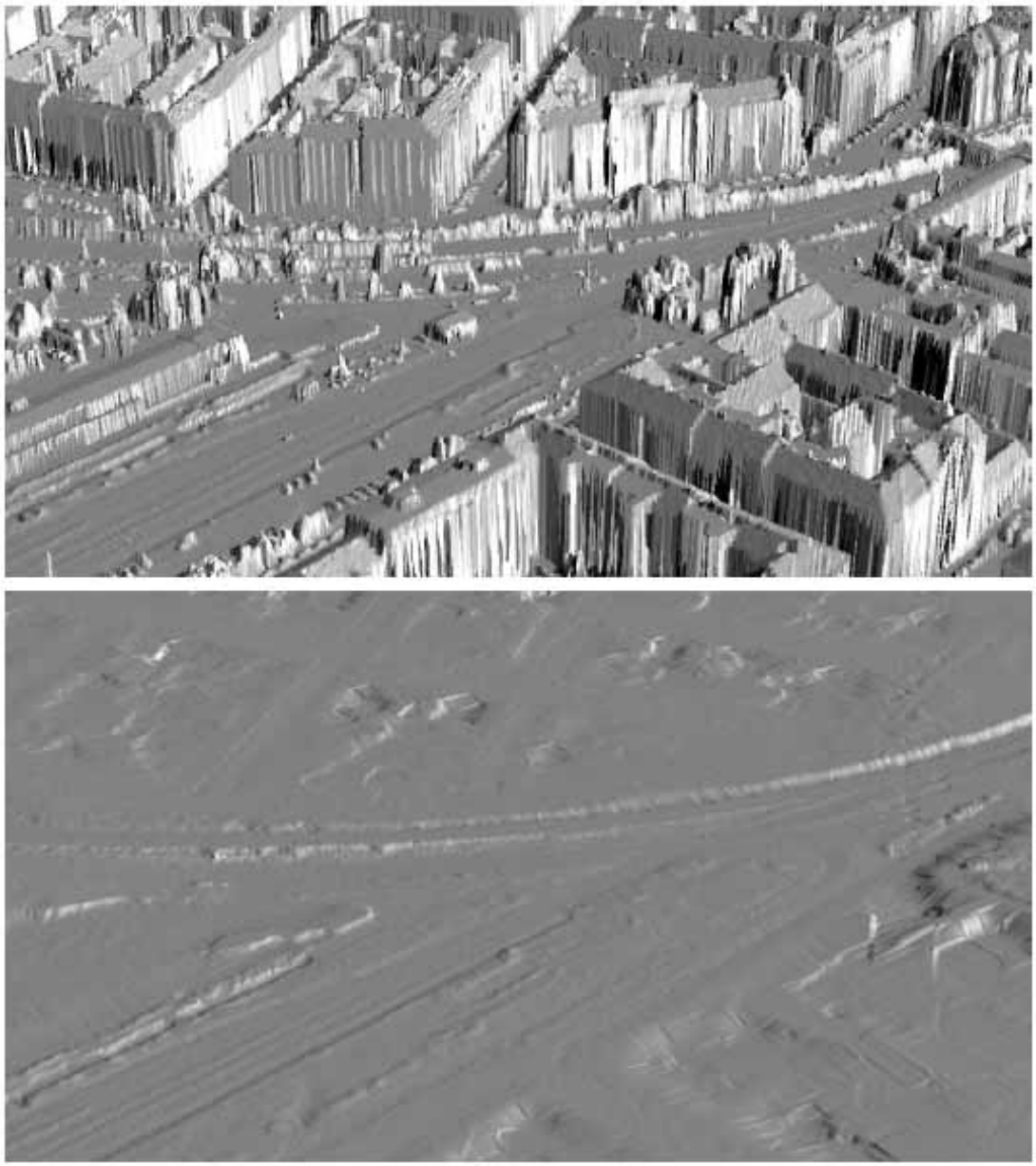

Figure 6.6: An example of DTM before (up) and after (bottom) hierarchical robust interpolation. This method enables a removal of off-ground targets from the ground surface. The example was used from Briese et al. [2002].

HRI allows an automatic generation of DTM from irregular distributed LiDAR point clouds, with off-terrain points eliminated and error reduced, such as the example illustrated in figure 6.6. Moreover, Razak et al. [in press] have developed a 'landslide filter' which is especially developed for automatic bare-earth extraction filtered from LiDAR point clouds for the purpose of landslide visualization. With an integration of these described methods, the textural analysis using GLCM mean can be effectively performed on the elevation data for a detection of landslide candidate objects.

6.2 PSI-HCA for landslide detection

6.2.1 Reference point

The reference point, the conventional stable point against which all other PSI displacements are measured, is very important for multi-interferometric processing and it should be carefully chosen. A high quality reference point is selected based on radar phase stability. Reference point has preferentially to be selected in the middle of a scene because the precision of the velocity estimation decreases with the increased distance to the reference point itself, due to an increment of relative atmospheric disturbance signals [Motagh et al., 2007]. Also, the height of the reference point should be accurately defined because its accuracy influences directly the uncertainty of PS location. In addition, since the reference point is considered as motionless, it should be selected in a stable area. In case of complicated regional settings areas, a set of locally stable reference points can be separately chosen in order to overcome the difficulty in unwrapping the entire

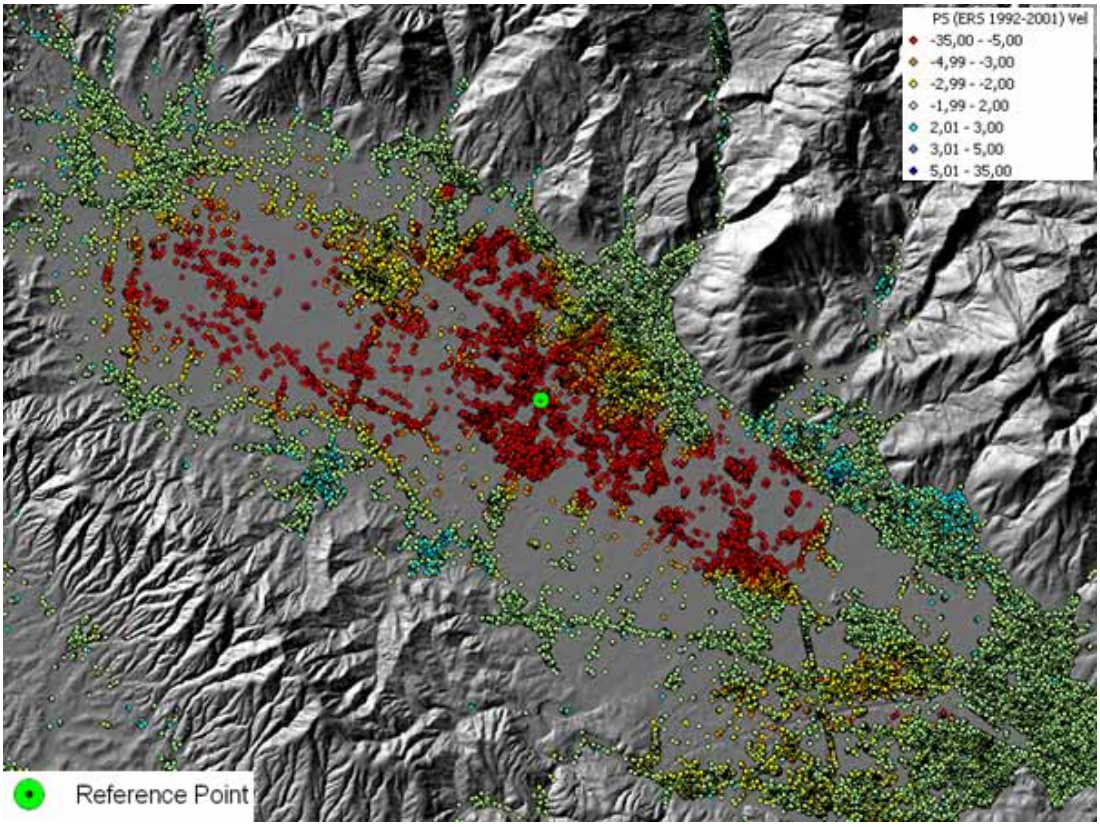

Figure 6.7: An example of selecting reference point in unstable area in Pistoia-Prato-Firenze basin.

scene using only a single reference point [Parcharidis et al., 2009]. In all, the selection of a reference is crucial for accurate PSI processing, considering that all rates and time series of PS are determined through this choice.

Figure 6.7 shows an example of a badly-chosen reference point. In this case, the reference point is selected in the unstable area of the Pistoia-Prato-Firenze basin which has long-term problems of subsidence. As a result, the derived PS data from this reference point is biased (figure 6.8). Due to the fact that this reference point is not motionless, these derived PS datasets show that the subsidence region is stable. This example illustrates how important a careful selection

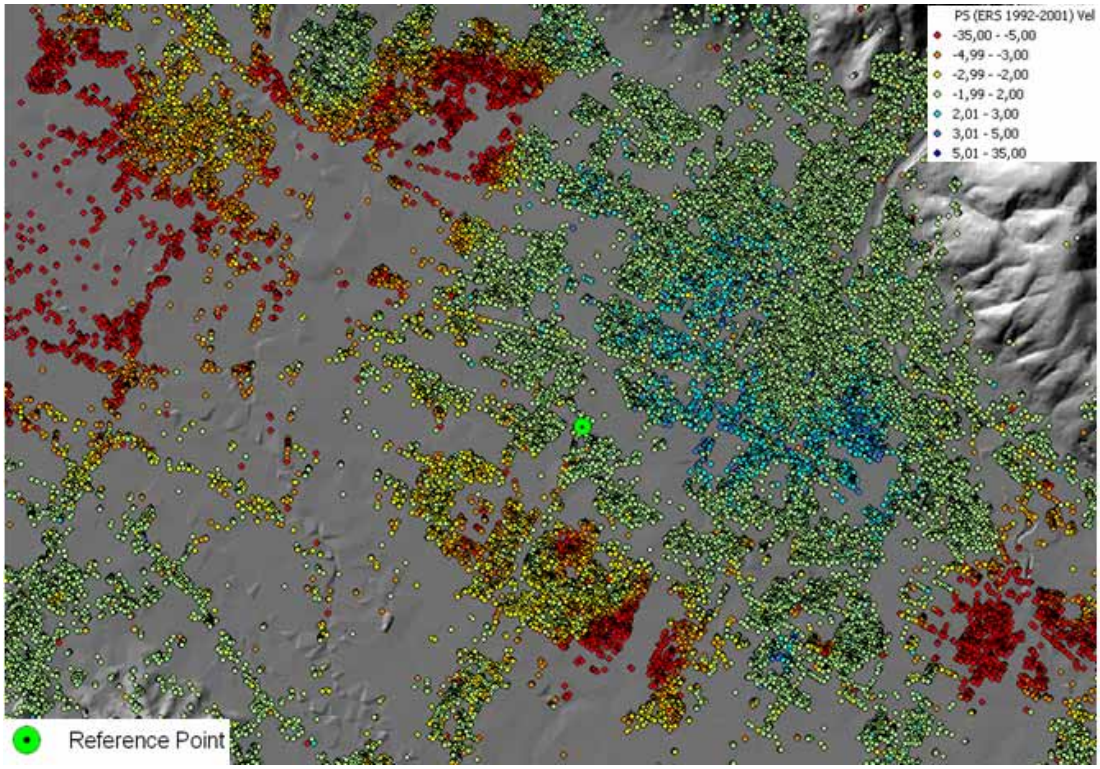

Figure 6.8: The derived PS result from the reference point in figure 6.7

of PS reference point is.

PSI-HCA nevertheless decreases the dependence on the reference point, thus reducing the effect of badly-chosen reference point. This is because the fundamental part of this approach is the Getis-Ord G_i^* statistic which compares weighted local averages to global averages for hotspot detection [Getis and Ord, 1992, 1996; Ord and Getis, 1995]. The hotspot is defined as a geographical area where there is a statistically significant level of PS clustering with high velocities. It means that the approach estimates whether local high positive values or low negative values tend to be clustered, with consideration of global PS dataset. Thus, PSI-HCA is an approach of relative computation. Since PS velocity is also a relative

estimation with respect to the velocity of a reference point, the hotspot analysis is less dependent on the stability of reference point. The high positive velocity PS will be clustered as a hotspot with high positive G_i^* values whereas the low negative velocity PS will be clustered as a hotspot with low negative G_i^* values. However, the usefulness of G_i^* statistic does not decrease the importance of choosing reference point with good quality. The difficulties in atmosphere disturbances, location uncertainty and regional settings mentioned above cannot really be smoothed using the spatial statistics analysis. To obtain a high quality PSI measure, a great care about the selection of suitable reference point should be taken during the processing.

6.2.2 PS density

The PS density determines the usefulness of PSI-HCA in landslide detection. Current difficulty of PSI-HCA is that the density of PS in hilly and mountainous areas can not always be ensured. This is because of lacking stable reflectors in rural areas. The case study of the Arno river basin can be properly carried out because the area is highly urbanized, thereby rendering PS density of 31 PS/km^2 for ascending data and 32 PS/km^2 for descending data even after the masking of flat urbanized areas. Nonetheless, how to improve PS density in mountainous areas without stable reflectors remains a critical concern for PSI-HCA and current advances in the research of long-term InSAR makes this improvement promising.

Firstly, the new generation of high resolution SAR images with short wavelength of X-band (e.g. COSMO-SkyMed and TerraSAR-X) enables a huge improvement in PS density. figure 6.9 indicates ca. 10 times improvement in PS

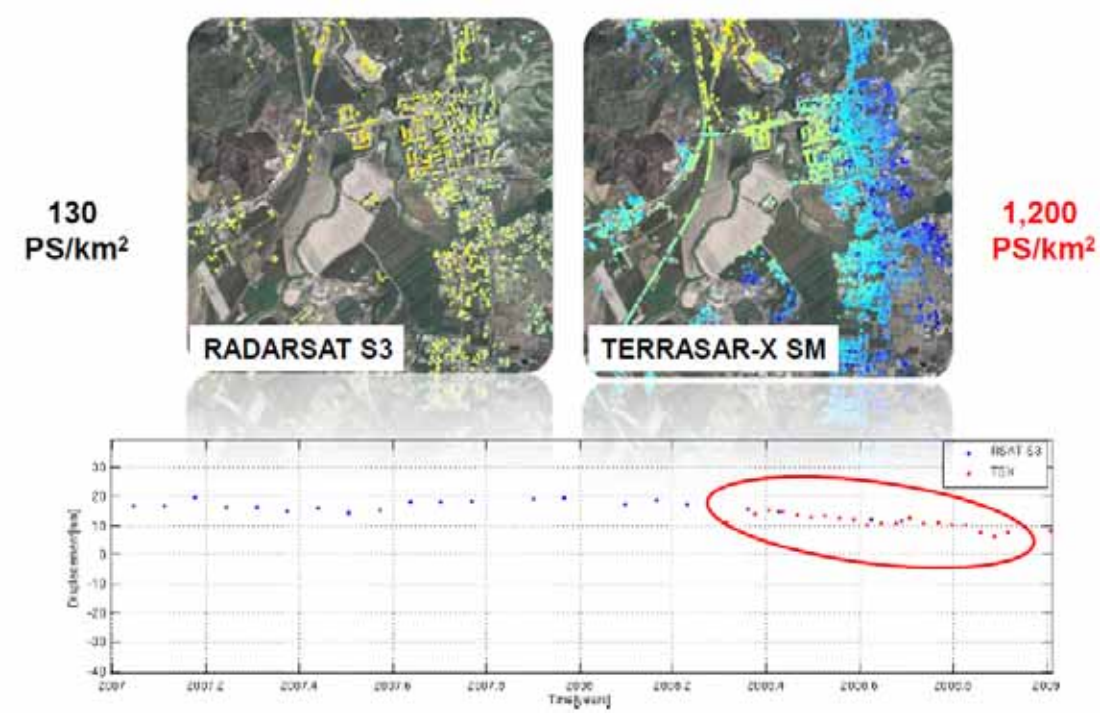

Figure 6.9: A comparison of PS density between C-band (RADARSAT) and X-band (TerraSAR-X) data. The image is acquired from Ferretti et al. [2010].

density of X-band TerraSAR-X data over C-band RADARSAT data [Ferretti et al., 2010]. Moreover, Crosetto et al. [2010] performed a comparison of PS density between C-band and X-band data in the city of Barcelona: the density of PS derived from X-band TerraSAR-X images is ca. 40 times of that from C-band ERS-1/2 and Envisat images. The high density of PS reached by X-band TerraSAR-X images even allows a 3D distribution of PS over the structure, as illustrated in figure 6.10.

In addition, several efforts have shown the possibility of increasing PS density through the processing technique improvement, such as the $SqueeSAR^{TM}$ technique developed by [Novali et al., 2009] which performs a filtering over ho-

Figure 6.10: The high density PS derived from high resolution X-band SAR images enables a 3D distribution over structures (Barcelona, Spain) [Crosetto et al., 2010].

mogeneous areas to enhance SNR. The $SqueeSAR^{TM}$ technique is on the basis of accurate coherence matrix estimation which compares adjacent pixels with the Kolmogorov-Smirnov test, so as to derive 'squeezed' parameters of InSAR. Figure 6.11 shows how the utilization of $SqueeSAR^{TM}$ contributes to the increasing density of PS data.

In all, the usefulness of PSI-HCA can be largely increased with the development of new X-band SAR satellite platforms and the improvement of data

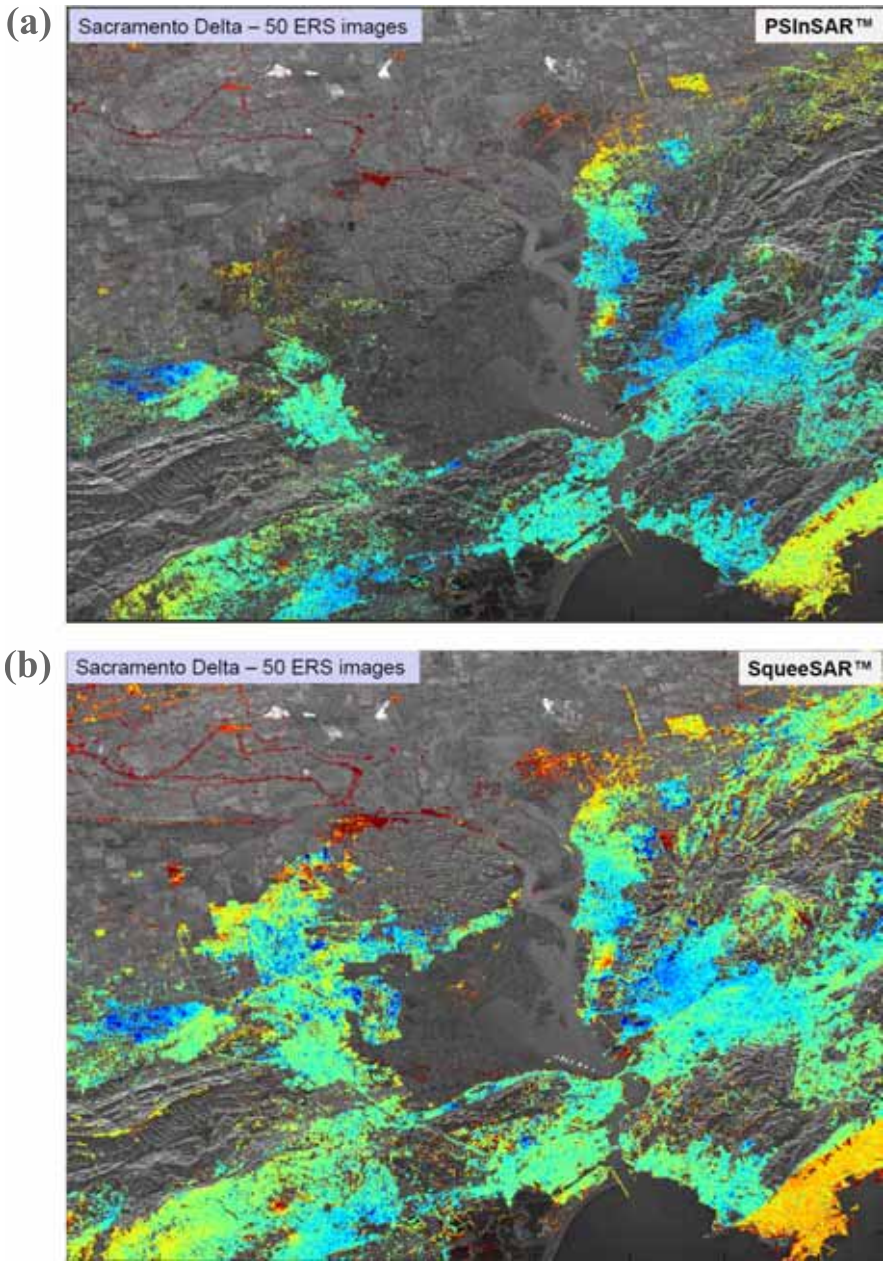

Figure 6.11: A comparison between $PSInSAR^{TM}$ and $SqueeSAR^{TM}$ shows an increasing point density for the latter, especially in the non-urban areas [Novali et al., 2009].

processing technique to extract the stable benchmarks.

6.3 PSI hue and saturation representation

6.3.1 Concept

PS are usually integrated in a geographic information system (GIS) as a standard point-based map, using color coding on their velocities. However, for this representation, the measurement of displacements is always along LOS, with an incidence angle of 37° for RADARSAT PS used in this study. Moreover, PS data has to be displayed with a separation of ascending and descending data (e.g. figure 6.12), such as the RADARSAT dataset in this study for PSI-HCA approach.

Here the PSI-HSR (PSI Hue-Saturation Representation), a new method for representing PSI point targets using the hue-saturation scale, is introduced. The aim was to render a unique color for each PSI point target, based on a combination of displacements assessed along two different lines of sight. PSI-HSR provides a straightforward way to describe ground movement. To demonstrate the usefulness of this approach, an example of detecting ground subsidence in the Pistoia-Prato-Firenze basin is presented. PSI-HSR has several advantages:

1. It synthesizes the displacement vectors from both ascending and descending orbits.

2. It provides a way to display both PS velocity and PS moving direction on an East-West-Zenith-Nadir plane, within a standard point-based map containing numerical information on hue and saturation.

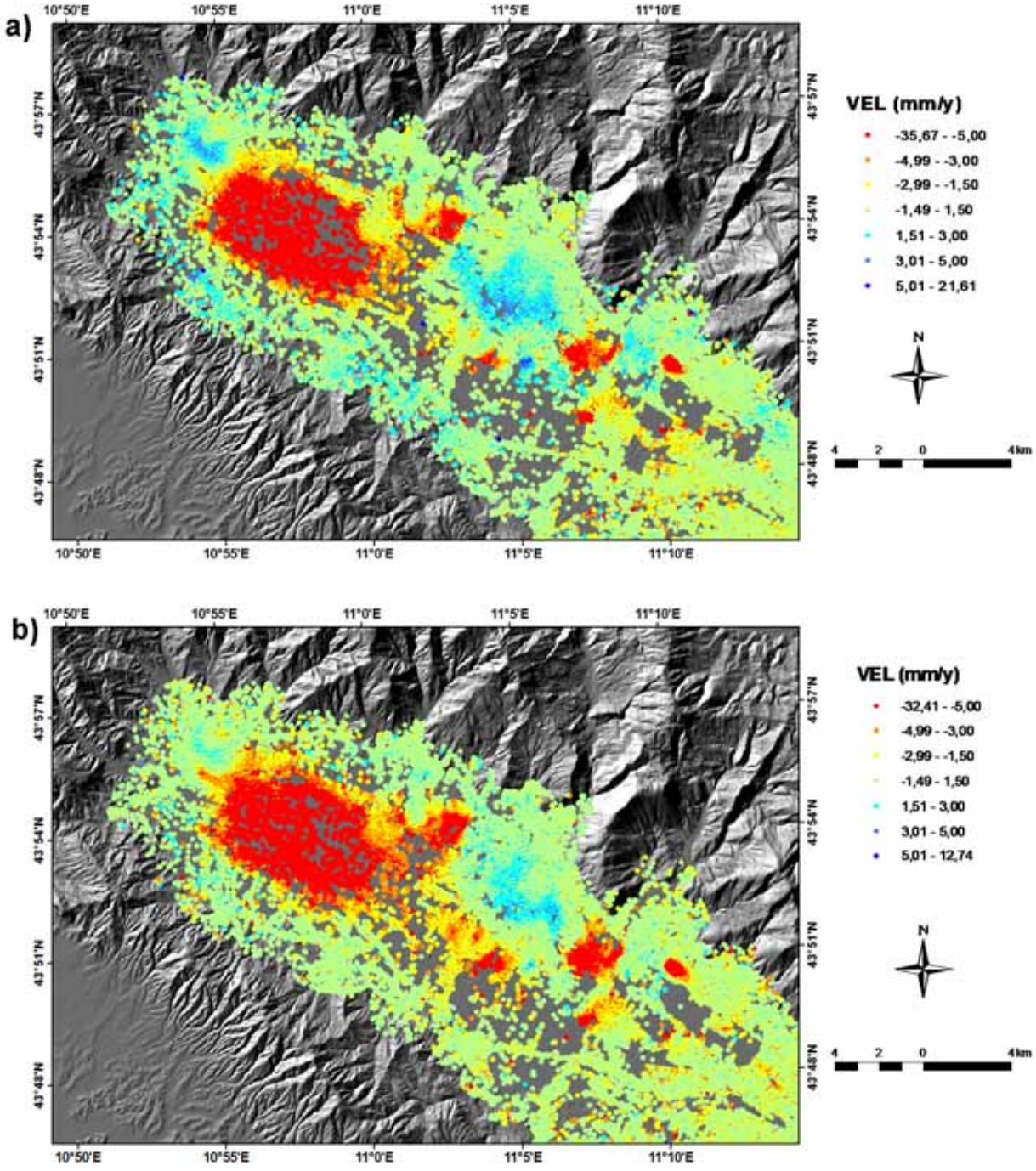

Figure 6.12: The Pistoia-Prato-Firenze basin: a PS (RADARSAT, 2003 to 2006) point-based map described by a color ramp on velocity, with the separation of (a) ascending and (b) descending data.

3. The PS velocity is calculated not only along the line-of-sight (LOS) but also ranging from 0° to 360°.

4. It offers the possibility to combine PS from different orbits and satellites together.

5. It provides a clearer and more straightforward visualization of ground movements.

6.3.2 Test area and data used

The Pistoia-Prato-Firenze basin in central Italy was selected as the test area. As a result of intensive groundwater withdrawal in past decades, the area is suffering from intense subsidence, with the monitored deformation rate reaching 30 mm/year during the period from 1992 to 2001 [Canuti et al., 2005, 2006]. PSI-HSR was applied in this area so as to confirm the existing subsidence. Meanwhile, the previous mapping results can be an alternative way to validate the usefulness of PSI-HSR.

In this study both ascending and descending PS derived from 48 RADARSAT images (from 2003 to 2006) were available for the basin. Because of urbanization, the PS density has reached 281 PS km^2 for descending data and 288 PS km^2 for the ascending orbit. The data were processed by Tele-Rilevamento Europa (TRE) using the PSInSAR technique on behalf of the Arno River Basin Authority.

6.3.3 Methodology

PSI-HSR introduces two new ideas: (1) the use of the hue-saturation color scheme and (2) the synthesis of ascending and descending components.

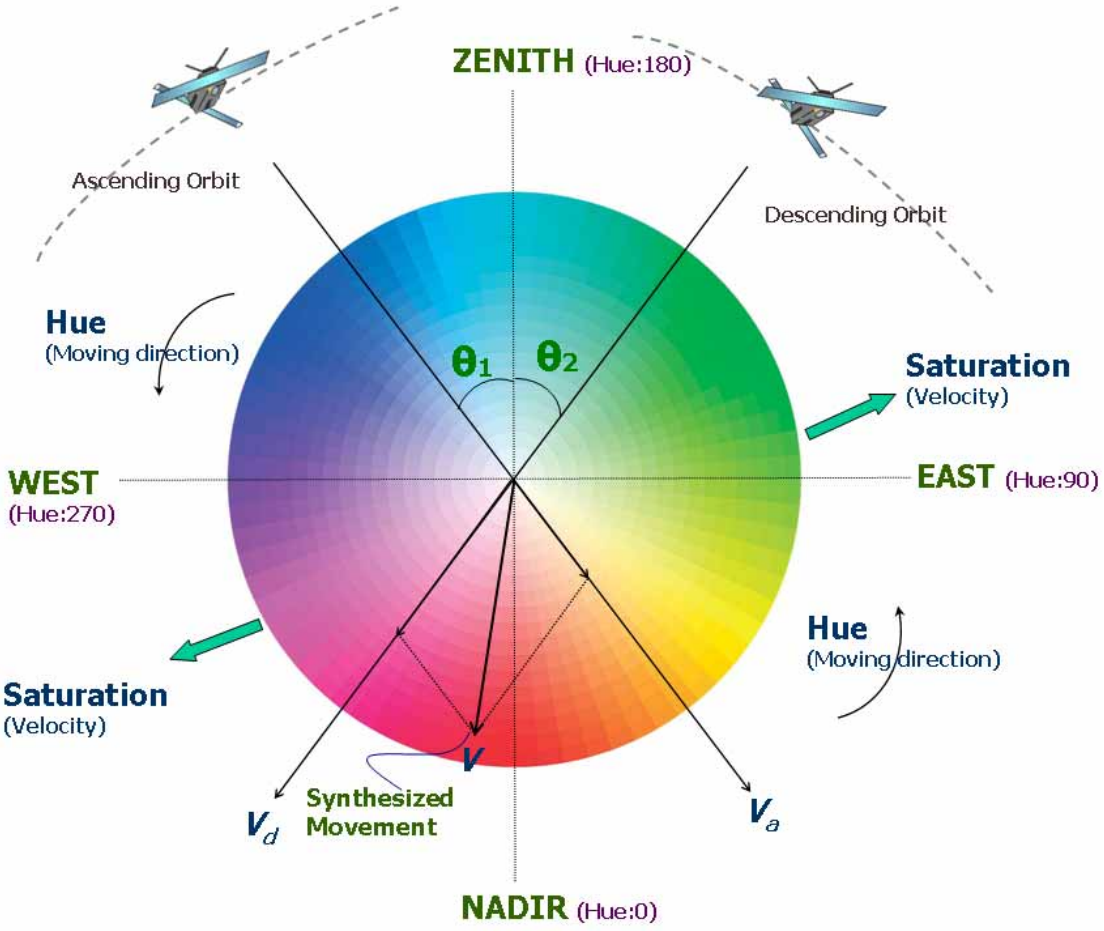

Figure 6.13: The hue-saturation wheel plotted on the East-West-Zenith-Nadir acquisition geometry. The moving direction of a displacement vector is represented by a hue value ranging between 0° to 360°, with 0° starting from the nadir. The displacement rate is represented by a saturation value ranging from 0 to 100. This representation is suitable for a synthesized displacement $\mathbf{V}$, which is the addition of ascending ($\mathbf{V_a}$) and descending ($\mathbf{V_d}$) displacement components. $\theta 1$ and $\theta 2$ refer to the incidence angles of the ascending and descending orbit, respectively.

The color scheme of HSI (hue, saturation and intensity) is applied in PSI-HSR. The idea is to allocate a unique color to each PSI point target with a different displacement rate and moving direction. The intensity value is assigned to a constant value, in this study with a maximum value of 100. The hue-saturation wheel is used and integrated in the acquisition geometry of the East-West-Zenith-Nadir, covering both ascending and descending displacement components (figure 6.13). The moving direction is represented by the hue value, which ranges from 0° to 360°, and the moving velocity is interpreted by the saturation value, ranging from 0 to 100. Using this color scheme, both displacement rate and moving direction can be displayed in a single standard point-based map.

For the traditional method, as illustrated in figure 6.12, the displacement rates of each single PSI point target are only calculated along the line-of-sight (LOS). Inspired by the flexible representation of the moving direction in the hue-saturation wheel, the concept of a synthesized displacement is introduced (figure 6.13). In the satellite acquisition geometry, a synthesized displacement $\mathbf{V}$ is the addition of ascending component $\mathbf{V_a}$ and descending component $\mathbf{V_d}$. As a result, each single synthesized displacement $\mathbf{V}$ combines PS information provided by both ascending and descending orbits, with a synthesized moving direction ranging between 0° and 360°. In the test area of Pistoia-Prato-Firenze basin, an array of synthesized points is created, with a spatial interval of 100m, which is the average autocorrelation distance measured in PS velocity. For each single point, $\mathbf{V_a}$ and $\mathbf{V_d}$ are respectively calculated based on the average value of neighboring ascending and descending PS, with a Euclidean searching distance of 100m. Its synthesized displacement $\mathbf{V}$ is calculated as the vector sum of $\mathbf{V_a}$ and $\mathbf{V_d}$, represented by the hue-saturation wheel indicated in figure 6.13.

6.3.4 Result interpolation

Compared to the traditional map (figure 6.12), PSI-HSR outputs (figures 6.14 and 6.15) overcome the limitation that ground displacements are only measured along the LOS. A movement within an East-West-Zenith-Nadir plane can be described flexibly, without the separation of the ascending and descending maps. Thus, PSI-HSR enables a spatially detailed mapping of ground deformation and uplift in the Pistoia-Prato-Firenze basin. In figure 6.14, the saturation stands for the logarithm of the moving velocity. A velocity smaller than 1 mm/year is classified as zero saturation because it refers to a stable condition. In figure 6.15, for an easier visualization, the color wheel is divided into 61 classes, according to different moving directions and displacement rates. Both figures 6.14 and 6.15 confirm the different spatial patterns of terrain subsidence in several industrial areas investigated by Canuti et al. [2005, 2006]; Colombo et al. [2003]; Raucoules et al. [2002]. The subsidence boundary and zonation can be clearly mapped, based on a homogeneous transition in the hue-saturation color wheel (in the map from yellow in the west to magenta in the east). Figure 6.14 shows the ground movement more continuously than figure 6.15 because of the detailed definition in its legend. However, the legend of figure 6.15 provides the alternative of an easier interpretation on moving velocities, with a monitored deformation up to 40 mm/year. Other than subsidence, some uplift motions (areas shown by a blue color) can be clearly observed using the PSI-HSR approach. Future improvements should involve some field data measured from Observation Stations in the study area.

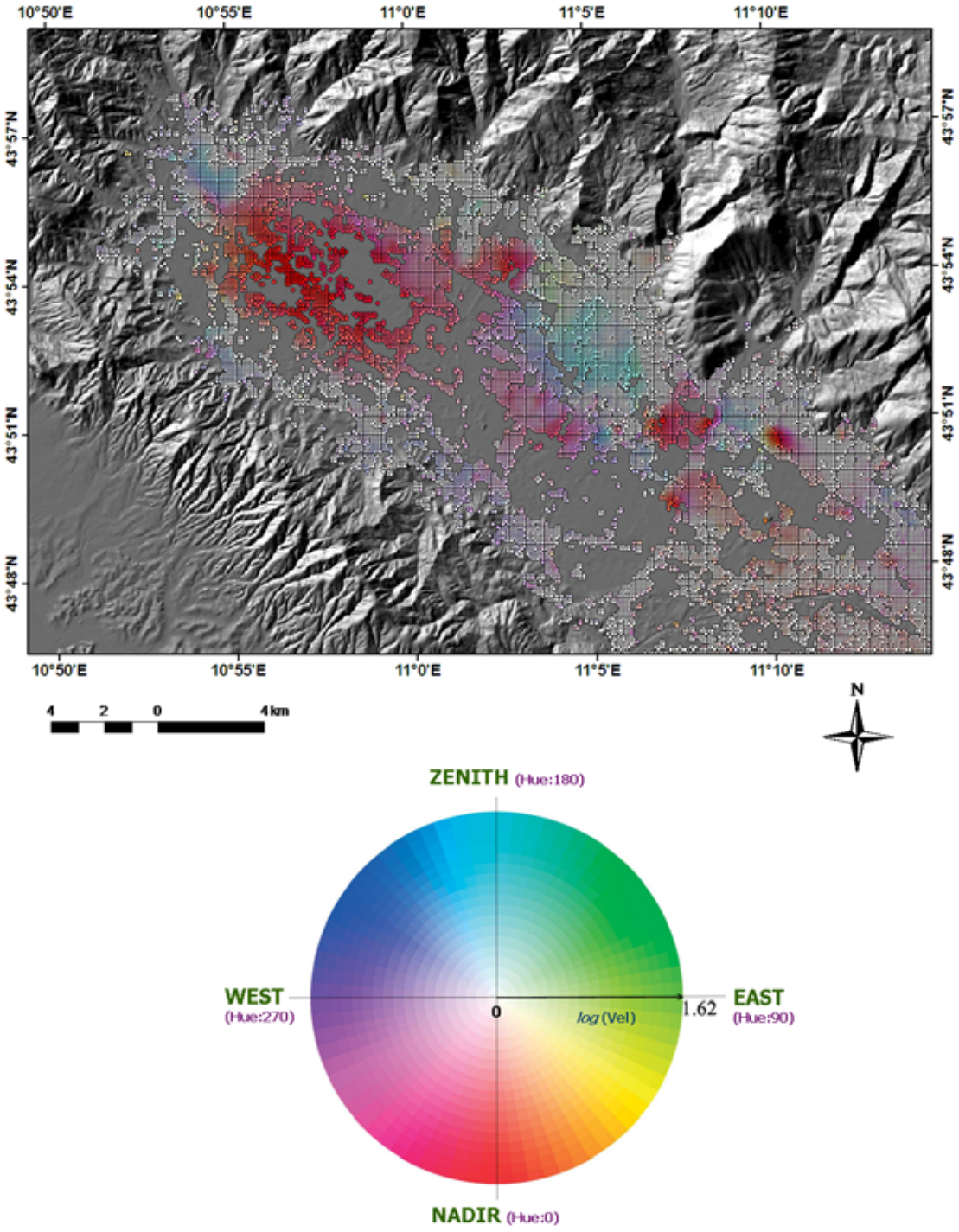

Figure 6.14: The subsidence and uplift in the Pistoia-Prato-Firenze basin, displayed by synthesized PS using PSI-HSR. Each point contains numerical information of hue and saturation values, and it can be located on the hue-saturation wheel. The saturation stands for the logarithm of velocity. Velocities < 1 mm/year are classified as zero saturation.

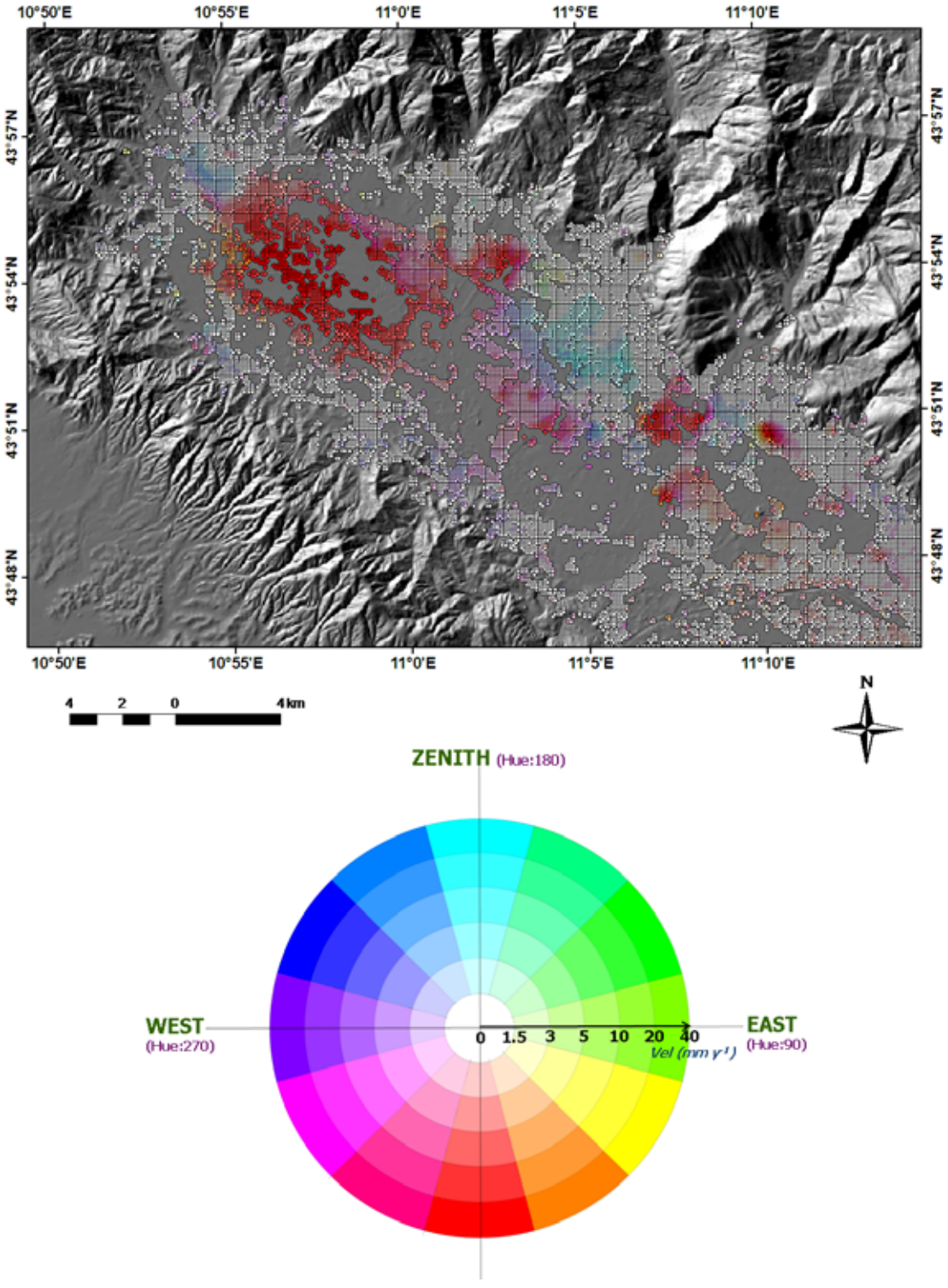

Figure 6.15: The subsidence and uplift in the Pistoia-Prato-Firenze basin, detected by synthesized PS using PSI-HSR. The color wheel is divided into 61 classes according to different moving directions and displacement rates.

6.3.5 PSI-HSR for landslide studies

The Pistoia-Prato-Firenze basin is suitable for PSI-HSR. The high density of PS is ensured by a large number of stable reflectors such as buildings and infrastructures. However, for landslide studies, the area with low-density PS can limit the usefulness of PSI-HSR because of insufficient points for calculating the synthesized vectors. The C-band RADARSAT PS employed in this study is still not sufficient for a representation using PSI-HSR to characterize spatial and geomorphometric properties of landslides. Nevertheless, the approach is promising for the near future, especially with the rapid development of a new generation of X-band satellites such as COSMO-SkyMed and TerraSAR-X, which can greatly increase the PS density because of an improvement in resolution [Bamler et al., 2006]. Also, the utilization of $SqueeSAR^{TM}$ technique mentioned by [Novali et al., 2009] can largely increase the density of scatterers. In addition, with the concept of synthesized PS, it is possible to integrate ascending and descending data acquired from different sensors, with known incidence angles. Thus, PSI-HSR provides the possibility of displaying PSI outputs from different satellites in the same point-based map. Therefore, the application of PSI-HSR in landslide studies is very promising.

6.4 Landslide risk mapping from PSI-HCA

In chapter 5, a new approach for quantitative landslide hazard and risk assessment was developed, using the long-term InSAR derivative of landslide hotspot map as the input. In the case study of the Arno river basin, approximately 0.54, 1.14, 1.86, 2.72 and 3.22 billion euro losses were estimated from slow-moving landslides

within the detection precision of PSI technique, for the upcoming 2, 5, 10, 20 and 30 years, respectively.

The uncertainty of this approach for landslide risk assessment results from the detection error of PSI-HCA. As mentioned in chapter 4, although the flat areas in the Arno river basin were masked and the analysis was exclusively performed in the mountainous and hilly areas, the usefulness of PSI-HCA can be decreased due to the existence of other geophysical processes which can be detection by PSI technique. For example, red hotspots indicating moving direction away from LOS can be recognized as ground motions due to subsidence [Canuti et al., 2007; Ferretti et al., 2000; Massonet et al., 1997], sinkholes [Al-Fares, 2005; Ferretti et al., 2004], building consolidation [Stramondo et al., 2008], erosion [Smith, 2002], tectonics [Buergmann et al., 2006; Colesanti et al., 2003; Massonet et al., 1994; Vilardo et al., 2009] and underground works related to tunnelling or mining activities [Perski, 1998]. In addition, blue hotspots suggesting moving direction towards LOS can be associated with ground movement because of uplift due to fluid injection [Doubre and Peltzer, 2007], excavation or abandonment of buildings, sedimentation of rivers [Smith, 2002] and tectonics again. These phenomena render different spatial, temporal probability and intensity from landslides. Also, for each element at risk, its vulnerability and exposure to these hazards are considered to be diverse. Failing to eliminate these factors can lead to an overestimation of expected losses for landslide risk assessment. As a result, further improvements should include an approach to remove those mis-detected hotspots.

6.5 Landslide risk management

The rapid development of remote sensing has brought the significant improvement in landslide hazard analysis: diverse data sources, sophisticated processing techniques and extensive applications. However, how to transfer the knowledge of remote sensing technique into the operational institutions and the general public remains a critical problem, considering that they are not expected to have the sufficient knowledge of landslide hazard identification and risk assessment. This requires an effective risk management which helps the operational institutions and the general public to understand how to deal with landslide hazard and risks with a variety of strategies, for the purpose of minimizing future damages as well as losses of lives. Also, a quantitative landslide risk assessment is crucial if the risk management has to be judged quantitatively. A framework and guideline for landslide risk assessment and management was proposed by Fell et al. [2005, 2008], as displayed in figure 6.16.

Dai et al. [2002] has summarized landslide risk management concerns into five separated branches: planning control, engineering solution, acceptance, monitoring and warning systems, and decision-making. First, for the planning control, remote sensing plays an important role for providing relevant information for risk management. For example, in this study, the landslide hotspot map generated from PSI data highlights those landslide-prone areas where potential slow-moving landslides exist however could easily be neglected due to few observed damages. Also, a landslide hazard zonation map is beneficial for regulate, prohibit and minimize in landslide-prone areas. Second, for engineering solution, an example of successful risk management in Carbonile village has already been mentioned in

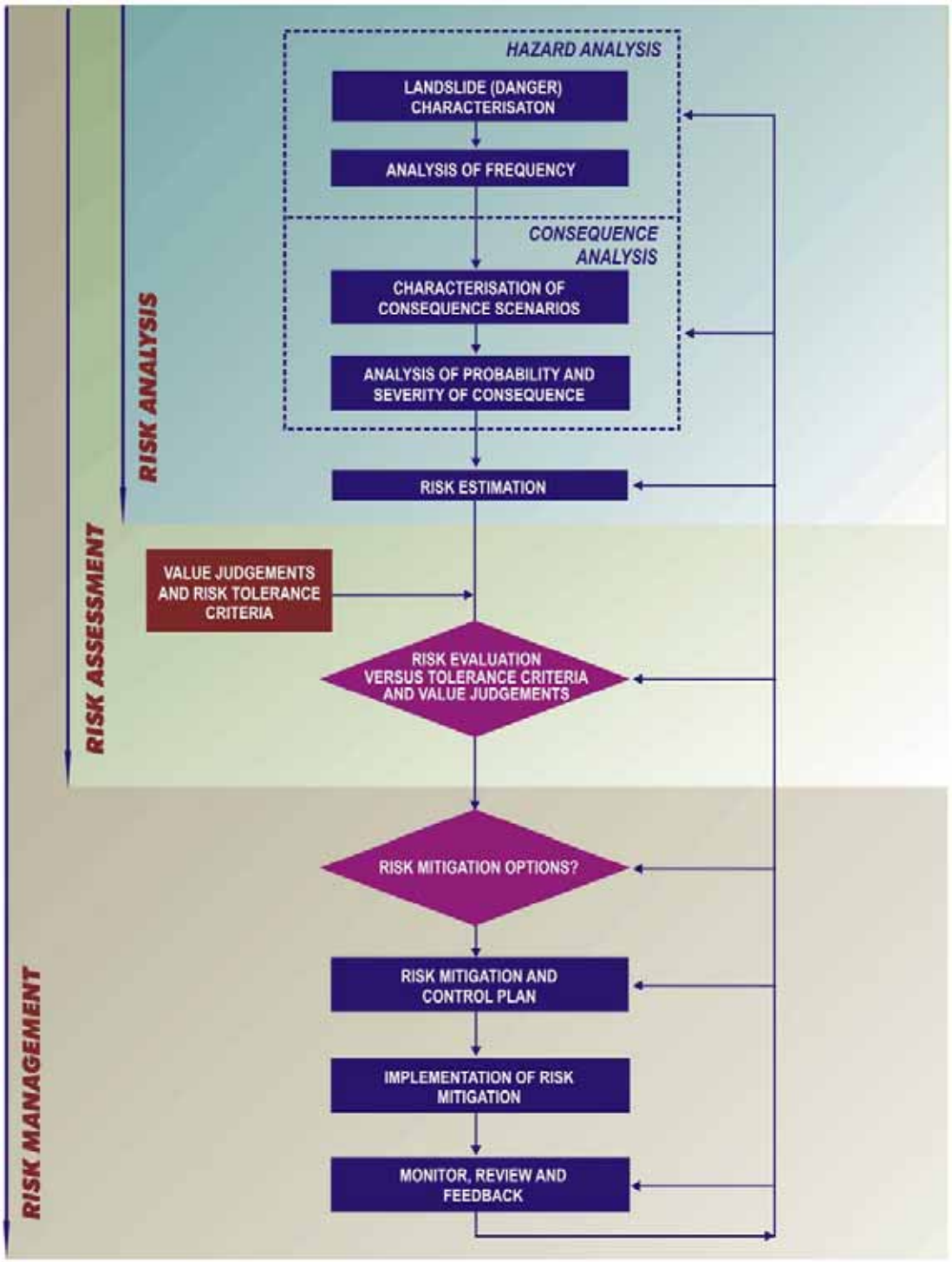

Figure 6.16: Guideline and framework for landslide risk management as proposed by Fell et al. [2005, 2008].

chapter 4. After the detection of mass movements from PS data, several remedial works of drainage collectors, trench drains and sheet piles were installed in order to stabilize slopes for risk mitigation, with an integration of correction of the underlying unstable slope and a control of the landslide movement. Third, in terms of the acceptance of landslide risks, it is difficult to be judged from remote sensing techniques. A major difficulty is that it is not easy to judge tolerable risk directly from remote sensing data or techniques. Dai et al. [2002] used frequency-fatality curve to define the threshold for acceptable risks, however it involves a degree of uncertainty in the analysis. Whether the landslide risk is tolerated or not is not reliably determined from remote sensing. Fourth, for the monitoring and warning systems, this represents the major advantage of remote sensing technique as reviewed in chapter 2. Especially for the real-time monitoring and warning system, ground and satellite-based InSAR is increasing their uses in recent years. Other useful techniques of landslide warning system for observing landslide kinematics include GPS, long-range terrestrial laser scanning and terrestrial oblique optical images. However, although the technique is developed quite well in monitoring and warning system, improvement should be focused on how to formulate the criteria for distributing warning messages and making evacuation plans. Finally, for decision making, although it exceeds the objective of remote sensing, providing a cost-benefit analysis for remote sensing technique could facilitate the communication between technicians and decision makers, thus bringing the science into society.

Chapter 7

Conclusion

Remote sensing is a valuable tool for landslide researches. In this study, two semi-automatic approaches for landslide rapid mapping and detection through remote sensing data were introduced. These two approaches focus on two different types of mass movements: (1) rapid-moving shallow landslides and debris flows, and (2) slow-moving deep-seated landslides.

The first approach, which is based on a recently developed technique of Object-Oriented Analysis (OOA), aims at a semi-automatic preparation of polygon-based landslide inventory for rapid-moving landslides. The usefulness of this OOA approach was demonstrated on the Messina landslide event in southern Italy that occurred on 1 October 2009. Two VHR optical imageries of QuickBird were utilized for the analysis. At the beginning stage, a fully automatic image segmentation with multi-scale optimization was performed on the post-event QuickBird imagery. The purpose is to maximally reduce the over- and under-segmentation for an automatic delineation of landslide objects, and meanwhile avoid a time-consuming 'trial and error' estimation of the optimal segmentation parameters

which has featured most OOA approaches in the past studies. The following approaches were accomplished with several spectral and textural analysis. Firstly, a change detection analysis was carried out based on the Principal Component Analysis (PCA) on stacked multi-spectral bands from both pre- and post-event QuickBird images. Landslide candidates were initially determined from 4th principal component through the membership function calculated from 10 selected samples of landslide objects. Besides, the derived 2nd principal component can be used to remove false positives of roads, infrastructures, deforestation areas and water. Secondly, a spectral anomaly detection was performed on pre-event imagery using Reed-Xiaoli anomaly Detector (RXD) in order to exclude those spectral anomalies that has already existed before the landslide occurrence. Thirdly, a spectral matching image between the pre- and post-event images was created using Spectral Angle Mapper (SAM) so as to remove false positives of subtle spectral changes from the change of spectrum vector direction. Finally, a textural analysis using Grey Level Co-occurrence Matrix (GLCM) mean was performed on an additional 1m LiDAR DTM acquired shortly after the event. The aim is to topographically eliminate those false positives with low-frequency elevation variation. The whole approach, which targets at a minimum manual participation, was developed in a training area of Altolia and implemented with any modification in a larger independent testing area of Itala. This OOA approach enables a successful mapping of 198 newly-triggered landslides, with the user's accuracy of 81.8% and producer's accuracy of 69.5% for the number of landslides, and the user's accuracy of 75.9% and producer's accuracy of 69.9% for the spatial extent of mapped landslides.

The second approach, the Persistent Scatterers Interferometry Hotspot and

Clustering Analysis (PSI-HCA), which is calculated based on two spatial statistics analysis of the Getis-Ord G_i^* statistic and kernel density estimation on PSI point targets, makes possible a detection of slow-moving mass movements within the detection precision of millimeters. The output of this PSI-HCA approach is the hotspot map indicating where potential slow-moving mass movements exist, rendered with two different colors according to different moving directions along LOS. In particular, red hotspots indicate potential landslides moving away from LOS whereas blue hotspots suggest mass movements towards LOS. The PSI-HCA approach gains its benefit from an integration of both PS velocity and spatial distribution. When the flat area was masked out and only PS in mountainous and hilly areas were concentrated, PSI-HCA shows its potential in the detection of extremely slow-moving landslides. The major difficulty of PSI-HCA results from the ground movement related to other geophysical processes that could be also identified by the detected displacements. These false detections mainly exist in the blue hotspots indicating mass movement towards LOS. Notwithstanding this difficulty, PSI-HCA shows its usefulness in an efficient detection of slow-moving landslides within a large area from huge amount of PS data, which is considered to be updated even more frequently with the advent of new generation of short wavelength X-band satellite platform.

The output of PSI-HCA was further included in a quantitative landslide hazard and risk mapping. The purpose is to quantitatively assess landslide risks from the information provided by landslide hotspots, thus making possible a comparison at the risk level between two semi-automatic landslide detection and mapping approaches: OOA for rapid-moving landslide mapping and PSI-HCA for slow-moving landslide detection. Based on the previously derived landslide

susceptibility map accomplished by Catani et al. [2005b] using ANN predictor, landslide hazard maps for five temporal predictions of 2, 5, 10, 20 and 30 years were produced by classifying the kernel density values of the hotspot map. In addition, for each PS, maximum velocity was calculated from its smoothed time series record and these maximum velocities were subsequently interpolated into a prediction map using ordinary kriging approach. With given intensity, elements at risk were extracted from the updated CORINE land cover map and the regional digital topographic map. The risk was calculated for 2, 5, 10, 20 and 30 years with the exposure of losses estimated in euro. In particular, approximately 3.22 billion euro losses were expected for the upcoming 30 years due to these slow-moving landslides as indicated in the hotspot map.

Future improvements should be focused on the following aspects. First, the segmentation approach for OOA can be further improved. Although current approach of image segmentation with multi-scale optimization is fully automatic, and can largely reduce the over- and under-segmentation of landslide objects, it is still facing the difficulty in completely delineating each single landslide object. More sophisticated statistical methods for image segmentation optimization as well as region growing are expected. Second, current selection of thresholds is primarily based on attempts of 'trial and error', thereby limiting the approach to be fully automatic. Further researches can be concentrated on an automatic threshold definition from the statistics analysis of different input layers in OOA. Third, how to decrease the cost of OOA approach should be taken into consideration. Since the current study employs VHR optical images, further attempts can be performed on mid-resolution optical images such as ASTER imagery which offers a large deduction of cost. Fourth, in future studies it is possible to include robust

filtering algorithm for raw LiDAR point clouds to eliminate those off-terrain signals, thus enabling an automatic bare-earth extraction for textural analysis using GLCM mean in OOA. Fifth, for the approach of PSI-HCA, the priority concern should be given to the efforts to increase the PS density. One solution is to process high resolution X-band SAR images in order to get more stable benchmarks. Alternative approach is to filter the interferograms over homogeneous area for the purpose of enhancing signal to noise ratio. Sixth, a better spatial definition of the G_i^* statistic parameterizations (e.g. by spatially distributing d_i values) and the possible inclusion of some series in spatial averaging schemes is preferred in the future work of PSI-HCA. Seventh, a novel approach of representing PS using hue and saturation scale can be promisingly involved in the future. With given density, the future hotspot and clustering analysis can be performed on the hue and saturation values in order to get the spatial clustering of moving direction and velocity. Finally but not the least, more attentions are needed to be paid to landslide risk management after hazard and risk analysis. In particular, the improvements should be focused on those efforts to increase the communication between researchers and decision makers, and those attempts to bring the science into society for an extensive public participation.

References

A. Abellan, M. Jaboyedoff, T. Oppikofer, and J. M. Vilaplana. Detection of millimetric deformation using a terrestrial laser scanner: experiment and application to a rockfall event. *Natural Hazards and Earth System Sciences*, 9: 365–372, 2009. 22

R. A. Al-Fares. The utility of synthetic aperture radar (sar) interferometry in monitoring sinkhole subsidence: subsidence of the devil's throat sinkhole area (nevada, usa). In B.F. Becker, editor, *Proceeding of 10th Multidisciplinary Conference on sinkholes and the engineering and environmental impacts of karst*, pages 541–547, San Antonio, TX, USA, 24-28 September 2005. 96, 152

D. H. al Khudairy, I. Caravaggi, and S. Glada. Structural damage assessments from ikonos data using change detection, object-oriented segmentation and classification techniques. *Photogrammetric Engineering and Remote Sensing*, 71(7):825–837, 2005. 30

G. Antonello, N. Casagli, P. Farina, D. Leva, G. Nico, A. J. Sieber, and D. Tarchi. Ground-based sar interferometry for monitoring mass movements. *Landslides*, 1(1):21–28, 2004. 17, 18

F. Antonioli, Luigi Ferranti, K. Lambeck, S. Kershaw, V. Verrubbi, and G. Dai

Pra. Late pleistocene to holocene record of changing uplift rates in southern calabria and northeastern sicily (southern italy, central mediterranean sea). *Tectonophysics*, 422:23–40, 2006. 35, 36

F. Ardizzone, M. Cardinali, M. Galli, F. Guzzetti, and P. Reichenbach. Identification and mapping of recent rainfall-induced landslides using elevation data collected by airborne lidar. *Natural Hazards and Earth System Science*, 7(6): 637–650, 2007. 20

M. Avian, A. Kellerer-Pirklbauer, and A. Bauer. Lidar for monitoring mass movements in permafrost environments at the cirque hinteres langtal, austria, between 2000 and 2008. *Natural Hazards and Earth System Sciences*, 9:1087–1094, 2009. xii, 21, 22

L. Ayalew and H. Yamagishi. The application of gis-based logistic regression for landslide susceptibility mapping in the kakuda-yahiko mountains, central japan. *Geomorphology*, 65:15–31, 2005. 104

M. Baatz and A. Schaepe. Multiresolution segmentation: an optimization approach for high quality multi-scale image segmentation. In *Angew. Geographische Informationsverarbeitung XII*, pages 12–23, Karlsruhe, Germany, 2000. 42

C. Baeza and J. Corominas. Assessment of shallow landslide susceptibility by means of multivariate statistical techniques. *Earth Surface Processes and Landforms*, 26(12):1251–1263, 2001. 104

S. B. Bai, J. Wang, G. N. Lu, P. G. Zhou, S. S. Hou, and S. N. Xu. Gis-based logistic regression for landslide susceptibility mapping of the zhongxian segment in the three gorges area, china. *Geomorphology*, 115:23–31, 2010. 104

M. Baldo, C. Bicocchi, U. Chiocchini, D. Giordan, and Giorgio Lollino. Lidar monitoring of mass wasting processes: The radicofani landslide, province of siena, central italy. *Geomorphology*, 105:193–201, 2009. 22

R. Bamler, B. Kampes, N. Adam, and S. Suchandt. Assessment of slow deformations and rapid motions by radar interferometry. In D. Fritsch, editor, *Proceedings of Photogrammetric Week 2005*, pages 111–122. Wichmann Verlag, Heidelberg, 2006. 76, 151

J. Barlow, Y. Martin, and S. E. Franklin. Detecting translational landslide scars using segmentation of landsat etm+ and dem data in the northern cascade mountains, british columbia. *Canadian journal of remote sensing*, 29(4):510–517, 2003. 32

J. Barlow, S. Franklin, and Y. Martin. High spatial resolution satellite imagery, dem derivatives, and image segmentation for the detection of mass wasting processes. *Photogrammetric Engineering and Remote Sensing*, 72(6):687–692, 2006. 32

R. L. Baum, J. A. Coe, J. W. Godt, E. L. Harp, M. E. Reid, W. Z. Savage, W. H. Schulz, D. L. Brien, A. F. Chleborad, and J. P. McKenna. Regional landslide-hazard assessment for seattle, washington, usa. *Landslides*, 2(4):266–279, 2005. 20

U. C. Benz, P. Hofmann, G. Willhauck, I. Lingenfelder, and M. Heynen. Multi-resolution, object-oriented fuzzy analysis of remote sensing data for gis-ready information. *ISPRS Journal of Photogrammetry and Remote Sensing*, 58:239–258, 2004. 27, 28, 30, 32, 42

P. Berardino, G. Fornaro, R. Lanari, and E. Sansosti. A new algorithm for surface deformation monitoring based on small baseline differential sar interferograms. *IEEE Transactions on Geoscience and Remote Sensing*, 40:2375–2383, 2002. 70, 71

P. Blanco-Sanchez, J. J. Mallorqui, S. Duque, and D. Monells. The coherent pixels technique (cpt): An advanced dinsar technique for nonlinear deformation monitoring. *Pure and Applied Geophysics*, 165(6):1167–1193, 2008. 68, 71

T. Blaschke. In *IEEE proceedings*. Washington DC, USA, 2003. 29

T. Blaschke. Object based image analysis for remote sensing. *ISPRS Journal of Photogrammetry and Remote Sensing*, 65(1):2–16, 2010. 28, 30, 32

L. Blesius and F. Weirich. Shallow landslide susceptibility mapping using stereo air photos and thematic maps. *Cartography and Geographic Information Science*, 37(2):105–118, 2010. 11

M. Boccaletti and F. Sani. Cover thrust reactivations related to internal basement involvement during neogene-quaternary evolution of the northern apennines. *Tectonics*, 17(1):112–130, 1998. 78

A. M. Booth, J. J. Roering, and J. T. Perron. Automated landslide mapping using spectral analysis and high-resolution topographic data: Puget sound lowlands, washington, and portland hills, oregon. *Geomorphology*, 109:132–147, 2009. 20, 31

L. Borgatti and M. Soldati. Landslides as a geomorphological proxy for climate

change: A record from the dolomites (northern italy). *Geomorphology*, 120: 56–64, 2010. 3

A. M. Borghuis, K. Chang, and H. Y. Lee. Comparison between automated and manual mapping of typhoon-triggered landslides from spot-5 imagery. *International Journal of Remote Sensing*, 28(8):1843 – 1856, 2007. 14, 31

F. Bovenga, R. Nutricato, A. Refice, and J. Wasowski. Application of multitemporal differential interferometry to slope instability detection in urban/periurban areas. *Engineering Geology*, 88:218–239, 2005. 70

F. Brardinoni, O. Slaymaker, and M. A. Hassan. Landslide inventory in a rugged forested watershed: a comparison between air-photo and field survey data. *Geomorphology*, 54:179–196, 2003. 11

C. Briese, N. Pfeifer, and P. Dorninger. Applications of the robust interpolation for dtm determination. In *International Archives of Photogrammetry and Remote Sensing, Photogrammetric Computer Vision*, Graz, Austria, 9-13 September 2002 2002. xviii, 134, 135

M. Brugioni. Analisi di deformazioni superficiali e di movimenti di bersagli radar mediante elaborazione di dati sar satellitari con la tecnica dei permanent scatterers. Technical report, The Arno river basin authority, 2007. 72

R. Buergmann, G. E. Hilley, and A. Ferretti. Resolving vertical tectonics in the san francisco bay area from permanent scatterer insar and gps analysis. *Geology*, 34:221–224, 2006. 96, 152

C. Burnett and T. Blaschke. A multi-scale segmentation/object relationship

modelling methodology for landscape analysis. *Ecological Modelling*, 168(3): 233–249, 2003. 29

P. Canuti and N. Casagli. Considerazioni sulla valutazione del rischio di frana. *CNR-GNDCI Publication*, 846:57, 1996. 112

P. Canuti, C. A. Garzonio, and G. Rodolfi. The influence of agricultural activity on slope stability: an example from montespertoli (tuscany, italy) representative area. In *Proceedings of Symposium of the IAEG*, pages 195–203. A.A. Balkema, Warsavia, 1979. 79

P. Canuti, N. Casagli, P. Focardi, and C. A. Garzonio. Lithology and slope instability phenomena in the basin of the arno river. *Mem Soc Geol Ital*, 48: 739–754, 1994. 110

P. Canuti, N. Casagli, L. Ermini, R. Fanti, and P. Farina. Landslide activity as a geoindicator in italy: significance and new perspectives from remote sensing. *Environmental Geology*, 45(7):907–919, 2004. 2, 3, 10, 17, 18

P. Canuti, N. Casagli, P. Farina, F. Marks, A. Ferretti, and G. Menduni. Land subsidence in the arno river basin studied through sar interferometry. In F. B. J. Barends, editor, *Proceedings of the 7th International Symposium on Land Subsidence*, pages 407–416, Shanghai, China, 2005. Millpress Science Publisher. 145, 148

P. Canuti, N. Casagli, P. Farina, F. Marks, A. Ferretti, and G. Menduni. Analisi dei fenomeni di subsidenza nel bacino del fiume arno mediante interferometria rada. *Giornale di Geologia Appllicata*, 4:131–136, 2006. 145, 148

P. Canuti, N. Casagli, F. Catani, G. Falorni, and P. Farina. Integration of remote sensing techniques in different stages of landslide response. In K. Sassa, H. Fukuoka, F. Wang, and G. Wang, editors, *Progress in Landslide Science*, 2007. 96, 152

M. Cardinali, P. Reichenbach, F. Guzzetti, F. Ardizzone, G. Antonini, M. Galli, M. Cacciano, M. Castellani, and P. Salvati. A geomorphological approach to the estimation of landslide hazards and risks in umbria, central italy. *Natural Hazards and Earth System Science*, 2:57–72, 2002. 103, 104, 105

A. Carrara, M. Cardinali, R. Detti, F. Guzzetti, V. Pasqui, and P. Reichenbach. Gis techniques and statistical models in evaluating landslide hazard. *Earth Surface Processes and Landforms*, 16(5):427–445, 1991. 104

A. Carrara, G. Crosta, and P. Frattini. Geomorphological and historical data in assessing landslide hazard. *Earth Surface Processes and Landforms*, 28(10): 1125C1142, 2003. 104

N. Casagli, F. Catani, G. Falorni, and P. Lu. Landslide monitoring through satellite and ground-based radar interferometry. workshop on real-time monitoring on landslides. In *Proceeding of 10th International Symposium on Landslides and Engineered Slopes*, Xi'an, China, June 30-July 4 2008. xii, 18

N. Casagli, R. Fanti, and G. Righini. Integration of vhr satellite images with field data for the analysis of debris sheet instability in the machu picchu area. In K. Sassa and P. Canuti, editors, *Landslides – Disaster Risk Reduction*, pages 275–281. Springer, 2009. 16

G. Castilla, G. J. Hay, and J. R. Ruiz. Size-constrained region merging (scrm): An automated delineation tool for assisted photointerpretation. *hotogrammetric Engineering and Remote Sensing*, 74(4):409–419, 2008. 30

F. Casu, M. Manzo, and R. Lanari. A quantitative assessment of the sbas algorithm performance for surface deformation retrieval from dinsar data. *Remote Sensing of Environment*, 102:195–210, 2006. 70, 71

F. Catani, P. Farina, S. Moretti, G. Nico, and T. Strozzi. On the application of sar interferometry to geomorphological studies: estimation of landform attributes and mass movements. *Geomorphology*, 68:119–131, 2005a. 17

F. Catani, N. Casagli, L. Ermini, G. Righini, and G. Menduni. Landslide hazard and risk mapping at catchment scale in the arno river basin. *Landslides*, 2: 329–342, 2005b. xvii, 78, 79, 87, 89, 103, 104, 105, 109, 110, 112, 114, 116, 121, 123, 124, 159

J. Chadwick, S. Dorsch, N. Glenn, G. Thackray, and K. Shilling. Application of multi-temporal high-resolution imagery and gps in a study of the motion of a canyon rim landslide. *ISPRS Journal of Photogrammetry and Remote Sensing*, 59(4):212–221, 2005. 14

C. I. Chang and S. S. Chiang. Anomaly detection and classification for hyperspectral imagery. *IEEE Transactions on Geoscience and Remote Sensing*, 40: 1314–1325, 2002. 56

K. T. Chau, Y. L. Sze, M. K. Fung, W. Y. Wong, E. L. Fong, and L. C. P. Chan. Landslide hazard analysis for hong kong using landslide inventory and gis. *Computers and Geosciences*, 30(4):429–443, 2004. 107

R. F. Chen, K. J. Chang, J. Angelier, Y. C. Chan, B. Deffontaines, C. T. Lee, and M. L. Lin. Topographical changes revealed by high-resolution airborne lidar data: The 1999 tsaoling landslide induced by the chi-chi earthquake. *Engineering Geology*, 88:160–172, 2006. 20

J. Choi, H. J. Oh, J. S. Won, and S. Lee. Validation of an artificial neural network model for landslide susceptibility mapping. *Environmental Earth Sciences*, 60 (3):473–483, 2010. 104

C. J. F. Chung and A. G. Fabbri. Validation of spatial prediction models for landslide hazard mapping. *Natural Hazards*, 30(3):451–472, 2003. 104

Civil-Protection. Landslide and mud flood emergency messina province, italy. Technical report, Italian Civil Protection, Region of Sicily, 2009. xiii, 35, 36, 37

J. A. Coe, P. A. Glancy, and J. W. Whitney. Volumetric analysis and hydrologic characterization of a modern debris flow near yucca mountain, nevada. *Geomorphology*, 20:11–28, 1997. 11

J. A. Coe, J. A. Michael, R. A. Crovelli, W. Z. Savage, W. T. Laprade, and W. D. Nashem. Probabilistic assessment of precipitation-triggered landslides using historical records of landslide occurrence, seattle, washington. *Environmental and Engineering Geoscience*, 10(2):103–122, 2004. 108

C. Colesanti and J. Wasowski. Investigating landslides with space-borne synthetic aperture radar (sar) interferometry. *Engineering Geology*, 88:173–199, 2006. 67, 70, 71, 72, 74, 75

C. Colesanti, A. Ferretti, C. Prati, and F. Rocca. Monitoring landslides and tectonic motions with the permanent scatterers technique. *Engineering Geology*, 68:3–14, 2003. 68, 70, 71, 72, 74, 96, 152

D. Colombo, P. Farina, S. Moretti, G. Nico, and C. Prati. Land subsidence in the firenze-prato-pistoia basin measured by means of spaceborne sar interferometry. In *Proceedings of IGARSS 2003, IEEE*, pages 2927–2929, Toulouse, France, 2003. Piscataway, NT. 148

R. G. Congalton. A review of assessing the accuracy of classifications of remotely sensed data. *Remote Sensing of Environment*, 37(1):35–46, 1991. 61

J. Corominas. The angle of reach as a mobility index for small and large landslides. *Canadian Geotechnical Journal*, 33(2):260C271, 1996. 105

A. Corsini, P. Farina, G. Antonello, M. Barbieri, N. Casagli, F. Coren, L. Guerri, F. Ronchetti, P. Sterzai, and D. Tarchi. Space-borne and ground-based sar interferometry as tools for landslide hazard management in civil protection. *International Journal of Remote Sensing*, 27(12):2351 – 2369, 2006. 16, 17, 18, 67

A. Corsini, L. Borgatti, F. Cervi, A. Dahne, F. Ronchetti, and P. Sterzai. Estimating mass-wasting processes in active earth slides-earth flows with time-series of high-resolution dems from photogrammetry and airborne lidar. *Natural Hazards and Earth System Sciences*, 9:433–439, 2009. 20

A.P. Cracknell. Review article synergy in remote sensing-what's in a pixel? *International Journal of Remote Sensing*, 19(11):2025–2047, 1998. 28

M. Crosetto, E. Biescas, J. Duro, J. Closa, and A. Arnaud. Generation of advanced ers and envisat interferometric sar products using stable point network technique. *Photogrammetric Engineering and Remote Sensing*, 74:443–450, 2008. 70, 71

M. Crosetto, O. Monserrat, R. Iglesias, and B. Crippa. Persistent scatterer interferometry: potential, limits and initial c- and x-band comparison. *Photogrammetric Engineering and Remote Sensing*, 76(9):1061–1069, 2010. xviii, 140, 141

G. Crosta. Regionalization of rainfall thresholds: an aid to landslide hazard evaluation. *Environmental Geology*, 35(2-3):131–145, 1998. 104

R. A. Crovelli. Probability models for estimation of number and costs of landslides. Technical report, U.S. Geological Survey, 2000. 108

M. J. Crozier and T. Glade. Frequency and magnitude of landsliding: fundamental research issues. *Zeitschrift fur Geomorphologie Supplementband*, 115: 141–155, 1999. 108

D. M. Cruden. A simple definition of a landslide. *Bulletin of Engineering Geology and the Environment*, 43(1):27–29, 1991. 1

D.M. Cruden and D. J. Varnes. Landslide types and processes. In A. K. Turner and R. L. Shuster, editors, *Landslides: Investigation and Mitigation*, pages 36–75. Transportation Research Board, National Research Council, National Academy Press, Washington, DC, 1996. 1, 25, 81, 95

F. C. Dai and C. F. Lee. Frequency-volume relation and prediction of rainfall-induced landslides. *Engineering Geology*, 59(3-4):253–266, 2001. 105

F. C. Dai, C. F. Lee, and Y. Y. Ngai. Landslide risk assessment and management: an overview. *Engineering Geology*, 64(1):65–87, 2002. 105, 153, 155

I. Das, S. Sahoo, C. J. van Westen, A. Stein, and R. Hack. Landslide susceptibility assessment using logistic regression and its comparison with a rock mass classification system, along a road section in the northern himalayas (india). *Geomorphology*, 114(4):627–637, 2010. 104

Definiens. *Definiens eCognition Developer User Guide*, 2010. 31, 42, 127

J. S. Deng, K. Wang, Y. H. Deng, and G. J. Qi. Pca-based land-use change detection and analysis using multitemporal and multisensor satellite data. *International Journal of Remote Sensing*, 29:4823–4838, 2008. 51, 52

P. E. Dennison, K. Q. Halligan, and D. A. Roberts. A comparison of error metrics and constraints for multiple endmember spectral mixture analysis and spectral angle mapper. *Remote Sensing of Environment*, 93:359–367, 2004. 54

M. H. Derron, L. H. Blikra, and M. Jaboyedoff. High resolution digital elevation model analysis for landslide hazard assessment (akerneset, norway). In K. Senneset, K. Flaate, and J. O. Larsen, editors, *Proceeding of Landslides and Avalanches: ICFL 2005*, pages 101–106, Norway, 2005. Taylor and Francis, London, UK. 20

O. Dewitte, C. J. Chung, Y. Cornet, M. Daoudi, and A. Demoulin. Combining

spatial data in landslide reactivation susceptibility mapping: a likelihood-ratio-based approach in w belgium. *Geomorphology*, 122:153–166, 2010. 104

R. A. Diaz-Varela, P. Ramil Rego, S. C. Iglesias, and C. Munoz Sobrino. Automatic habitat classification methods based on satellite images: A practical assessment in the nw iberia coastal mountains. *Environmental Monitoring and Assessment*, 144(1-3):229–250, 2008. 30

L. Donati and M. C. Turrini. An objective method to rank the importance of the factors predisposing to landslides with the gis methodology: application to an area of the apennines (valnerina; perugia, italy). *Engineering Geology*, 63: 277–289, 2002. 11

C. Doubre and G. Peltzer. Fluid-controlled faulting process in the asal rift, djibouti, from 8 yr of radar interferometry observations. *Geology*, 35:69–72, 2007. 96, 152

L. Dragut, T. Schauppenlehner, A. Muhar, J. Strobl, and T. Blaschke. Optimization of scale and parametrization for terrain segmentation: An application to soil-landscape modeling. *Computers and Geosciences*, 35:1875–1883, 2009. 46

J. Duro, J. Inglada, J. Closa, N. Adam, and A. Arnaud. High resolution differential interferometry using times series of ers and envisat sar data. In *Proceedings of FRINGE 2003, ESRIN*, Frascati, Italy, 1-5 December 2003 2003. 70, 71

H. S. B. Duzgun and S. Lacasse. Vulnerability and acceptable risk in integrated risk assessment framework. In O. Hungr, R. Fell, R. Couture, and E. Eberhardt, editors, *Landslide risk management*, page 505C515. Balkema, Rotterdam, The Netherlands, 2005. 106

M. Van Den Eeckhaut, T. Vanwalleghem, J. Poesen, G. Govers, G. Verstraeten, and L. Vandekerckhove. Prediction of landslide susceptibility using rare events logistic regression: A case-study in the flemish ardennes (belgium). *Geomorphology*, 76:392–410, 2006. 104

M. Van Den Eeckhaut, J. Poesen, G. Verstraeten, V. Vanacker, J. Nyssen, J. Moeyersons, L. P. H. van Beek, and L. Vandekerckhove. Use of lidar-derived images for mapping old landslides under forest. *Earth Surface Processes and Landforms*, 32(5):754–769, 2007. 20

M. Ehlers, M. Gaehler, and R. Janowsky. Automated analysis of ultra high-resolution remote sensing data for biotope type mapping: New possibilities and challenges. *ISPRS Journal of Photogrammetry and Remote Sensing*, 57 (5-6):315–326, 2003. 30

M. Ehlers, M. Gaehler, and R. Janowsky. Automated techniques for environmental monitoring and change analyses for ultra high-resolution remote sensing data. *Photogrammetric Engineering and Remote Sensing*, 72(7):835–844, 2006. 30

L. Ermini, F. Catani, and N. Casagli. Artificial neural networks applied to landslide susceptibility assessment. *Geomorphology*, 66:327–343, 2005. 104

T. Esch, M. Thiel, M. Bock, A. Roth, and S. Dech. Improvement of image segmentation accuracy based on multiscale optimization procedure. *IEEE Geoscience and Remote Sensing Letters*, 5:463–467, 2008. 46, 48, 125

G. M. Espindola, G. Camara, I. A. Reis, L. S. Bins, and A. M. Monteiro. Parameter selection for region-growing image segmentation algorithms using spatial

autocorrelation. *International Journal of Remote Sensing*, 27:3035–3040, 2006. 46

ESRI. *ArcGIS Desktop Tutorials*. ESRI, 2008. 115

A. G. Fabbri, C. J. F. Chung, A. Cendrero, and J. Remondo. Validation of spatial prediction models for landslide hazard mapping. *Natural Hazards*, 30 (3):487–503, 2003. 104

F. Falaschi, F. Giacomelli, P. R. Federici, A. Puccinelli, G. D'Amato Avanzi, A. Pochini, and A. Ribolini. Logistic regression versus artificial neural networks: landslide susceptibility evaluation in a sample area of the serchio river valley, italy. *Natural hazards*, 50(3):551–569, 2009. 104

P. Farina, D. Colombo, A. Fumagalli, E. Gontier, and S. Moretti. Integration of permanent scatterers anlaysis and high resolution optical images within landslide risk analysis. In *Proceedings of FRINGE 2003*, Frascati, Italy, 2-5 December 2003 2003. 70

P. Farina, D. Colombo, A. Fumagalli, F. Marks, and S. Moretti. Permanent scatterers for landslide investigations: outcomes from the esa-slam project. *Engineering Geology*, 88:200–217, 2006. 70, 79, 89, 91

R. Fell. Landslide risk assessment and acceptable risk. *Canadian geotechnical journal*, 31(2):261–272, 1994. 103, 105, 117, 121, 124

R. Fell, K. K. S. Ho, S. Lacasse, and E. Leroi. A framework for landslide risk assessment and management. In O. Hungr, R. Fell, R. Couture, and E. Eber-

hardt, editors, *Landslide Risk Management*, pages 3–26. Taylor and Francis, London, 2005. xx, 153, 154

R. Fell, J. Corominas, C. Bonnard, L. Cascini, E. Leroi, and W. Z. Savage. Guidelines for landslide susceptibility, hazard and risk zoning for land use planning. *Engineering Geology*, 102:85–98, 2008. xx, 103, 153, 154

A. Ferretti, C. Prati, and F. Rocca. Non-linear subsidence rate estimation using permanent scatterers in differential sar interferometry. *IEEE Transactions on Geoscience and Remote Sensing*, 38:2202–2212, 2000. 68, 70, 71, 72, 74, 96, 152

A. Ferretti, C. Prati, and F. Rocca. Permanent scatterers in sar interferometry. *IEEE Transactions on Geoscience and Remote Sensing*, 39:8–20, 2001. 67, 68, 70, 71, 72, 74

A. Ferretti, M. Basilico, F. Novali, and C. Prati. Possibile utilizzo dei dati radar satellitari per individuazione e monitoraggio di fenomeni di sinkholes. In *Proceedings of primo seminario sullo stato dell'arte dei fenomeni di sinkholes e ruolo delle amministrazioni statali e locali nel governo del territorio*, pages 415–424, 2004. 96, 152

A. Ferretti, C. Prati, F. Rocca, N. Casagli, P. Farina, and B. Young. Permanent scatterers technology: a powerful state of the art tool for historic and future monitoring of landslides and other terrain instability phenomena. In *Proceedings of International Conference on Landslide Risk Management 2005*, Vancouver, Canada, 31 May – 3 June 2005. 70, 72, 73, 74

A. Ferretti, G. Falorni, F. Novali, F. Rocca, A. Rucci, and A. Tamburini. Innovative applications of satellite interferometry in the oil and gas industry. In *ESA ESRIN Workshop*, Frascati, Italy, 14–15 September 2010. xviii, 140

P. J. Finlay. *The risk assessment of slopes*. PhD thesis, School of Civil Engineering, University of New South Wales, Australia, 1996. 106

P. J. Finlay, R. Fell, and P. K. Maguire. The relationship between the probability of landslide occurrence and rainfall. *Canadian Geotechnical Journal*, 34(6):811–824, 1997. 108

D. Flanders, M. Hall-Beyer, and J. Pereverzoff. Preliminary evaluation of ecognition object-based software for cut block delineation and feature extraction. *Canadian Journal of Remote Sensing*, 29(4):441C452, 2003. 28

I. G. Fourniadis, J. G. Liu, and P. J. Mason. Landslide hazard assessment in the three gorges area, china, using aster imagery: Wushan-badong. *Geomorphology*, 84:126–144, 2007. 14

B. Fruneau, J. Achache, and C. Delacourt. Observation and modelling of the saint-etienne-de-tinee landslide using sar interferometry. *Tectonophysics*, 265: 181–190, 1996. 17

C. Galeazzi. Prima: a new, competitive small satellite platform. *Acta Astronautica*, 46:379–388, 2000. 75

R. Gens and J. L. Van Genderen. Review article sar interferometryissues, techniques, applications. *International Journal of Remote Sensing*, 17(10):1803–1835, 1996. 16

A. Getis and J. K. Ord. The analysis of spatial association by use of distance statistics. *Geographical Analysis*, 24:189–206, 1992. 82, 138

A. Getis and J. K. Ord. Local spatial statistics: an overview. In P. Longley and M. Batty, editors, *Spatial Analysis: Modeling in a GIS Environment*, pages 261–277. WILEY, 1996. 82, 138

T. Glade and M. J. Crozier. The nature of landslide hazard impact. In T. Glade, M. Anderson, and M. J. Crozier, editors, *Landslide hazard and risk*, pages 43–74. Wiley, U.S., 2005. 108

N. F. Glenn, D. R. Streutker, D. J. Chadwick, G. D. Thackray, and S. J. Dorsch. Analysis of lidar-derived topographic information for characterizing and differentiating landslide morphology and activity. *Geomorphology*, 73:131–148, 2006. 20

H. Gomez and T. Kavzoglu. Assessment of shallow landslide susceptibility using artificial neural networks in jabonosa river basin, venezuela. *Engineering Geology*, 78:11–27, 2005. 104

P. Gong. Change detection using principal components analysis and fuzzy set theory. *Canadian Journal of Remote Sensing*, 19, 1993. 129

A. A. Green, M. Berman, P. Switzer, and M. D. Craig. A transformation for ordering multispectral data in terms of image quality with implications for noise removal. *IEEE Transactions on Geoscience and Remote Sensing*, 26, 1988. 131

J. Grodecki and G. Dial. Block adjustment of high-resolution satellite images

described by rational polynomials. *Photogrammetric Engineering and Remote Sensing*, 69(1):59–68, 2003. 49

R. P. Gupta and B. C. Joshi. Landslide hazard zoning using the gis approach–a case study from the ramganga catchment, himalayas. *Engineering Geology*, 28: 119–131, 1990. 13

F. Guzzetti. Landslide fatalities and the evaluation of landslide risk in italy. *Engineering Geology*, 58:89–107, 2000. 2, 103

F. Guzzetti, A. Carrara, M. Cardinali, and P. Reichenbach. Landslide hazard evaluation: a review of current techniques and their application in a multi-scale study, central italy. *Geomorphology*, 31:181–216, 1999. 104

F. Guzzetti, P. Reichenbach, and G. F. Wieczorek. Rockfall hazard and risk assessment in the yosemite valley, california, usa. *Natural Hazards and Earth System Sciences*, 3:491C503, 2003. 108

F. Guzzetti, P. Reichenbach, M. Cardinali, M. Galli, and F. Ardizzone. Probabilistic landslide hazard assessment at the basin scale. *Geomorphology*, 72: 272–299, 2005a. 61, 104

F. Guzzetti, C. P. Stark, and P. Salvati. Evaluation of flood and landslide risk to the population of italy. *Environmental management*, 36(1):15–36, 2005b. 103

R. M. Haralick, K. Shanmugam, and I. H. Dinstein. Textural features for image classification. *IEEE Transactions on Systems, Man and Cybernetics*, 6:610–621, 1973. 57

R. A. Haugerud, D. J. Harding, S. Y. Johnson, J. L. Harless, and C. S. Weaver. High-resolution lidar topography of the puget lowland, washington. *GSA Today*, 13(3):4–10, 2003. 20

G. J. Hay and K. O. Niemann. Visualizing 3-d texture: A three dimensional structural approach to model forest texture. *Canadian Journal of Remote Sensing*, 20(2):90–101, 1994. 27

G. J. Hay, K. O. Niernann, and D. G. Goodenough. Spatial thresholds, image-objects, and upscaling: A multiscale evaluation. *Remote Sensing of Environment*, 62(1):1–19, 1997. 27

G. J. Hay, D. J. Marceau, P. Dube, and A. Bouchard. A multiscale framework for landscape analysis: Object-specific analysis and upscaling. *Landscape Ecology*, 16(6):471–490, 2001. 27, 29

G. J. Hay, T. Blaschke, D. J. Marceau, and A. Bouchard. A comparison of three image-object methods for the multiscale analysis of landscape structure. *ISPRS Journal of Photogrammetry and Remote Sensing*, 57:327–345, 2003. 27, 29, 46

G. J. Hay, G. Castilla, M. A. Wulder, and J. R. Ruiz. An automated object-based approach for the multiscale image segmentation of forest scenes. *International Journal of Applied Earth Observation and Geoinformation*, 7(4):339–359, 2005. 30

G. Herrera, J. A. Fernandez-Merodo, J. Mulas, M. Pastor, G. Luzi, and O. Monserrat. A landslide forecasting model using ground based sar data: The portalet case study. *Engineering Geology*, 105:220–230, 2009. 17

J. Hervas, J. I. Barredo, P. L. Rosin, A. Pasuto, F. Mantovani, and S. Silvano. Monitoring landslides from optical remotely sensed imagery: the case history of tessina landslide, italy. *Geomorphology*, 54:63–75, 2003. 31, 33

Y. Heyman, C. Steenmans, G. Croisille, and M. Bossard. Corine land cover project technical guide. Ecsc-eec-eaec, European Commission, Directorate General Environment, Nuclear Safety and Civil Protection, Brussels- Luxembourg, 1994. 110, 117

G. E. Hilley, R. Burgmann, A. Ferretti, F. Novali, and F. Rocca. Dynamics of slow-moving landslides from permanent scatterer analysis. *Science*, 304(5679): 1952–1955, 2004. 70

Y. Hong, R. Adler, and G. Huffman. Evaluation of the potential of nasa multi-satellite precipitation analysis in global landslide hazard assessment. *Geophysical Research Letters*, 33:L22402, 2006. xii, 3, 4

Y. Hong, R. Adler, and G. Huffman. Use of satellite remote sensing data in the mapping of global landslide susceptibility. *Natural Hazards*, 43:245–256, 2007. xii, 3, 4

A. Hooper, H. Zebker, P. Segall, and B. Kampes. A new method for measuring deformation on volcanoes and other natural terrains using insar persistent scatterers. *Geophysical Research Letters*, 31, 2004. 68, 71

A. Hooper, P. Segall, and H. Zebker. Persistent scatterer insar for crustal deformation analysis, with application to volcan alcedo, galapagos. *Journal of Geophysical Research*, 112, 2007. 68, 71

S. Huang and B. Chen. Integration of landsat and terrain information for landslide study. In *The Proceeding of 8th Thematic Conference on Geologic Remote Sensing*, pages 743–754, Denver, CO, UNITED STATES, 29 April-2 May 1991 1991. 13

O. Hungr. A model for the runout analysis of rapid flow slides, debris flows, and avalanches. *Canadian Geotechnical Journal*, 32:610–623, 1995. 105, 114

O. Hungr. Some methods of landslide hazard intensity mapping. In D. M. Cruden and R. Fell, editors, *Landslide Risk Assessment*, pages 215–226. Balkema Publisher, Rotterdam, The Netherlands, 1997. 104, 105

O. Hungr, S. G. Evans, M. J. Bovis, and J. N. Hutchinson. A review of the classification of landslides of the flow type. *Environmental and Engineering Geoscience*, 7(3):221–238, 2001. 2

J. N. Hutchinson. General report: Morphological and geotechnical parameters of landslide in relation to geology and hydrogeology. In C. Bonnard, editor, *Landslides, Vol. I. 5th Int. Symp. on Landslides*, pages 3–35. Balkema Rotterdam, 1988. 1

IPCC. Intergovernmental panel on climate change (ipcc), climate change 2007: the physical science basis. contribution of working group i to the fourth assessment report of the intergovernmental panel on climate change. In S. Solomon, D. Qin, M. Manning, Z. Chen, M. Marquis, K. B. Avery, M. Tignor, and H. L. Miller, editors, *Fourth Assessment Report*, page 996. Cambridge University Press, Cambridge, UK, and New York, USA, 2007. 3

ISDR. International decade for natural disaster reduction: successor arrangements. Report of the secretary-general, International Strategy for Disaster Reduction (ISDR), UN, www.unisdr.org, 1999. 102

M. Jaboyedoff, R. Metzger, T. Oppikofer, R. Couture, M. H. Derron, J. Locat, and D. Turmel. New insight techniques to analyze rock-slope relief using dem and 3d-imaging cloud points: Coltop-3d software. In E. Eberhardt, D. Stead, and T. Morrison, editors, *Rock mechanics: Meeting Society's challenges and demands, Proceedings of the 1st Canada - U.S. Rock Mechanics Symposium*, pages 61–68, Vancouver, Canada, 27-31 May 2007 2007. Taylor and Francis, London, UK. 22

P. Jaiswal, C. J. van Westen, and V. Jetten. Quantitative landslide hazard assessment along a transportation corridor in southern india. *Natural Hazards and Earth System Sciences*, 10:1253–1267, 2010. 103

M. Jakob and S. Lambert. Climate change effects on landslides along the southwest coast of british columbia. *Geomorphology*, 107:275–284, 2009. 3

J. Jensen. In *Introductory Digital Image Processing, a Remote Sensing Perspective*. Upper Saddle River, NJ: Prentice-Hall, 1996. 129

L. D. Jones. Monitoring landslides in hazardous terrain using terrestrial lidar: an example from montserrat. *Quarterly Journal of Engineering Geology and Hydrogeology*, 39(4):371–373, 2006. 22

kaab. Monitoring high-mountain terrain deformation from repeated air-and spaceborne optical data: examples using digital aerial imagery and aster data. *ISPRS Journal of Photogrammetry and Remote Sensing*, 57:39–52, 2002. 11

D. P. Kanungo, M. K. Arora, R. P. Gupta, and S. Sarkar. Landslide risk assessment using concepts of danger pixels and fuzzy set theory in darjeeling himalayas. *Landslides*, 5(4):407–416, 2008. 103

A. M. Kaynia, M. Papathoma-Koehle, B. Neuhaeuser, K. Ratzinger, H. Wenzel, and Z. Medina-Cetina. Probabilistic assessment of vulnerability to landslide: application to the village of lichtenstein, baden-wuerttemberg, germany. *Engineering Geology*, 101:33–48, 2008. 106

D. Kim, S. Im, S. H. Lee, Y. Hong, and K. S. Cha. Predicting the rainfall-triggered landslides in a forested mountain region using trigrs model. *Journal of Mountain Science*, 7(1), 2010. 14

H. Kimura and Y. Yamaguchi. Detection of landslide areas using satellite radar interferometry. *Photogrammetric Engineering and Remote Sensing*, 66(3):337–344, 2000. 67

M. Kouli, C. Loupasakis, P. Soupios, and F. Vallianatos. Landslide hazard zonation in high risk areas of rethymno prefecture, crete island, greece. *Natural Hazards*, 52(3):599–621, 2010. 16

F. A. Kruse, A. B. Lefkoff, J. W. Boardman, K. B. Heidebrecht, A. T. Shaprio, P. J. Barloon, and A. F. H. Goetz. The spectral image processing system (sips) - interactive visualization and analysis of imaging spectrometer data. *Remote Sensing of Environment*, 44:145–163, 1993. 54, 56

M. Lackner and T. M. Conway. Determining land-use information from land cover through an object-oriented classification of ikonos imagery. *Canadian Journal of Remote Sensing*, 34(2):77–92, 2008. 30

R. Lanari, O. Mora, M. Manunta, J. J. Mallorqui, P. Berardino, and E. Sansosti. A small-baseline approach for investigating deformations on full-resolution differential sar interferograms. *IEEE Transactions on Geoscience and Remote Sensing*, 42:1377–1386, 2004. 70, 71

M. Lato, J. Hutchinson, M. Diederichs, D. Ball, and R. Harrap. Engineering monitoring of rockfall hazards along transportation corridors: using mobile terrestrial lidar. *Natural Hazards and Earth System Sciences*, 9:935–946, 2009. 23

S. Lee. Application of logistic regression model and its validation for landslide susceptibility mapping using gis and remote sensing data. *International Journal of Remote Sensing*, 26(7):1477–1491, 2005. 104

S. Lee. Application of likelihood ratio and logistic regression models to landslide susceptibility mapping using gis. *Environmental Management*, 34(2):223–232, 2004. 104

S. Lee and B. Pradhan. Probabilistic landslide hazards and risk mapping on penang island, malaysia. *Journal of Earth System Science*, 115(6):661–672, 2006. 103

S. Lee, J. H. Ryu, J. S. Won, and H. J. Park. Determination and application of the weights for landslide susceptibility mapping using an artificial neural network. *Engineering Geology*, 71:289–302, 2004. 104

S. Lee, J. H. Ryu, and I. S. Kim. Landslide susceptibility analysis and its verification using likelihood ratio, logistic regression, and artificial neural network models: case study of youngin, korea. *Landslides*, 4(4):327–338, 2007. 104

F. J. Van Leijen and R. F. Hanssen. Persistent scatterer density improvement using adaptive deformation models. In *Proceedings of IGARSS 2007*, pages 2102–2105, Barcelona, Spain, 23-27 July 2007 2007. IEEE, Piscataway, NT. 76

F. Lentini, S. Carbone, S. Catalano, A. Di Stefano, C. Gargano, M. Romeo, S. Strazzulla, and G. Vinci. Sedimentary evolution of basins in mobile belts: examples from the tertiary terrigenous sequences of the peloritani mountains (ne sicily). *Terra Nova*, 7(2):160–171, 1995. 35, 36

F. Leone, J. P. Aste, and E. Leroi. Vulnerability assessment of elements exposed to mass-movements: working toward a better risk perception. In K. Senneset, editor, *Landslides-Glissements de Terrain*, pages 263–270. Balkema, Rotterdam, The Netherlands, 1996. 106

S. Leroueil, J. Vaunat, L. Picarelli, J. Locat, H. Lee, and R. Faure. Geotechnical characterisation of slope movements. In K. Senneset, editor, *Proceedings of the 7th International Symposium on Landslides*, pages 53–74, Trondheim, Norway, 1996. 2

D. Leva, G. Nico, D. Tarchi, J. Fortuny-Guasch, and A. J. Sieber. Temporal analysis of a landslide by means of a ground-based sar interferometer. *IEEE Transactions on Geoscience and Remote Sensing*, 41(4):745–752, 2003. 17, 19

Z. Li, F. Nadim, H. Huang, M. Uzielli, and S. Lacasse. Quantitative vulnerability estimation for scenario-based landslide hazards. *Landslides*, 7(2):125–134, 2010. 105

T. M. Lillesand and R. W. Kiefer. *Remote Sensing and Image Interpretation*. Wiley, New York, NY., 1987. 10

C. Lin, C. Shieh, B. Yuan, Y. Shieh, S. Liu, and S. Lee. Impact of chi-chi earthquake on the occurrence of landslides and debris flows: example from the chenyulan river watershed, nantou, taiwan. *Engineering Geology*, 71:49–61, 2004. 14, 130

W. T. Lin, W. c. Chou, C. Y. Lin, P. H. Huang, and J. S. Tsai. Vegetation recovery monitoring and assessment at landslides caused by earthquake in central taiwan. *Forest Ecology and Management*, 210:55–66, 2005. 130

W. T. Lin, C. Y. Lin, and W. c. Chou. Assessment of vegetation recovery and soil erosion at landslides caused by a catastrophic earthquake: A case study in central taiwan. *Ecological Engineering*, 28(1):79–89, 2006. 130

J. G. Liu, P. J. Mason, N. Clerici, S. Chen, A. Davis, F. Miao, H. Deng, and L. Liang. Landslide hazard assessment in the three gorges area of the yangtze river using aster imagery: Ziguicbadong. *Geomorphology*, 61:171–187, 2004. 14

P. Lu, N. Casagli, and F. Catani. Psi-hsr: a new approach for representing persistent scatterer interferometry (psi) point targets using the hue and saturation scale. *International Journal of Remote Sensing*, 31(8):2189–2196, 2010. 96

P. Lunardi. Tunnelling under the mugello moto racing circuit incorporating the adeco-rs approach. *Tunnel*, 8:24–31, 2000. 99

G. Luzi, M. Pieraccini, D. Mecatti, L. Noferini, G. Guidi, F. Moia, and C. Atzeni. Ground-based radar interferometry for landslides monitoring: Atmospheric and instrumental decorrelation sources on experimental data. *IEEE Transactions on Geoscience and Remote Sensing*, 42(11):2454–2466, 2004. 17

G. Luzi, M. Pieraccini, D. Mecatti, L. Noferini, G. Macaluso, A. Galgaro, and C. Atzeni. Advances in ground-based microwave interferometry for landslide survey: a case study. *International Journal of Remote Sensing*, 27(12): 2331C2350, 2006. 17

G. Luzi, L. Noferini, D. Mecatti, G. Macaluso, M. Pieraccini, C. Atzeni, A. Schaffhauser, R. Fromm, and T. Nagler. Using a ground-based sar interferometer and a terrestrial laser scanner to monitor a snow-covered slope: Results from an experimental data collection in tyrol (austria). *IEEE Transactions on Geoscience and Remote Sensing*, 47(2):382–393, 2009. 18

B. D. Malamud, D. L. Turcotte, F. Guzzetti, and P. Reichenbach. Landslide inventories and their statistical properties. *Earth Surface Processes and Landforms*, 29:687–711, 2004. 46, 107

F. Mantovani, R. Soeters, and C. J. Van Westen. Remote sensing techniques for landslide studies and hazard zonation in europe. *Geomorphology*, 15:213–225, 1996. 10, 11, 13

F. Marks. *Application of remote sensing and GIS for ground instability analysis.* PhD thesis, University of Firenze, 2006. 77, 78, 79

T. R. Martha, N. Kerle, V. Jetten, C. J. van Westen, and K. V. Kumar. Characterising spectral, spatial and morphometric properties of landslides for semi-automatic detection using object-oriented methods. *Geomorphology*, 116:24–36, 2010. 32, 42, 49

T. R. Martha, N. Kerle, C. J. Van Westen, V. Jetten, and K. V. Kumar. Segment optimisation and data-driven thresholding for knowledge-based landslide

detection by object-oriented image analysis. *IEEE Transactions on Geoscience and Remote Sensing*, in review. 46

Y. E. Martin and S. E. Franklin. Classification of soil-and bedrock-dominated landslides in british columbia using segmentation of satellite imagery and dem data. *International journal of remote sensing*, 26(7):1505–1509, 2005. 32

P. J. Mason, M. S. Rosenbaum, and J. M. Moore. Digital image texture analysis for landslide hazard mapping. In J. G. Maund and M. Eddleston, editors, *Geohazards in Engineering Geology*, volume 15, pages 297–305. The Geological Society, London, 1998. 57

D. Massonet, K. Feigl, M. Rossi, and F. Adragna. Radar interferometric mapping of deformation in the year after the landers earthquake. *Nature*, 369:227–230, 1994. 96, 152

D. Massonet, T. Holzer, and H. Vadon. Land subsidence caused by the east mesa geothermal field, california, observed using sar interferometry. *Geophysical Research Letters*, 24:901–904, 1997. 96, 152

D. Massonnet and K. L. Feigl. Radar interferometry and its application to changes in the earth's surface. *Reviews of Geophysics*, 36(4):441–500, 1998. 16, 65, 67

O. Mavrouli and J. Corominas. Rockfall vulnerability assessment for reinforced concrete buildings. *Natural Hazards and Earth System Sciences*, 10:2055–2066, 2010. 106

J. McKean and J. Roering. Objective landslide detection and surface morphology

mapping using high-resolution airborne laser altimetry. *Geomorphology*, 57: 331–351, 2004. 20, 31

C. Melchiorre, M. Matteucci, A. Azzoni, and A. Zanchi. Artificial neural networks and cluster analysis in landslide susceptibility zonation. *Geomorphology*, 94: 379–400, 2008. 104

G. Metternicht, L. Hurni, and R. Gogu. Remote sensing of landslides: An analysis of the potential contribution to geo-spatial systems for hazard assessment in mountainous environments. *Remote Sensing of Environment*, 98:284–303, 2005. 10, 11

M. Michael-Leiba, F. Baynes, G. Scott, and K. Granger. Regional landslide risk to the cairns community. *Natural hazards*, 30(2):233–249, 2003. 103

M. Moine, A. Puissant, and J. P. Malet. Detection of landslides from aerial and satellite images with a semi-automatic method. application to the barcelonnette basin (alpes-de-haute-provence, france). In J. P. Malet, A. Remaitre, and T. Bogaard, editors, *Landslide Processes: From Geomorphological Mapping to Dynamic Modelling*, pages 63–68, CERG, Strasbourg, France, 2009. 32

C. Monaco and L. Tortorici. Active faulting in the calabrian arc and eastern sicily. *Journal of Geodynamics*, 29:407–424, 2000. 35, 36

O. Mora, J. J. Mallorqui, and A. Broquetas. Linear and nonlinear terrain deformation maps from a reduced set of interferometric sar images. *IEEE Transactions on Geoscience and Remote Sensing*, 41:2243–2253, 2003. 68, 71

M. Motagh, J. Hoffmann, B. Kampes, M. Baes, and J. Zschau. Strain accumulation across the gazikoy-saros segment of the north anatolian fault inferred from persistent scatterer interferometry and gps measurements. *Earth and Planetary Science Letters*, 255:432–444, 2007. 136

F. Nadim. Probabilistic methods for geohazards problems: state-of-the-art. In *UEF Conference*, Graz, Austria, 2002. 5

F. Nadim, O. Kjekstad, P. Peduzzi, C. Herold, and C. Jaedicke. Global landslide and avalanche hotspots. *Landslides*, 3(2):159–173, 2006. xii, 3, 4, 5, 103

R. Nagarajan, A. Roy, R. Vinod Kumar, A. Mukherjee, and M. V. Khire. Landslide hazard susceptibility mapping based on terrain and climatic factors for tropical monsoon regions. *Bulletin of Engineering Geology and the Environment*, 58(4):275–287, 2000. 104

NASA. Global landslide risks map. available on internet: http://earthobservatory.nasa.gov, 2007. xii, 4

H. A. Nefeslioglu, T. Y. Duman, and S. Durmaz. Landslide susceptibility mapping for a part of tectonic kelkit valley (eastern black sea region of turkey). *Geomorphology*, 94:401–418, 2008. 104

J. Nichol and M. S. Wong. Satellite remote sensing for detailed landslide inventories using change detection and image fusion. *International Journal of Remote Sensing*, 26(9):1913–1926, 2005. 14, 33

J. E. Nichol and A. Shaker. Application of high-resolution stereo satellite images to detailed landslide hazard assessment. *Geomorphology*, 76:68–75, 2006. 14

I. Niemeyer, M. Canty, and D. Klaus. Unsupervised change detection techniques using multispectral satellite images. In *Proceeding of IEEE International Geoscience and Remote Sensing Symposium*, pages 327–329, 1999. 129

L. Noferini, M. Pieraccini, D. Mecatti, G. Luzi, C. Atzeni, A. Tamburini, and M. Broccolato. Permanent scatterers analysis for atmospheric correction in ground-based sar interferometry. *IEEE Transactions on Geoscience and Remote Sensing*, 43(7):1459–1471, 2005. 17

L. Noferini, M. Pieraccini, D. Mecatti, G. Macaluso, G. Luzi, and C. Atzeni. Long term landslide monitoring by ground-based synthetic aperture radar interferometer. *International Journal of Remote Sensing*, 27(10):1893–1905, 2006. 17

L. Noferini, M. Pieraccini, D. Mecatti, G. Macaluso, C. Atzeni, M. Mantovani, G. Marcato, A. Pasuto, S. Silvano, and F. Tagliavini. Using gb-sar technique to monitor slow moving landslide. *Engineering Geology*, 95:88–98, 2007. 17

L. Noferini, T. Takayama, M. Pieraccini, D. Mecatti, G. Macaluso, G. Luzi, and C. Atzeni. Analysis of ground-based sar data with diverse temporal baselines. *IEEE Transactions on Geoscience and Remote Sensing*, 46(6):1614–1623, 2008. 17

F. Novali, A. Ferretti, A. Fumagalli, F. Rocca, C. Prati, and A. Rucci. The second generation psinsar approach: Squeesar. In *Proceedings of FRINGE 2009*, Frascati, Italy, 30 November – 4 December 2009 2009. xix, 76, 140, 142, 151

OFDA/CRED. Em-dat international disaster databasehttp://www.em-dat.net, universit catholique de louvain, brussels, belgium, 2006. 3

T. Oppikofer, M. Jaboyedoff, L. Blikra, M. H. Derron, and R. Metzger. Characterization and monitoring of the aknes rockslide using terrestrial laser scanning. *Natural Hazards and Earth System Sciences*, 9:1003–1019, 2009. 22

J. K. Ord and A. Getis. Local spatial autocorrelation statistics: distributional issues and application. *Geographical Analysis*, 27:286–306, 1995. 82, 138

L. A. Owen, U. Kamp, G. A. Khattak, E. L. Harp, D. K. Keefer, and Mark A. Bauer. Landslides triggered by the 8 october 2005 kashmir earthquake. *Geomorphology*, 94:1–9, 2008. 14

I. Parcharidis, M. Foumelis, P. Kourkouli, and U. Wegmuller. Persistent scatterers insar to detect ground deformation over rio-antirio area (western greece) for the period 1992-2000. *Journal of Applied Geophysics*, 68:348–355, 2009. 137

M. Parise. Landslide mapping techniques and their use in the assessment of the landslide hazard. *Physics and Chemistry of the Earth, Part C: Solar, Terrestrial and Planetary Science*, 26(9):697–703, 2001. 11

N. W. Park and K. H. Chi. Quantitative assessment of landslide susceptibility using high-resolution remote sensing data and a generalized additive model. *International Journal of Remote Sensing*, 29(1):247–264, 2008. 33

C. Pascual, A. Garcia-Abril, L. G. Garcia-Montero, S. Martin-Fernandez, and W. B. Cohen. Object-based semi-automatic approach for forest structure characterization using lidar data in heterogeneous pinus sylvestris stands. *Forest Ecology and Management*, 255(11):3677–3685, 2008. 30

P.Canuti, N. Casagli, F. Catani, G. Falorni, and P. Farina. Integration of remote sensing techniques in different stages of landslide response. In K. Sassa, H. Fukuoka, F. Wang, and G. Wang, editors, *Progress in Landslide Science*, pages 251–260. Springer, 2007. 16, 67

Z. Perski. Applicability of ers-1 and ers-2 insar for land subsidence monitoring in the silesian coal mining region, poland. *International Archives of Photogrametry and Remote Sensing*, 32:555–558, 1998. 96, 152

N. Pfeifer, P. Stadler, and C. Briese. Derivation of digital terrain models in the scop environment. In *Proceedings of OEEPE workshop on Airborne Laserscanning and Interferometric SAR for Detailed Digital Elevation Models*, volume 40, page 13. OEEPE Publication, 1-3 March 2001. 134

R. D. Phillips, C. E. Blinn, L. T. Watson, and R. H. Wynne. An adaptive noise filtering algorithm for aviris data with implications for classification accuracy. *IEEE Transactions on Geoscience and Remote Sensing*, 47:3168–3179, 2009. 131

M. Pieraccini, N. Casagli, G. Luzi, D. Tarchi, D. Mecatti, L. Noferini, and C. Atzeni. Landslide monitoring by ground-based radar interferometry: a field test in valdarno (italy). *International Journal of Remote Sensing*, 24(6):1385–1391, 2003. 17

B. Pradhan and S. Lee. Landslide risk analysis using artificial neural network model focussing on different training sites. *International Journal of Physical Sciences*, 4(1):1–15, 2009. 103

B. Pradhan, S. Lee, and M. F. Buchroithner. A gis-based back-propagation neural network model and its cross-application and validation for landslide susceptibility analyses. *Computers, Environment and Urban Systems*, 34(3): 216–235, 2010. 104

A. Prokop and H. Panholzer. Assessing the capability of terrestrial laser scanning for monitoring slow moving landslides. *Natural Hazards and Earth System Sciences*, 9:1921–1928, 2009. 22

R. Punturo, H. Kern, R. Cirrincione, P. Mazzoleni, and A. Pezzino. P- and s-wave velocities and densities in silicate and calcite rocks from the peloritani mountains, sicily (italy): The effect of pressure, temperature and the direction of wave propagation. *Tectonophysics*, 409:55–72, 2005. 35, 36

R. J. Radke, S. Andra, O. Al-Kofahi, and S. Roysam. Image change detection algorithms: A systematic survey. *IEEE Transactions on Image Processing*, 14: 294–307, 2005. 129

J. Y. Rau, L. C. Chen, J. K. Liu, and T. H. Wu. Dynamics monitoring and disaster assessment for watershed management using time-series satellite images. *IEEE Transactions on Geoscience and Remote Sensing*, 45:1641–1649, 2007. 43, 130

D. Raucoules, S. Le Mouegravelic, C. Carnec, and C. King. Urban subsidence in the city of prato (italy) monitored by satellite radar interferometry. In *Proceedings of IGARSS 2002, IEEE*, pages 1225–1227, Toronto, Canada, 2002. Piscataway, NT. 148

K. A. Razak, M. W. Straatsma, C. J. Van Westen, J. P. Malet, and S. M. de Jong.

Airborne laser scanning of forested landslides characterization: terrain model quality and visualization. *Geomorphology*, in press. 136

I. S. Reed and X. Yu. Adaptive multiple-band cfar detection of an optical pattern with unknown spectral distribution. *IEEE Transactions on Acoustics, Speech and Signal Processing*, 38:1760–1770, 1990. 56

P. Reichenbach, M. Cardinali, P. De Vita, and F. Guzzetti. Regional hydrological thresholds for landslides and floods in the tiber river basin (central italy). *Environmental Geology*, 35(2-3):146–159, 1998. 104

J. Remondo, J. Bonachea, and A. Cendrero. A statistical approach to landslide risk modelling at basin scale: from landslide susceptibility to quantitative risk assessment. *Landslides*, 2(4):321–328, 2005. 103

J. Remondo, J. Bonachea, and A. Cendrero. Quantitative landslide risk assessment and mapping on the basis of recent occurrences. *Geomorphology*, 94: 496–507, 2008. 103, 106, 121, 124

P. Revellino, O. Hungr, F. M. Guadagno, and S. G. Evans. Velocity and runout simulation of destructive debris flows and debris avalanches in pyroclastic deposits, campania region, italy. *Environmental Geology*, 45(3):295–311, 2004. 105

J. A. Richards. *Remote Sensing Digital Image Analysis*. Springer-Verlag, Berlin, 1999. 49

J. A. Richards and X. Jia. *Remote Sensing Digital Image Analysis: An Introduction*. Springer-Verlag, Berlin, Germany, 2006. 51

P. A. Rosen, S. Hensley, I. R. Joughin, K. Li, S. N. Madsen, E. Rodriguez, and R. M. Goldstein. Synthetic aperture radar interferometry. *Proceedings of the IEEE*, 88(3):333–382, 2000. 16, 67

H. Rott and T. Nagle. The contribution of radar interferometry to the assessment of landslide hazards. *Advances in Space Research*, 37(4):710–719, 2006. 16, 67

H. Rott, B. Scheuchl, A. Siegel, and B. Grasemann. Monitoring very slow slope movements by means of sar interferometry: A case study from a mass waste above a reservoir in the otztal alps, austria. *Geophysical Research Letters*, 26 (11):1629–1632, 1999. 17

K. A. Rowlands, L. D. Jones, and M. Whitworth. Landslide laser scanning: a new look at an old problem. *Quarterly Journal of Engineering Geology and Hydrogeology*, 2:155–157, 2003. 22

S. B. Saba, M. van der Meijde, and H. van der Werff. Spatiotemporal landslide detection for the 2005 kashmir earthquake region. *Geomorphology*, 124:17–25, 2010. 16

N. Santacana, B. Baeza, J. Corominas, A. De Paz, and J. Marturia. A gis-based multivariate statistical analysis for shallow landslide susceptibility mapping in la pobla de lillet area (eastern pyrenees, spain). *Natural hazards*, 30(3):281–295, 2003. 104

M. Santoro. Sar basics. Training material, Gamma Remote Sensing AG, Worbstrasse 225, 3073 Guemligen Switzerland, 2008. 67

K. Sassa. Geotechnical model for the motion of landslides. In C. Bonnard,

editor, *Proceedings of the 5th International Symposium on Landslides*, pages 37–55, Lausanne, Switzerland, 1988. Balkema, Rotterdam, The Netherlands. 105

K. Sassa, H. Fukuoka, G. Wang, and N. Ishikawa. Undrained dynamic-loading ring-shear apparatus and its application to landslide dynamics. *Landslides*, 1 (1):7–19, 2004. 103

H. P. Sato, H. Hasegawa, S. Fujiwara, M. Tobita, M. Koarai, H. Une, and J. Iwahashi. Interpretation of landslide distribution triggered by the 2005 northern pakistan earthquake using spot 5 imagery. *Landslides*, 4(2):113–122, 2007. 14

D. J. Sauchyn and N. R. Trench. Landsat applied to landslide mapping. *Photogrammetric Engineering and Remote Sensing*, 44:735–741, 1978. 13

C Scheidl, D. Rickenmann, and M. Chiari. The use of airborne lidar data for the analysis of debris flow events in switzerland. *Natural Hazards and Earth System Sciences*, 8:1113–1127, 2008. 20

W. H. Schulz. Landslides mapped using lidar imagery, seattle, washington. Technical report, U.S. Geological Survey. 20

W. H. Schulz. Landslide susceptibility revealed by lidar imagery and historical records, seattle, washington. *Engineering Geology*, 89:67–87, 2007. 20

R. L. Schuster. Socioeconomic significance of landslides. In A. K. Turner and R. L. Schuster, editors, *Landslides: Investigation and Mitigation*, pages 12–35. Transportation Research Board, National Research Council, National Academy Press, Washington, DC, 1996. 3

R. L. Schuster and R. W. Fleming. Economic losses and fatalities due to landslides. *Bulletin of the Association of Engineering Geologists*, 23(1):11–28, 1986. 105, 117

S. E. Sesnie, P. E. Gessler, B. Finegan, and S. Thessler. Integrating landsat tm and srtm-dem derived variables with decision trees for habitat classification and change detection in complex neotropical environments. *Remote Sensing of Environment*, 112:2145–2159, 2008. 131

B.W. Silverman. *Density estimation for statistics and data analysis*. Chapman and Hall, London, UK, 1986. 83

A. Singh. Review article digital change detection techniques using remotely-sensed data. *International Journal of Remote Sensing*, 10:989–1003, 1989. 51

V. Singhroy, K. E. Mattar, and A. L. Gray. Landslide characterisation in canada using interferometric sar and combined sar and tm images. *Advances in Space Research*, 21(3):465–476, 1998. 17

L. C. Smith. Emerging applications of interferometric synthetic aperture radar (insar) in geomorphology and hydrology. *Annals of the Association of American Geographers*, 92:385–398, 2002. 96, 152

R. Soeters and C. J. Van Westen. Slope instability recognition, analysis, and zonation. In A. K. Turner and R. L. Shuster, editors, *Landslides: Investigation and Mitigation*, pages 129–177. Transportation Research Board, National Research Council, National Academy Press, Washington, DC, 1996. 11

Y. Sohn and N. S. Rebello. Supervised and unsupervised spectral angle classifiers. *Photogrammetric Engineering and Remote Sensing*, 68:1271–1280, 2002. 54

M. Soldati, A. Corsini, and A. Pasuto. Landslides and climate change in the italian dolomites since the late glacial. *Catena*, 55:141–161, 2004. 3

R. Somma, A. Messina, and S. Mazzoli. Syn-orogenic extension in the peloritani alpine thrust belt (ne sicily, italy): Evidence from the al unit. *Comptes Rendus Geosciences*, 337(9):861–871, 2005. 35, 36

C. Squarzoni, C. Delacourt, and P. Allemand. Nine years of spatial and temporal evolution of the la valette landslide observed by sar interferometry. *Engineering Geology*, 68:53–66, 2003. 16, 67

M. L. Stein. Interpolation of spatal data, some theory for kriging. Springer-Verlag, New York, 1999. 115

S. Sterlacchini, S. Frigerio, P. Giacomelli, and M. Brambilla. Landslide risk analysis: a multi-disciplinary methodological approach. *Natural Hazards and Earth System Science*, 7(6):657–675, 2007. 103

M. Story and R. G. Congalton. Accuracy assessment: a user's perspective. *Photogrammetric Engineering and Remote Sensing*, 52(3):397–399, 1986. 61

S. Stramondo, F. Bozzano, F. Marra, U. Wegmuller, F. R. Cinti, M. Moro, and M. Saroli. Subsidence induced by urbanisation in the city of rome detected by advanced insar technique and geotechnical investigations. *Remote Sensing of Environment*, 112:3160–3172, 2008. 96, 152

T. Strozzi, P. Farina, A. Corsini, C. Ambrosi, M. Thuring, J. Zilger, A. Wiesmann, U. Wegmuller, and C. Werner. Survey and monitoring of landslide displacements by means of l-band satellite sar interferometry. *Landslides*, 2(3): 193–201, 2005. 17

T. Strozzi, U. Wegnuller, H. R. Keusen, K. Graf, and A. Wiesmann. Analysis of the terrain displacement along a funicular by sar interferometry. *IEEE Geoscience and Remote Sensing Letters*, 3:15–18, 2006. 70, 71

M. Sturzenegger and D. Stead. Quantifying discontinuity orientation and persistence on high mountain rock slopes and large landslides using terrestrial remote sensing techniques. *Natural Hazards and Earth System Sciences*, 9: 267–287, 2009. 23

D. Tarchi, N. Casagli, S. Moretti, D. Leva, and A. J. Sieber. Monitoring landslide displacements by using ground-based synthetic aperture radar interferometry: Application to the ruinon landslide in the italian alps. *Journal of Geophysical Research*, 108:2387–2401, 2003a. 17, 19

D. Tarchi, Nicola Casagli, R. Fanti, D. D. Leva, G. Luzi, A. Pasuto, M. Pieraccini, and S. Silvano. Landslide monitoring by using ground-based sar interferometry: an example of application to the tessina landslide in italy. *Engineering Geology*, 68:15–30, 2003b. 17, 19

M. T. J. Terlien. The determination of statistical and deterministic hydrological landslide-triggering thresholds. *Environmental Geology*, 35(2-3):124–130, 1998. 104

G. Teza, A. Galgaro, N. Zaltron, and R. Genevois. Terrestrial laser scanner to detect landslide displacement fields: a new approach. *International Journal of Remote Sensing*, 28(16):3425–3446, 2007. 22

G. Teza, A. Pesci, R. Genevois, and A Galgaro. Characterization of landslide ground surface kinematics from terrestrial laser scanning and strain field computation. *Geomorphology*, 97:424–437, 2008. 22

S. Trevisani, M. Cavalli, and L Marchi. Variogram maps from lidar data as fingerprints of surface morphology on scree slopes. *Natural Hazards and Earth System Sciences*, 9:129–133, 2009. 20

G. E. Tucker, F. Catani, A. Rinaldo, and R. L. Bras. Statistical analysis of drainage density from digital terrain data. *Geomorphology*, 36:187–202, 2001. 82

UN/ISDR. Living with risk. a global review of disaster reduction initiatives. Technical report, UN Publications, Geneva, 2004. 5

M. Uzielli, F. Nadim S. Lacasse, and A. M. Kaynia. A conceptual framework for quantitative estimation of physical vulnerability to landslides. *Engineering Geology*, 102:251–256, 2008. 106

G. B. Vai and P. Martini. *Anatomy of an orogen: the Apennines and adjacent Mediterranean basins*. Kluwer Academic, Dordrecht, The Netherlands, 2001. 78

C. J. van Westen and F. L. Getahun. Analyzing the evolution of the tessina land-

slide using aerial photographs and digital elevation models. *Geomorphology*, 54:77–89, 2003. xii, 11, 12

C. J. van Westen, T. W. J. van Asch, and R. Soeters. Landslide hazard and risk zonation-why is it still so difficult? *Bulletin of Engineering Geology and the Environment*, 65:167–184, 2006. 61, 103, 104, 107, 121, 124

C. J. van Westen, E. Castellanos, and S. L. Kuriakose. Spatial data for landslide susceptibility, hazard, and vulnerability assessment: An overview. *Engineering Geology*, 102:112–131, 2008. 22

D. J. Varnes. Slope movement types and processes. In R. L. Schuster and R. J. Krizek, editors, *Landslides: Analysis and Control*, pages 11–33. Transportation Research Board, 1978. 1, 81

D. J. Varnes. Landslide hazard zonation: a review of principles and practice. In *Commission on landslides of the IAEG, UNESCO, Natural Hazards*, volume 3, page 61, 1984. 102, 103, 117, 121, 124

G. Vilardo, G.Ventura, C. Terranova, F. Matano, and S. Nardo. Ground deformation due to tectonic, hydrothermal, gravity, hydrogeological, and anthropic processes in the campania region (southern italy) from permanent scatterers synthetic aperture radar interferometry. *Remote Sensing of Environment*, 113: 197–212, 2009. 96, 152

E. Weinke, S. Lang, and M. Preiner. Strategies for semi-automated habitat delineation and spatial change assessment in an alpine environment. In T. Blaschke, S. Lang, and G. J. Hay, editors, *Object Based Image Analysis*, pages 711–732. Springer, Heidelberg, Berlin, New York, 2008. 30

C. Werner, U. Wegmuller, T. Strozzi, and A. Wiesmann. Interferometric point target analysis for deformation mapping. In *Proceedings of IGARSS 2003*, pages 4362–4364, Toulouse, France, 21-25 July 2003 2003. 70, 71

M. C. Z. Whitworth, D. P. Giles, and W. Murphy. Airborne remote sensing for landslide hazard assessment: a case study on the jurassic escarpment slopes of worcestershire, uk. *Quarterly Journal of Engineering Geology and Hydrogeology*, 38:285–300, 2005. 57

C. Wu and A. T. Murray. Estimating impervious surface distribution by spectral mixture analysis. *Remote Sensing of Environment*, 84:493–505, 2003. 131

Y. Yamaguchi, S. Tanaka, T. Odajima, T. Kamai, and S. Tsuchida. Detection of a landslide movement as geometric misregistration in image matching of spot hrv data of two different dates. *International Journal of Remote Sensing*, 24 (18):3523–3534, 2003. 14

X. Ye, H. Kaufmann, and X. F. Guo. Landslide monitoring in the three gorges area using d-insar and corner reflectors. *Photogrammetric Engineering and Remote Sensing*, 70(10):1167–1172, 2004. 17

J. Zezere, S. Oliveira, R. Garcia, and E. Reis. Landslide risk analysis in the area north of lisbon (portugal): evaluation of direct and indirect costs resulting from a motorway disruption by slope movements. *Landslides*, 4(2):123–136, 2007. 103

J. Zezere, R. Garcia, and S. Oliveira. Probabilistic landslide risk analysis considering direct costs in the area north of lisbon (portugal). *Geomorphology*, 94: 467–495, 2008. 103, 106

Q. Zhang, G. Pavlic, W. Chen, R. Fraser, S. Leblanc, and J. Cihlar. A semi-automatic segmentation procedure for feature extraction in remotely sensed imagery. *Computers and Geosciences*, 31(3):289–296, 2005. 30